IMPACT, the LLNL 3-D global atmospheric chemical transport model for the combined troposphere and stratosphere: Model description and analysis of ozone and other trace gases

D. A. Rotman, C. S. Atherton, D. J. Bergmann, P. J. Cameron-Smith,
C. C. Chuang, P. S. Connell, J. E. Dignon, A. Franz, K. E. Grant,
D. E. Kinnison,[1] C. R. Molenkamp, D. D. Proctor, and J. R. Tannahill
Atmospheric Science Division, Lawrence Livermore National Laboratory, Livermore, California, USA

Received 7 November 2002; revised 15 August 2003; accepted 8 September 2003; published 18 February 2004.

[1] We present a global chemical transport model called the Integrated Massively Parallel Atmospheric Chemical Transport (IMPACT) model. This model treats chemical and physical processes in the troposphere, the stratosphere, and the climatically critical tropopause region, allowing for physically based simulations of past, present, and future ozone and its precursors. The model is driven by meteorological fields from general circulation models (GCMs) or assimilated fields representing particular time periods. It includes anthropogenic and natural emissions, advective and convective transport, vertical diffusion, dry deposition, wet scavenging, and photochemistry. Simulations presented here use meteorological fields from the National Center for Atmospheric Research (NCAR) Middle Atmospheric Community Climate Model, Version 3 (MACCM3). IMPACT simulations of radon/lead are compared to observed vertical profiles and seasonal cycles. IMPACT results for a full chemistry simulation, with approximately 100 chemical species and 300 reactions representative of a mid-1990s atmosphere, are presented. The results are compared with surface, satellite, and ozonesonde observations. The model calculates a total annual flux from the stratosphere of 663 Tg O_3/year, and a net in situ tropospheric photochemical source (that is, production minus loss) of 161 Tg O_3/year, with 826 Tg O_3/year dry deposited. NO_x is overpredicted in the lower midlatitude stratosphere, perhaps because model aerosol surface densities are lower than actual values or the NO_x to NO_y conversion rate is underpredicted. Analysis of the free radical budget shows that ozone and NO_y abundances are simulated satisfactorily, as are HO_x catalytic cycles and total production and removal rates for ozone. *INDEX TERMS:* 3362 Meteorology and Atmospheric Dynamics: Stratosphere/troposphere interactions; 0368 Atmospheric Composition and Structure: Troposphere—constituent transport and chemistry; 0341 Atmospheric Composition and Structure: Middle atmosphere—constituent transport and chemistry (3334); 3367 Meteorology and Atmospheric Dynamics: Theoretical modeling; *KEYWORDS:* ozone, stratosphere, troposphere

Citation: Rotman, D. A., et al. (2004), IMPACT, the LLNL 3-D global atmospheric chemical transport model for the combined troposphere and stratosphere: Model description and analysis of ozone and other trace gases, *J. Geophys. Res.*, *109*, D04303, doi:10.1029/2002JD003155.

1. Introduction

[2] From pre-industrial times, the concentrations of key greenhouse gases such as carbon dioxide (CO_2), methane (CH_4), nitrous oxide (N_2O), and tropospheric ozone (O_3) have increased. Simultaneously, concentrations of stratospheric ozone have decreased. While CO_2 is an important greenhouse gas, the combined non-CO_2 greenhouse gases are also important to the radiative balance of the atmosphere [*Intergovernmental Panel on Climate Change* (*IPCC*), 2001]. A key region of interaction between atmospheric chemistry and the climate is the region near the tropopause. This is especially true for ozone and its precursors [*Lacis et al.*, 1990].

[3] Ozone in the stratosphere is beneficial to the biosphere because it absorbs a significant fraction of the sun's shorter wavelength ultraviolet radiation. Ozone in the troposphere is a pollutant (respiratory irritant in humans and acts to damage crops, vegetation, and many materials). It affects the Earth's energy balance by absorbing both incoming solar radiation and outgoing longwave radiation. Ozone is an important part of the oxidizing capacity of the atmosphere, through a photolysis pathway that leads to the hydroxyl radical (OH). Reaction with OH is the main sink

[1]Now at Atmospheric Chemistry Division, National Center for Atmospheric Research, Boulder, Colorado, USA.

0148-0227/04/2002JD003155$09.00

Table 1. Meteorological Input Fields Used in IMPACT

Variable	Units
Surface pressure	mbbar
Zonal wind	m s^{-1}
Meridional wind	m s^{-1}
Temperature	K
Specific humidity	g kg^{-1}
Surface air temperature	K
Downward solar flux at surface	W m^{-2}
Boundary layer height	mbbar
Surface friction velocity	m s^{-1}
Vertical diffusion coefficient	m^2 s^{-1}
Updraft convective mass flux	kg m^{-2} s^{-1}
Downdraft convective mass flux	kg m^{-2} s^{-1}
Entrainment into convective updraft	s^{-1}
Entrainment into convective downdraft	s^{-1}
Detrainment from convective updraft	s^{-1}
Convective precipitation	mm d^{-1}
Total precipitation	mm d^{-1}
Rainfall across cell edges	mm d^{-1}
Total cloud fraction by random overlap clouds	unitless
Large-scale cloud fraction	unitless
Convective cloud fraction	unitless
Turbulent kinetic energy	m^2 s^{-2}
Surface drag coefficient	unitless
Ground temperature	K
Surface roughness	m
Condensed water total	kg kg^{-1}

of many atmospheric species, so its concentration controls the distributions of many radiatively important species.

[4] Ozone in the troposphere arises from both in situ photochemical production and transport from the stratosphere [*Danielsen*, 1968; *Chung and Dann*, 1985; *Holton et al.*, 1995]. These two "sources" of ozone vary both spatially and temporally. Within the troposphere, ozone is formed in situ when carbon monoxide (CO), methane (CH_4), and non-methane hydrocarbons (NMHCs) react in the presence of nitrogen oxides ($NO_x = NO + NO_2$) and sunlight. In contrast, stratospheric ozone formation is initiated by the photolysis of O_2 and destroyed via catalytic reactions with NO, H (hydrogen), OH, Cl (chlorine) and Br (bromine), and self-photolysis. Transport of ozone-rich stratospheric air through the tropopause into the troposphere can occur during tropopause folding events [*Danielsen*, 1968], decay of cutoff weather systems [*Bamber et al.*, 1984; *Loring et al.*, 1996], stratospheric streamers [*Appenzeller and Davies*, 1992; *Appenzeller et al.*, 1996; *Langford and Reid*, 1998], and transport across the subtropical jet [*Langford*, 1999].

[5] In the past, attempts to simulate the observed distributions of ozone (and other important gases) have focused on either the stratosphere or the troposphere, often due to computational constraints. Stratospheric models either employed simplified parameterizations to represent tropospheric chemical and physical processes, or assumed the troposphere behaved as a boundary condition [e.g., *Rose and Brasseur*, 1989; *Chipperfield et al.*, 1993, 1994, 1995; *Brasseur et al.*, 1997; *Douglass et al.*, 1997, *Rotman et al.*, 2001]. Similarly, tropospheric models used tropopause boundary conditions or simplified stratospheric chemistry and transport [e.g., *Levy et al.*, 1985; *Penner et al.*, 1991; *Crutzen and Zimmerman*, 1991; *Roelofs and Lelieveld*, 1995; *Müller and Brasseur*, 1995; *Wang et al.*, 1998a; *Brasseur et al.*, 1998; *Horowitz et al.*, 1998; *Lawrence et al.*, 1999; *Bey et al.*, 2001].

[6] This paper presents a chemical transport model named IMPACT (version 2.0). IMPACT simulates chemical-transport processes, including the important chemical production and loss cycles throughout the troposphere, stratosphere, and tropopause region. This allows for a more physically realistic simulation of both the upper troposphere and lower stratosphere, which includes the chemically and climatically important region around the tropopause. Forthcoming modeling requires this capability to adequately simulate past and future scenarios. Because the computational needs of these tasks are substantial, IMPACT is designed to run on large parallel computers.

[7] This paper describes the scientific and computational formulation of IMPACT and simulation results for $^{222}Rn/^{210}Pb$ and photooxidants. The IMPACT model chemistry and physics is described in section 2. Tracer simulations are described and presented in section 3, while section 4 presents selected full photochemistry simulation results. Results and conclusions are discussed in section 5.

2. Model Description

[8] IMPACT is a global, three-dimensional, chemistry-transport model that contains both a prognostic troposphere and stratosphere. Its input meteorological fields are obtained from either a general circulation model (GCM) or assimilated data, such as that available from the Data Assimilation Office (DAO) at NASA-Goddard. IMPACT uses meteorology from a GCM to address historical, future, and climatological average studies. IMPACT uses assimilated data to simulate specific historical time periods, typically for particular regions of interest. This paper focuses on describing the scientific capabilities of the IMPACT model and general evaluation of model results; all simulations and results presented here were obtained using GCM (see next section on MACCM3) input data. The IMPACT grid resolution is dictated by the input meteorological data, although currently IMPACT is using a version of the advection code [*Lin and Rood*, 1996] that requires equal latitude gridding. Hence data not on equal latitudes (e.g., Gaussian data) is regridded before use.

[9] IMPACT is based on an operator-split method for emissions, advection, diffusion, deposition, convection, gravitational settling, photolysis and chemistry. Below, input meteorological fields and the model processes are described in greater detail.

2.1. Input Meteorological Fields

[10] Currently, IMPACT uses meteorological fields from either the NCAR MACCM3 GCM [*Kiehl et al.*, 1998] or the NASA DAO (Data Assimilation Office) GEOS-STRAT (Goddard EOS Assimilation System-Stratospheric Tracers of Atmospheric Transport) [*Coy and Swinbank*, 1997; *Coy et al.*, 1997] products. Table 1 lists the meteorological fields and their units used in IMPACT.

[11] The vertical structure of IMPACT is based on a hybrid sigma-pressure coordinate system,

$$P(i,j,k) = A(k) \times \mathrm{PT} + B(k) \times \mathrm{Psfc}(i,j), \quad (1)$$

in which P is local pressure, i, j, and k are the indices in longitude, latitude, and pressure, PT is a constant unique to

Table 2. List of Coefficients, A and B, Used in the Hybrid Sigma-Pressure Coordinate System[a]

A	B	Pressure (Psfc = 1000 mbar)
0.0000000	0.9925561	993
0.0012607	0.9692941	971
0.0048032	0.9248458	930
0.0102147	0.8569460	867
0.0170959	0.7706060	788
0.0249684	0.6718278	697
0.0333057	0.5672184	601
0.0411057	0.4693495	510
0.0477359	0.3861593	434
0.0533717	0.3154463	369
0.0581622	0.2553391	314
0.0622342	0.2042469	266
0.0656954	0.1608178	227
0.0686375	0.1239024	193
0.0711384	0.0925237	164
0.0732641	0.0658512	139
0.0750711	0.0431792	118
0.0766070	0.0239077	101
0.0779126	0.0075266	85.4
0.0724582	0.0000000	72.5
0.0611434	0.0000000	61.1
0.0513384	0.0000000	51.3
0.0428911	0.0000000	42.9
0.0356552	0.0000000	35.7
0.0294924	0.0000000	29.4
0.0242733	0.0000000	24.3
0.0198782	0.0000000	19.9
0.0161979	0.0000000	16.2
0.0131332	0.0000000	13.1
0.0105953	0.0000000	10.6
0.0085052	0.0000000	8.51
0.0067935	0.0000000	6.79
0.0053992	0.0000000	5.40
0.0042697	0.0000000	4.27
0.0033597	0.0000000	3.36
0.0026304	0.0000000	2.63
0.0020492	0.0000000	2.05
0.0015885	0.0000000	1.59
0.0012252	0.0000000	1.22
0.0009403	0.0000000	0.940
0.0007180	0.0000000	0.718
0.0005456	0.0000000	0.546
0.0004047	0.0000000	0.405
0.0002857	0.0000000	0.286
0.0001920	0.0000000	0.192
0.0001228	0.0000000	0.123
0.0000755	0.0000000	0.076
0.0000458	0.0000000	0.046
0.0000277	0.0000000	0.028
0.0000168	0.0000000	0.017
0.0000102	0.0000000	0.010
0.0000061	0.0000000	0.006

[a]P(i, j, k) = A(k) * PT + B(k) * Psfc(i, j).

the meteorological data set (1000 for MACCM3), Psfc is local surface pressure, and A and B are weighting factors dependent only on the vertical level index, k. The values for A and B are shown in Table 2. Such a general vertical system allows the use of pure sigma input data (such as DAO GEOS-STRAT), pure pressure data, or hybrid combinations of sigma and pressure (such as NCAR MACCM3).

[12] The NCAR MACCM3 input meteorology used for this paper covered 1 year using conditions representing the mid-1990s. MACCM3 ran on a T42 Gaussian grid, giving approximately 3° latitude × 3° longitude horizontal resolution. It has 52 hybrid vertical levels, with the top at 0.006 hPa. The T42 Gaussian grid varies latitudinally from pole to pole and was regridded by NCAR to 4° × 5° horizontal resolution. The IMPACT simulations in this work use this 4° × 5° regular grid. Vertical resolution in the tropopause region is approximately 1.15 km. The fields are cell-centered (commonly referred to as "A-grid") 3-hour averages.

2.2. Velocity/Pressure Adjustment

[13] Divergences in the wind field are inconsistent with time derivatives of the surface pressure field in both the DAO and NCAR meteorological fields. This inconsistency arises for two main reasons. First, we need time-averaged mass-fluxes rather than time-averaged or instantaneous winds. Second, the winds may have been re-gridded from the parent GCM grid system. Such inconsistencies between the wind and surface pressure fields inevitably lead to one of the following undesirable consequences: non-conservation of tracer mass, spurious changes in tracer concentration, or spurious changes to the surface pressure distribution. These problems do not arise from a deficiency in the advection routine, which conserves tracer mass and handles tracer concentrations properly. Rather, these problems are inherent in all chemistry tracer models using off-line meteorological fields with inconsistent winds and surface pressures, as discussed by *Jöckel et al.* [2001].

[14] In IMPACT, a method related to *Prather et al.* [1987, Appendix B.2] and *Heimann and Keeling* [1989, Appendix B], treats the inconsistency between winds and surface pressure. The IMPACT algorithm is simple, fast, and ensures exact equality between the surface pressure change implied by the divergence of the modified winds and the change in the meteorological field's surface pressure for each time step.

[15] The starting point for pressure-fixer algorithms is the divergence equation,

$$\frac{\partial P_F}{\partial t} = -\nabla \bullet F, \tag{2}$$

where F is the vertically integrated mass-flux derived from the meteorological field winds by multiplying the wind speed (m s^{-1}) and the pressure thickness of the layer (Pa) then summing in the vertical (note that this includes linear interpolation from grid box centered values to values on grid box boundaries). F has units of N m^{-1} s^{-1}. P_F (in Pa) is the associated surface pressure calculated via equation (2). An equivalent equation also applies to P_G, the surface pressure from the meteorological field, and G, the true mass-flux that gives rise to P_G. Ideally we would like to determine G, but it cannot be uniquely calculated because the homogeneous equation $\nabla \bullet G = 0$ has an infinite number of solutions. Instead, we want to calculate f, the smallest change to F that will satisfy

$$\nabla \bullet (F + f) = \nabla \bullet (G). \tag{3}$$

Although equation (3) does not have a unique solution either, it is much easier to find a solution in which f is small, rather than to ascertain which of the infinite set of solutions for G is the most physically realistic. It is more convenient

to re-express equation (3) in terms of the difference between the pressure tendencies of P_F and P_G, which we call P_{err},

$$P_{\text{err}} = \frac{\partial P_G}{\partial t} - \frac{\partial P_F}{\partial t}. \quad (4)$$

P_{err} can be calculated from the meteorological field variables P_G and F via equations (2) and (4) and knowledge of the meteorological field time step. Equation (3) then becomes

$$P_{err} = -\nabla \bullet f. \quad (5)$$

IMPACT uses the algorithm described and analyzed by P. J. Cameron-Smith et al. (manuscript in preparation, 2003) to solve equation (5) in a manner that is precise and efficient. The algorithm is as follows:

[16] 1. Subtract any global mean pressure change from P_{err}.

[17] 2. Remove the zonal mean distribution of P_{err} through zonally uniform values of f in the meridional direction. Note that the zonal mean of P_{err} will now be zero for all latitude bands. Note too that this implies the meridional component of f at each pole is zero.

[18] 3. In each latitude band, start with any grid box and set f on its eastern boundary to exactly remove the box's P_{err}. Then consider the next grid box to the east, and set f on its eastern boundary to remove its P_{err} plus the value of f on its western boundary, which was determined in the previous step. Iterate for the rest of the grid boxes in the latitude band. Finally, subtract off the zonal mean, so that the zonal mean of f in the zonal direction is zero. Note that this solution does not depend on which grid box is chosen to be the first box.

[19] 4. Distribute the horizontal mass-flux, f, (which is a column integral) between the different horizontal levels in proportion to dB(k), the change in $B(k)$ between the top and bottom of each level (see equation (1) in section 2.1). Since the divergence of f is equal to the needed correction to the surface pressure (by equation (5)), this method of apportioning f ensures that the additional air mass flowing into each grid cell is equal to the increase in its mass implied by the change in surface pressure (P_{err}), and hence there will be no change to the inferred air mass flowing through the top or bottom of any cell (i.e., no change to the vertical wind in hybrid coordinates).

[20] This algorithm guarantees that f will exactly satisfy equation (5), as opposed to the algorithm of *Prather et al.* [1987], which finds an f that only approximately satisfies equation (5). This algorithm generally generates small values for f, as do the other algorithms, but none of the three algorithms guarantees to find the absolutely smallest f, with the caveat that there are several possible definitions for what constitutes the "size" of f.

[21] Step 1 removes any change in global air mass since equation (5) only has a solution if the global integral of P_{err} is zero. Strictly speaking then, the algorithm does not solve equation (5), but rather finds a solution that eliminates all of the inconsistency between the meteorological winds and pressures except for any change in global air mass. Hence, once changes due to advection have been calculated, IMPACT uses the modified mass-fluxes ($F + f$) to determine its surface pressure, rather than P_G, in order to avoid causing residual mass-conservation/concentration errors.

[22] We ignore any changes to the air mass distribution due to sources and sinks of water (precipitation and evaporation from the surface) because the effect is small (water vapor is less than 1% of air mass, and change in column abundance is a small fraction of that) causing changes in the wind speed of a few millimeters per second.

[23] With this algorithm, tracer mass is now perfectly conserved by advection. We see significant changes for many species, especially in the lowermost stratosphere where ozone is 40–50% higher without the pressure-fixer (which is unreasonably high compared to ozonesonde data; see section 4.3 and Figures 11 and 12). We have not seen any significant changes in the model results attributable to altered horizontal advection patterns.

2.3. Photochemical Solution Technique and Reaction Mechanism

[24] The photochemical species equations within IMPACT are solved using the SMVGEAR II technique [*Jacobson*, 1995]. In particular, we use a species-by-species variable time step within our operator-split 1-hour time step to increase computational performance and control the relative and absolute numerical errors. SMVGEAR II also orders grid cells within each node's sub-region into blocks according to similarity in stiffness of the species ordinary differential equations (ODEs), which essentially optimizes the average time step. Block lengths are selected according to problem size and number of processors used.

[25] The photochemistry includes reactions for both the stratosphere and troposphere. Reactions occurring in the stratosphere include those for O_x, NO_y, ClO_y, HO_y, BrO_y, CH_4, and their oxidation products. Reactions allowed in the troposphere include those for O_3, OH, PAN, NO, NO_2, CO, CH_4, HNO_3, isoprene, ethane, propane, ketones (including acetone), formaldehyde, acetaldehyde, higher aldehydes, and their products [*Lurmann et al.*, 1986]. The mechanism also includes isoprene reactions [*Paulson and Seinfeld*, 1992], reactions in the remote troposphere [*Jacob and Wofsy*, 1988] and peroxy radical reactions [*Kirchner and Stockwell*, 1996]. Where applicable, absorption cross sections and reaction rate coefficients were taken from *DeMore et al.* [1997] and *Sander et al.* [2000]. This version of IMPACT does not include extensive sulfur chemical reactions, although other versions do. Even though reaction rates may be small away from their region of importance, for example CFC photolysis in the troposphere, all reactive processes are allowed to occur throughout the model domain.

[26] Substantial laboratory kinetic experiments on isoprene oxidation have been conducted since 1992. In this work, the isoprene mechanism proposed by *Paulson and Seinfeld* [1992] has been updated by incorporating recently updated isoprene-related reaction rate coefficients, products, and reaction yields, as denoted in Table A1.

[27] Simulating water vapor provides special challenges, since none of the input meteorological fields contain the important source of stratospheric water from methane oxidation and IMPACT does not include a full predictive hydrologic cycle. Within IMPACT, water is produced pho-

tochemically in the stratosphere from CH_4 and H_2. A local tropopause height is calculated (using local temperature and pressure information) to differentiate these regions (Jim Stobie, personal communication, 1999). This photochemically produced stratospheric water is transported as a separate tracer, thus enabling exchange into the troposphere, and loss by wet deposition. The total water vapor used in the photochemistry subroutines in the troposphere is equal to this water vapor tracer plus the water vapor read in from the meteorological data. The supply of water vapor from the troposphere to the stratosphere, through the so-called ''cold trap,'' is simulated by enforcing a climatological average 3 μmol mol^{-1} lower limit on stratospheric water vapor.

[28] This approach simulates fairly well the observed quantities of water in the stratosphere in the sense of vertical profile and meridional gradient (for example, in comparison with Plate 2b of *Harries et al.* [1996], with the concentration increasing to about 6.5 μmol mol^{-1} near the stratopause and in polar air returning to the troposphere. Water vapor mole fraction in air moving from the stratosphere to the troposphere is tracked into the troposphere; this avoids the possibility of artificial drying of air in the lowest stratosphere were the tropopause to descend from one time step to the next. Because the model does not include the complete hydrologic cycle with phase transitions, it naturally does not represent features of observed water vapor fields such as thin laminar layers in the lowest stratosphere, seasonal dependence of the hygropause, and polar dehydration.

[29] Photolysis frequencies are obtained from a clear-sky lookup table developed using methodologies from *Douglass et al.* [1997]. The rates are adjusted in the troposphere depending on the presence of clouds and the archived cloud fraction in the meteorological fields. Photolysis rates are decreased by a factor of 1 to 0.5 for clear sky fractions of 1 to 0. Although this approach is not considered a replacement for a full radiative transport calculation, it is necessary to account for the global cloud-average albedo of 0.3 used in producing the clear-sky look-up table. Computational performance was also considered.

[30] Table A1 lists the reactions and corresponding rate coefficients. Table A2 gives species names. Additionally, equilibrium constants are listed for six three-body reactions in which the products are thermally unstable at atmospheric conditions. Table A1 also includes six reaction rate coefficients that are expressed using complex mathematical functions (rather than Arrhenius or Troe expressions). For these, the reaction rate coefficient evaluated at 298K (k_{298K}) and the temperature dependence of the activation energy is listed.

[31] Nine heterogeneous processes are included in the photochemical mechanism, representing hydrolysis of acid anhydrides and chlorine activation. These reactions are listed in Table A3. However, neither the processes affecting aerosol composition or state in the winter polar stratosphere, nor the dehydration or denoxification of the stratospheric polar vortex are included.

[32] The tropospheric aerosol surface area densities used in N_2O_5 and NO_3 hydrolysis were interpolated from *Chuang et al.* [1997]. These surface area densities combine sulfate, biomass burning, and fossil fuel carbon-containing particles. Reaction probabilities for tropospheric processes do not depend on particle type and are assumed to represent surface interactions with a water coating. Hydrolyzes of N_2O_5 and NO_3 on dilute tropospheric sulfate aerosol to produce nitric acid are simulated as pseudo-first-order processes proportional to aerosol surface area. The pure water reaction probabilities of $\gamma^{N_2O_5} = 0.05$ and $\gamma^{NO_3} = 2.0 \times 10^{-4}$ [*DeMore et al.*, 1997] are used. These tropospheric aerosol surface densities are smoothly joined to the stratospheric aerosol loading discussed below. The tropospheric reaction representing the slow hydrolysis of NO_2 to produce HONO and HNO_3 is included (S. Sillman, personal communication, 1997) at a fixed second-order rate constant (4.0×10^{-24}) relative to water vapor. This reaction is presumably heterogeneously catalyzed and is an important source for HONO to initiate radical production at sunrise.

[33] Six of the reactions in Table A3 represent stratospheric hydrolyzes of N_2O_5, $ClONO_2$, and $BrONO_2$, and chlorine activation through surface-mediated reactions of HCl with $ClONO_2$, HOCl, and HOBr. Climatological distributions of stratospheric liquid binary sulfate aerosol surface area density based on 1995 SAGE II observations [*Thomason et al.*, 1997; *World Meteorological Organization* (*WMO*), 1999] are used in the calculation of the collision rate of the gas with the surface. The surface reaction probability, representing the irreversible reactive update of the gas on the aerosol, is temperature and composition dependent. Values are tabulated by *DeMore et al.* [1997], while the expressions implemented in IMPACT are derived from the experimental literature cited. Reactions between chlorine species, HCl + $ClONO_2$ for example, are treated as ''pseudo'' second order, by dividing the bimolecular heterogeneous rate constant by the HCl concentration, thus assuming all HCl is in the aerosol droplet at the temperatures for which such reactions are important. This simple approach captures the midlatitude conversion of NO_x to HNO_3 in the lower stratosphere, as well as a portion of the NO_x reduction and chlorine activation that drives the winter polar stratospheric ozone destruction. We achieve some degree of chlorine activation as a result of the nonlinear, negative temperature dependence of the heterogeneous reaction parameters. Rates of Cl activation can be fast enough at sufficiently low temperatures essentially to titrate the reaction partner in smaller abundance. Although presence of the enhanced surface area density provided by PSCs would speed this process, it can be effectively saturated to polar Cl-driven ozone loss.

2.4. Source Emission Inventories

[34] IMPACT includes monthly (or, in some cases, annual) average emissions of nitrogen oxides (NO_x), carbon monoxide (CO), methane (CH_4), non-methane hydrocarbons (NMHCs), nitrous oxide (N_2O), and chlorofluorohydrocarbons (CFCs). These sources arise mainly from industrial activities including fossil fuel emissions (NO_x, CO, CH_4, NMHCs, N_2O, CFCs), biomass burning (NO_x, CO, NMHCs, N_2O), vegetation (NMHCs), soils (NO_x, N_2O), and lightning (NO_x). Emissions for the IMPACT model are listed in Table 3.

2.4.1. Fuel Combustion and Industrial Activity Emissions

[35] Global emissions of NO_x from fossil fuel combustion are compiled on a 1° × 1° horizontal resolution by the

Table 3. Annual Source Emission Rates in the IMPACT Model

Source	Annual Emission, Tg yr^{-1}	Monthly (M) or Annual (A) Average
CO	1398 Tg CO	
Industrial/fossil fuel	525	A
Biomass burning	857	M
Oceans	16.5	M
CH_4	506 Tg CH_4	
Industrial/fossil fuel	38.4	A
Land fills	44.6	A
Biomass burning	91.6	M
Animals	75.8	A
Rice cultivation	79.7	M
Wetland/bogs/swamps/tundra	181.1	M
Termites	20.0	A
Loss via soil absorption	−(25.1)	A
NO_x (emitted as NO_2)	38.4 Tg N	
Industrial/fossil fuel	21.5	M
Biomass burning	6.4	M
Lightning	5.0	M
Soil processes	5.5	M
Aircraft	0.5	M
N_2O	18.1 Tg N_2O	
Industrial/fossil fuel	1.0	A
Biomass burning	0.4	A
Soil processes	10.6	A
Animals	1.3	A
Oceans	4.8	A
CFC11	0.115 Tg CFC11	A
CFC12	0.15 Tg CFC12	A
C_5H_8 (isoprene)	568 Tg C_5H_8	M
Terpenes	135 Tg $C_{10}H_{16}$	M
CH_3COCH_3 (acetone)	40 Tg CH_3COCH_3	
Industrial/fossil fuel combustion	1	A
Biomass burning	5	M
Biogenic (primary and secondary)	23	M
Terpene oxidation	11	M
C_2H_6 (ethane)	15.9 Tg C_2H_6	
Industrial/fossil fuel combustion	8.0	A
Biomass burning	6.3	M
Oceans	1.6	M
C_3H_8 (propane)	17.6 Tg C_3H_8	
Industrial/fossil fuel combustion	12.0	A
Biomass burning	4.7	M
Oceans	0.9	M

International Global Atmospheric Chemistry Project-Global Emissions Inventory Activity (IGAC-GEIA) [*Benkovitz et al.*, 1996] and updated by E. C. Voldner et al. (1° × 1° global SO_x and NO_x two-level inventory resolved seasonally into emission sectors and point and area emission sources, 1997, available at http://www.ortech.ca/cgeic/poster.html). This inventory gives surface emissions at two vertical levels for four seasons, which we then interpolate to monthly averages. The two levels in the GEIA inventory correspond well with the two lowest vertical levels of the IMPACT model. Aircraft NO_x emissions (0.51 Tg N yr^{-1}) are the monthly mean emissions inventory of *Baughcum et al.* [1996] and *Metwally* [1995].

[36] CO emissions arise primarily from biomass burning, fossil fuel combustion, and industrial processes. The 525 Tg CO yr^{-1} fossil fuel combustion source [*Dignon et al.*, 1998] is distributed seasonally with a 1° × 1° horizontal resolution. This source is consistent with recent fossil fuel combustion estimates of *Khalil* [1999] and *Pacyna and Graedel* [1995], which show CO emissions as 380–620 Tg CO yr^{-1} (best estimate of 500 Tg CO yr^{-1}) and 440 ± 150 Tg CO yr^{-1}, respectively. All CH_4 emissions are from Goddard Institute for Space Studies' (GISS) 1° × 1° inventory [*Fung et al.*, 1991; *Lerner et al.*, 1988], with the exception of methane hydrates and clathrates, which were not included due to uncertainties in their source strengths and locations. The industrial sources of ethane and propane are from *Watson et al.* [1991], as described by *Atherton* [1994]. They are scaled to give annual totals of 8 Tg yr^{-1} ethane and 12 Tg yr^{-1} propane [*Kanakidou and Crutzen*, 1993]. The industrial acetone source of 1 Tg yr^{-1} given by *Singh et al.* [1994] is distributed in a manner similar to the CO industrial distribution.

[37] The annual emissions of CFC11, CFC12, and N_2O (including natural N_2O sources) are obtained from GEIA [*McCulloch et al.*, 1994; *Bouwman et al.*, 1995]. The mixing ratio of CH_3CCl_3 in the lowest two model layers is specified to be typical of 1998 conditions [*WMO*, 2002].

2.4.2. Biomass Burning Emissions

[38] The biomass burning sources of NO_x, CO, and NMHCs are from *Atherton* [1995] based on the work of *Liousse et al.* [1996]. The sources are appropriate for the early 1990 time period. Since Liousse's emissions are only for tropical latitudes, the biomass burning CO source (which includes biofuel other than the liquid mobile source fuels) also incorporates the work of *Dignon et al.* [1998] for higher latitudes. Boreal forests fires are included although are a relatively small source compared to low and middle latitudes. The total value of our biomass burning source is 857 Tg CO yr^{-1}. Recent estimates of biomass burning CO range include 260–930 Tg CO yr^{-1} [*Olivier et al.*, 1996], while *Pacyna and Graedel* [1995] gives a range of 700 ± 200 Tg CO yr^{-1}. The IMPACT value lies toward the higher end of this range. Other published source estimates include 1000 ± 600 Tg CO yr^{-1} [*Conrad and Seiler*, 1986], 875 Tg CO yr^{-1} [*Andreae*, 1990], 300–900 Tg CO yr^{-1} [*Bates et al.*, 1995], 520 Tg CO yr^{-1} [*Wang et al.*, 1998a], and 661.8 Tg CO yr^{-1} [*Brasseur et al.*, 1998]. Emissions of CO from biomass burning for the months of January and July are illustrated in Figure 1.

[39] Biomass burning emissions of acetone total 5 Tg yr^{-1} [*Singh et al.*, 1994], and are spatially and temporally distributed according to the CO emissions shown in Figure 1. Ethane and propane biomass burning sources [*Atherton*, 1995] are similarly distributed.

2.4.3. Oceanic Emissions

[40] Carbon monoxide oceanic emissions are distributed temporally and seasonally based on work by *Erickson and Taylor* [1992], but with a total global source of 16.5 Tg CO yr^{-1} rather than 165 Tg yr^{-1} given in the original work. This value is similar to the recent estimate of *Bates et al.* [1995] of 13 Tg CO yr^{-1}. Ocean sources of ethane and propane are 0.9 and 1.6 Tg C yr^{-1}, respectively, and are distributed spatially and temporally as for carbon monoxide. These values are slightly larger than the emissions of 0.8 Tg C yr^{-1} for ethane and 1.1–1.4 Tg C yr^{-1} for propane estimated by others [*Brasseur et al.*, 1998; *IPCC*, 2001]. N_2O emissions, as stated earlier, are from GEIA, and originate from *Bouwman et al.* [1995].

2.4.4. NO_x From Soil and Lightning

[41] Nitrogen oxides are emitted during nitrification and denitrification activities by natural microbes that live in the soil. Monthly NO_x emissions from soils are from

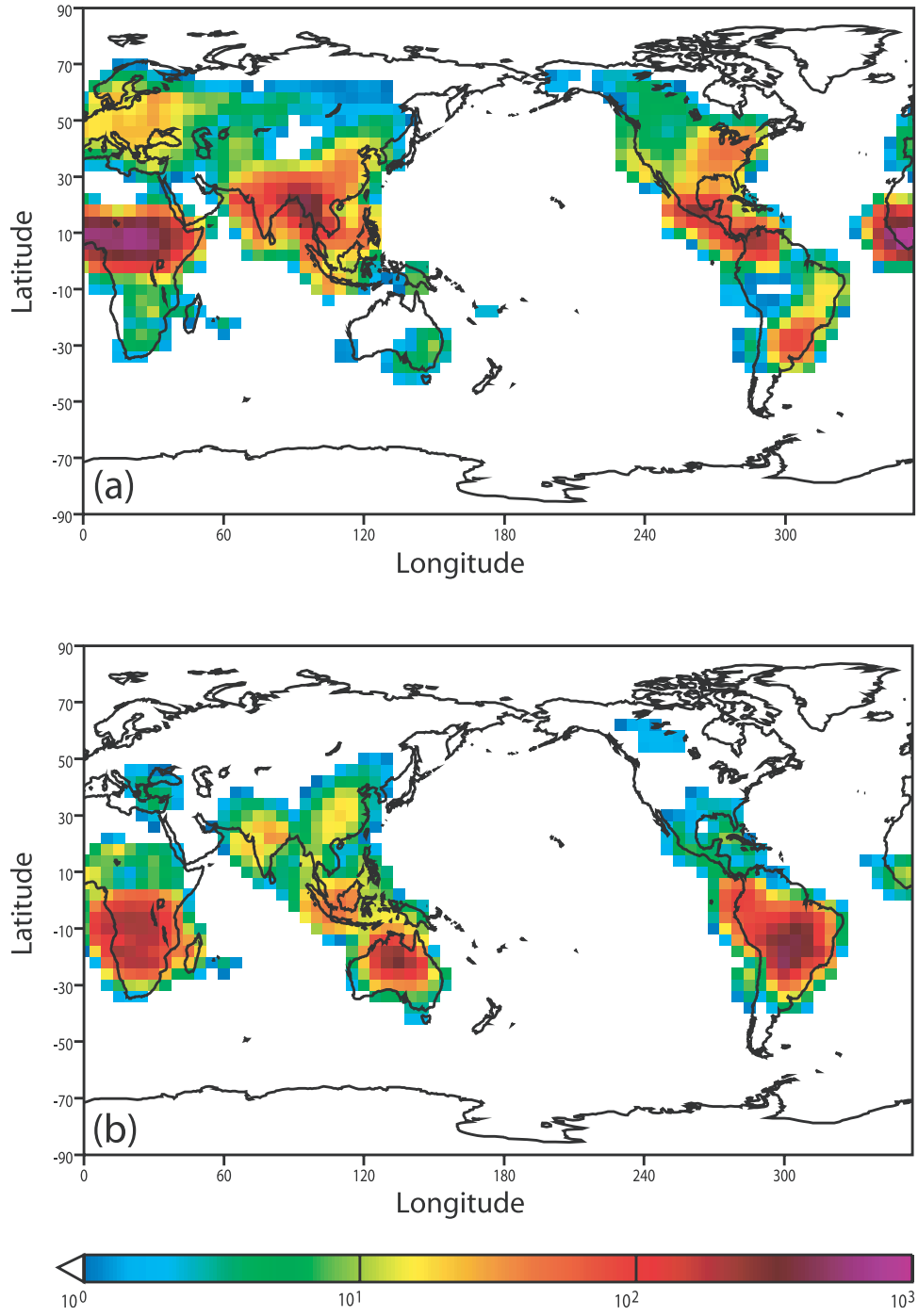

Figure 1. Emissions of CO in each 4° × 5° grid cell from bio-mass burning used in IMPACT for (a) January and (b) July, in kg CO s^{-1}.

Dignon et al. [1992] and incorporate monthly emission fluxes as a function of vegetation type [*Matthews*, 1983], temperature, and soil moisture [*Willmott et al.*, 1985]. Soil NO_x emissions are shown for January and July in Figure 2. Totaling 5.5 Tg N yr^{-1}, this estimate compares well with the inventory given by *Yienger and Levy* [1995].

[42] Atmospheric production of NO_x from high temperature N_2 fixation during lightning strikes is also included in IMPACT. The lightning source is 5.0 Tg N yr^{-1} and is horizontally distributed with the location of convective cloud activity according to parameterization of *Price and Rind* [1992]. The vertical distribution of the lightning NO_x is specified from cloud convection simulations of *Pickering et al.* [1998]. The emissions are input as monthly mean values.

2.4.5. Vegetation

[43] Vegetation is a large source of NMHC emissions; however, there is considerable uncertainty in this estimate. IMPACT's isoprene and terpene source distributions

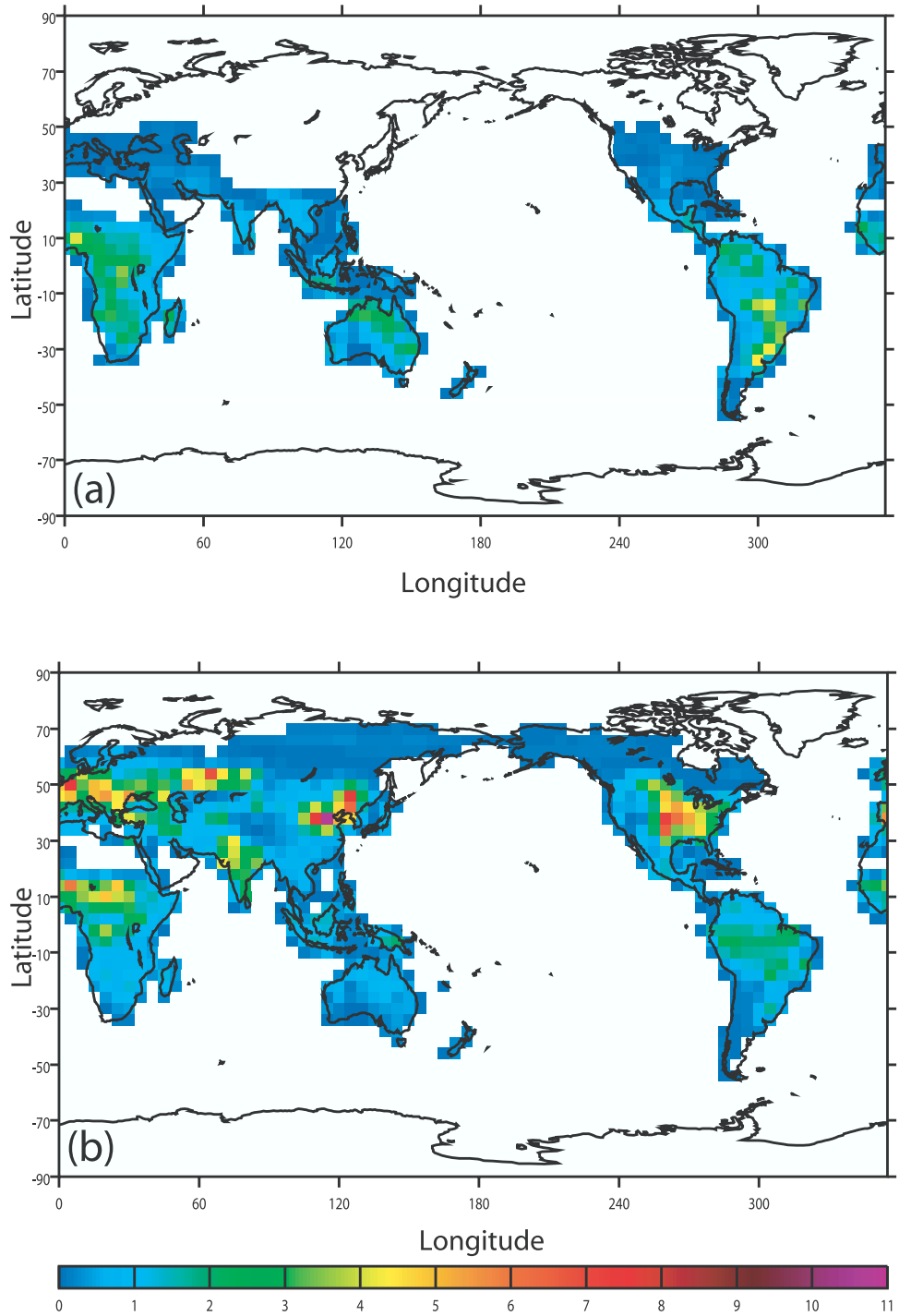

Figure 2. Soil NO_x emissions in each 4° × 5° grid cell in IMPACT for (a) January and (b) July, in kg N s^{-1}.

are from IGAC-GEIA [*Guenther et al.*, 1995] and total 568 Tg yr^{-1} and 135 Tg yr^{-1}, respectively. IMPACT uses a biogenic source of acetone of 34 Tg yr^{-1}, of which 18 Tg yr^{-1} and 16 Tg yr^{-1} are distributed as isoprene and terpene emissions, respectively.

2.5. Advection

[44] Chemical species in IMPACT advect via the Flux Form Semi-Lagrangian Transport (FFSLT) algorithm of *Lin and Rood* [1996]. FFSLT uses upstream differencing to reduce phase errors and contains multiple monotonicity constraints to eliminate the need for a filling algorithm. The scheme's basic building blocks are one-dimensional operators based on high-order Godunov-type finite volume schemes (primarily the third-order piecewise parabolic method, PPM). Multidimensional transport includes explicit consideration of the fluxes associated with cross terms. FFSLT avoids the strict Courant stability problem

at the poles by transitioning to a one-dimensional application of a modified semi-Lagrangian algorithm (SLT) for east-west advection (meridional and vertical transport always uses the PPM based scheme; see *Lin and Rood* [1996] for details). This combination of SLT and PPM allows larger time steps, resulting in highly efficient advection.

[45] IMPACT can incorporate any linear combination of pure sigma and pure pressure vertical coordinates (as described by equation (1)). Vertical mass fluxes in these coordinates are derived from the three-dimensional horizontal winds in the meteorological fields, conservation of mass, and the hydrostatic equation. This occurs after the horizontal winds have been modified to ensure mass conservation by the pressure-fixer, but by construction our pressure-fixer does not alter the vertical mass fluxes derived here (see section 2.2).

2.6. Diffusion

[46] Mixing of trace species due to sub-grid-scale eddies is modeled only in the vertical direction. IMPACT uses the three-dimensional field of time-varying vertical diffusion coefficients supplied in the meteorological fields. Vertical diffusion coefficients in the troposphere may have values as high as 100 to 1000 $m^2\ s^{-1}$, while stratospheric values are approximately 0.01 to 0.1 $m^2\ s^{-1}$. These diffusion coefficients are applied via an implicit scheme on each column [*Walton et al.*, 1988]. The scheme conserves mass, will maintain a flat field, and is not subject to time step constraints.

2.7. Convection

[47] Transport in convective updrafts is an important mechanism for moving material from near the Earth's surface in the planetary boundary layer (PBL) into the free troposphere. Convective mass-fluxes in each vertical column are supplied in the meteorological fields at interfaces between neighboring vertical layers. The magnitude and spatial variation of these fluxes vary among GCMs, but can be as large as 0.1 kg $m^{-2}\ s^{-1}$ and extend as high as 150 mbar above the surface in the tropics.

[48] Detrainment is also supplied in the meteorological fields. There can be substantial detrainment at multiple levels in a single convective column or little detrainment, except at the top of the convective column. Entrainment is calculated, to ensure conservation of mass, from the difference between the vertical derivative of convective mass flux and detrainment. Trace species convective transport is carried out using a modified version of the CONVTRANS algorithm [*Rasch et al.*, 1997]. Grid boxes within the PBL are considered well mixed for the convective scheme. The convection algorithm starts at the first grid box above the PBL and moves a fraction of each species upward into the convective updraft (planetary boundary layer height is provided in the input meteorological fields). The trace species mixing ratio within the convective updraft (different than the bulk grid box mixing ratio) is calculated. An equal amount of air is assumed to subside elsewhere in the grid box. Detrainment and entrainment terms then modify the mixing ratio both in the updraft and the bulk grid box. This algorithm marches upward in the column until there is no more convective mass-flux. The algorithm is fast, conserves mass, and will maintain any initial flat fields.

2.8. Wet Deposition

[49] Species are scavenged dependent on their solubility as described by their Henry's law coefficient. Highly soluble species such as HNO_3 and less soluble species such as acetone are transported and removed from the troposphere through a variety of hydrological processes (wet scavenging). Trace species can be incorporated into drops and ice crystals within clouds (rainout), collected by falling raindrops (washout), or be entrained into wet convective updrafts. IMPACT uses the Harvard wet scavenging model [*Mari et al.*, 2000; *Liu et al.*, 2001] that enhances previous models [*Giorgi and Chameides*, 1986; *Balkanski et al.*, 1993].

[50] Scavenging within convective updrafts is calculated within the convective transport algorithm. If these were independent operators, soluble species could be transported to the top of the convective column and then dispersed. In each convective column, beginning at the bottom grid box, the fraction of each species scavenged is calculated and directly deposited on the Earth's surface with no chance for re-evaporation [*Mari et al.*, 2000].

[51] Rainout, washout, and re-evaporation are each calculated for stratiform and convective precipitation. The three-dimensional meteorological field supplies rainfall or precipitable condensation rate, which are separated into convective and stratiform components. When not supplied in this form, rain is separated into components by the three-dimensional fields of convective and stratiform clouds. This module also operates on a column, but unlike the convective updrafts, rainout and washout are calculated from the top down, with the top grid box experiencing precipitation down to the ground. The horizontal area-fraction of each grid box experiencing precipitation is estimated [*Giorgi and Chameides*, 1986]. A fraction of each species (F_i) lost to rainout is then calculated from this areal fraction (f) and a Henry's Law dependent loss rate (k_i) in the form

$$F_i = f(1 - \exp[-k_i \Delta t]). \tag{6}$$

Aerosols and HNO_3 are assumed to be 100% in the cloud condensate phase with $k_i = 0.005\ s^{-1}$, while loss rates for other gases are dependent on Henry's law values.

[52] Washout occurs in grid boxes with no formation of precipitation and where precipitation is liquid. Re-suspension is calculated in all grid boxes with no formation of precipitation.

[53] Wet deposition of nitric acid (HNO_3) is shown in Figure 3. Nitric acid deposition is high near and downwind of NO_x source regions that are typically over populated continents.

2.9. Dry Deposition

[54] IMPACT calculates dry deposition loss rates using the dry deposition algorithm of *Wang et al.* [1998a], which follows the methodology of *Wesely et al.* [1985]. At each time step and for each surface grid box, this algorithm computes an aerodynamic resistance to deposition, which is dependent on meteorological conditions and surface type. A surface resistance is also calculated which depends on

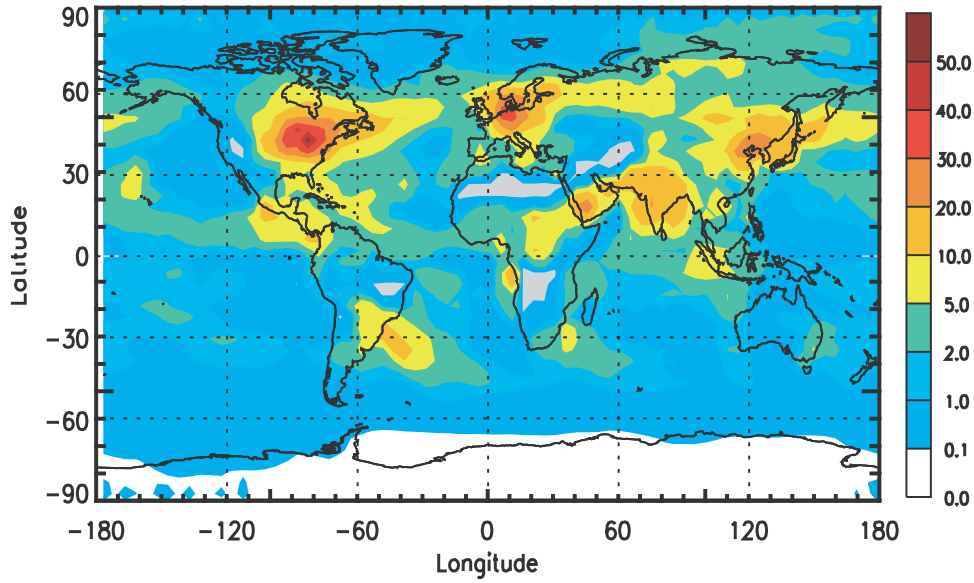

Figure 3. Amount of nitric acid (HNO_3) wet deposited in July, in kg N km^{-2} $month^{-1}$.

the physical characteristics of each species (Henry's Law coefficient and molecular weight), the meteorological conditions, the surface type, and a seasonal leaf area index [*Wang et al.*, 1998a]. Surface resistance components for the deposition land types are from *Wesely* [1989], except for tropical forests [from *Jacob and Wofsy*, 1990] and for tundra [from *Jacob et al.*, 1992]. The module then employs a resistance in series approach [*Wesely et al.*, 1985] to calculate a dry deposition velocity for each species.

[55] Dry deposition velocities for ozone for July are shown in Figure 4. The highest deposition velocities of 0.5–1 cm s^{-1} occur in regions of heavy vegetation. This is consistent with measurements and other global models.

2.10. Gravitational Settling

[56] When modeling aerosol movement in the atmosphere (e.g., lead), gravitational settling can play an important role if the aerosols are relatively large, if the time integration spans several years, or if stratospheric aerosols are involved. The mass-weighted settling velocity for the aerosol distribution is

$$\frac{\int \mathrm{vm}\frac{dN}{d\ln R}d\ln R}{\int \mathrm{m}\frac{dN}{d\ln R}d\ln R}, \tag{7}$$

where the mass, m, is given by

$$\mathrm{m} = \rho\, {}^{4}\!/_{3}\pi R^3 \qquad (\mathrm{g}), \tag{8}$$

and the velocity, v, is given by

$$\mathrm{v} = \frac{1}{18}\frac{4R^2\rho g C_c}{\mu} \qquad (\mathrm{cm\ s^{-1}}), \tag{9}$$

where N and R represent the number and radius (centimeters) of a log normal aerosol size distribution, μ is the viscosity (g cm^{-1} s^{-1}), C_c is the slip correction factor, and ρ is density (g cm^{-3}) [*Seinfeld and Pandis*, 1998].

[57] For a given size distribution, the mass-weighted settling velocity is a function of pressure and temperature. IMPACT uses a lookup table of settling velocities as a function of temperature and pressure that are applied at each time step to move a fraction of the aerosol from the grid box above to the current grid box. The advantages of this method are that the lookup tables are relatively small (6×16 entries for each distribution), apply to an arbitrary meteorological data grid, and have a much lower computational cost.

2.11. Computational Description

[58] Three-dimensional atmospheric chemistry models require large amounts of computational time because of their complexity, fine grid resolution, short time steps, and the need to perform simulations of long duration. To enable multiyear chemistry simulations, IMPACT runs on massively parallel (MP) computational platforms.

[59] LLNL's computational framework [*Mirin et al.*, 1994] uses a logically rectangular, two-dimensional longitude/latitude domain decomposition, with a computational processor attached to each subdomain. Each subdomain consists of a collection of full vertical columns, spread over a limited range of latitude and longitude. Message passing interfacing (MPI) is used to communicate information between subdomains as necessary. This two-dimensional domain decomposition is efficient because the chemistry and photolysis algorithms take up the vast majority of the computational cycles, are column based, and require no communication with neighboring grid zones. However, this decomposition does impose communication requirements for the horizontal advection operator.

[60] Nearly all of IMPACT's code is written in FORTRAN 77/95, with a small amount of C. FORTRAN 95's dynamic memory management capability and the MPI message

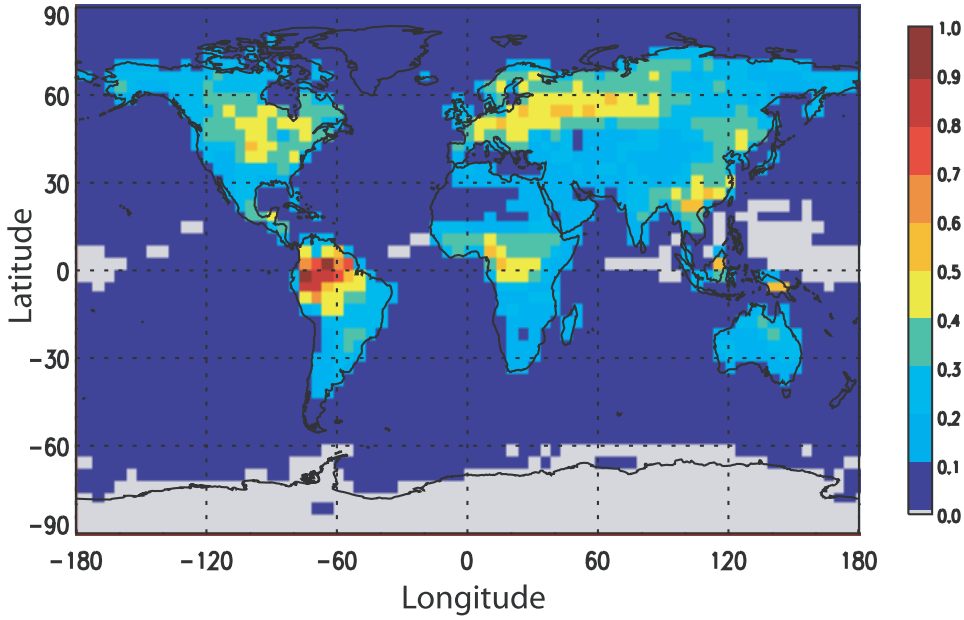

Figure 4. Calculated dry deposition velocity for O_3 in July, in cm s^{-1}.

passing interface enhance portability. IMPACT's conditional compilation at high levels in the code allows machine-specific constructs that optimize performance and still maintain portability across many architectures.

[61] The results presented in this paper were performed on a Compaq-SC1 computer using 36 processors, and required 48 hours to simulate a year. IMPACT's parallel computational efficiency (simulation time multiplied by the number of processors relative to a standard case with 36 processors) is nearly 70% up to 92 processors, yielding a year's simulation in 28 hours.

3. Model Calculations: ^{222}Rn/^{210}Pb

[62] The gas ^{222}Rn escapes from the ground into the atmosphere and decays into ^{210}Pb, which quickly attaches to any nearby aerosol. Comparing ^{222}Rn model simulations to atmospheric measurements tests a model's ability to accurately move trace species from the surface into the upper troposphere, while comparing modeled ^{210}Pb to observations tests a model's dry deposition, wet scavenging, and long-range transport representations.

[63] A ^{222}Rn/^{210}Pb simulation using MACCM3 4° × 5° meteorology was performed with the IMPACT model. Beginning with a clean atmosphere, ^{222}Rn was emitted from land surfaces at a rate of 1.0 atom cm^{-2} s^{-1}. This emission rate was reduced to 0.3 atom cm^{-2} s^{-1} when surface air temperature is below 230 K, based on measurements by *Larson* [1974]. This threshold differs from *Jacob et al.* [1997], who assumed ^{222}Rn emissions decreased to 0.005 atoms cm^{-2} s^{-1} between 60° to 70° in latitude, and to zero poleward of 70°. It also differs from the work of *Rind and Lerner* [1996], who set land emissions to 0.313 atom cm^{-2} s^{-1} when surface air temperature was less than 273 K. In sensitivity studies, high northern latitude concentrations of ^{222}Rn predicted by IMPACT were too low if ^{222}Rn emissions were severely limited or zeroed poleward of 60°, in particular, measurements made by Larson in the Yukon Valley showed near-surface measurements of 200 pCi M^{-3} while IMPACT results showed 20 pCi/M^{-3}. This conclusion is also supported by current non-zero ^{222}Rn emission measurements from snowpack in Maine (C. T. Hess, personal communication, 2001). Emission of radon from the oceans was assumed to be 0.005 atoms cm^{-2} s^{-1}. Global radon emissions were 15.5 kg yr^{-1}.

[64] Except for a small loss of radon through dry deposition (about 3%), the bulk of ^{222}Rn decays to ^{210}Pb with a time constant of 5.5 days. ^{210}Pb is stable, quickly attaches to existing atmospheric aerosols, and both dry and wet deposits. Because of its relatively short lifetime, ^{222}Rn reaches a steady state in the atmosphere after only a month or two, while ^{210}Pb requires a much longer simulation time for upper tropospheric and lower stratospheric concentrations to come to steady state. Gravitational settling is included for ^{210}Pb aerosol, as this can influence predicted aerosol concentrations in the stratosphere. Results from the final year of a 4-year simulation are discussed and plotted below.

[65] Figure 5 shows the seasonal variation in ^{210}Pb surface concentrations for six sites, three each from the Northern and Southern Hemispheres [*Larsen et al.*, 1995]. IMPACT captures the seasonal cycle and magnitudes of concentrations for Moosonee (Canada), New York City, Tutuila (Samoa), and Cape Grim (Tasmania). For Antofagasta (Chile), located directly on the western coast of South America, the model results are shown for both the grid box containing Antofagasta, as well as the grid box to the west. These model results bracket the observations, indicating that Antofagasta observations may represent a combination of oceanic and land influenced sampling conditions. Additionally, the exact location of a model grid box may affect predictions near continental boundaries.

[66] Model results for Mauna Loa, Hawaii, are lower than observations during the first half of the year, includ-

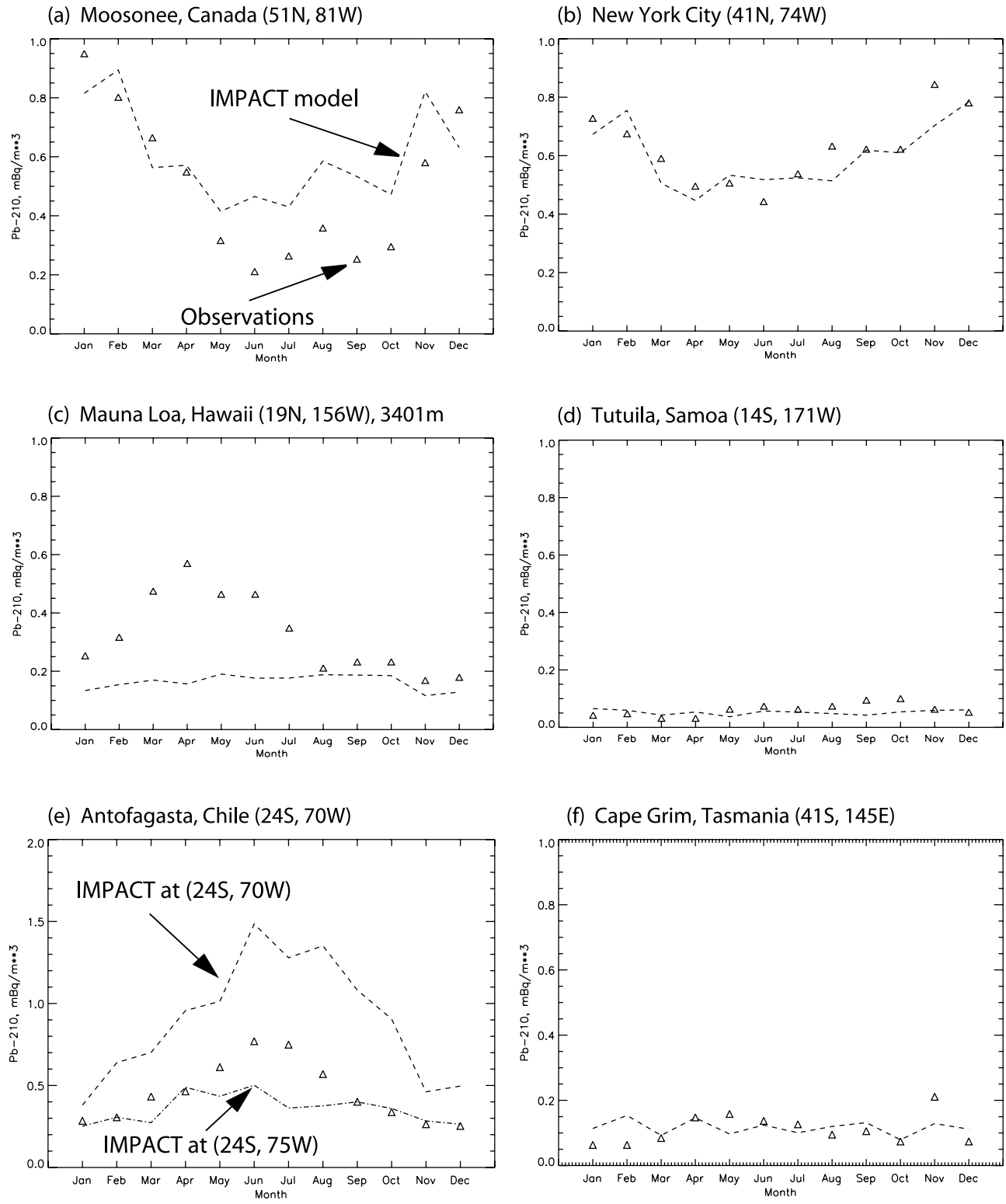

Figure 5. Comparison of surface [^{210}Pb], in mBq m^{-3} from the IMPACT model (dashed lines) and observations (triangles) from 1990–1993 [*Larsen et al.*, 1995]. Locations include (a) Moosonee, Canada, (b) New York City, (c) Mauna Loa, Hawaii, (d) Tutuila, Samoa, (e) Antofagasta, Chile, and (f) Cape Grim, Tasmania. IMPACT results for Figure 5e, Antofagasta, also include the model predictions for the grid box immediately to the west of Antofagasta.

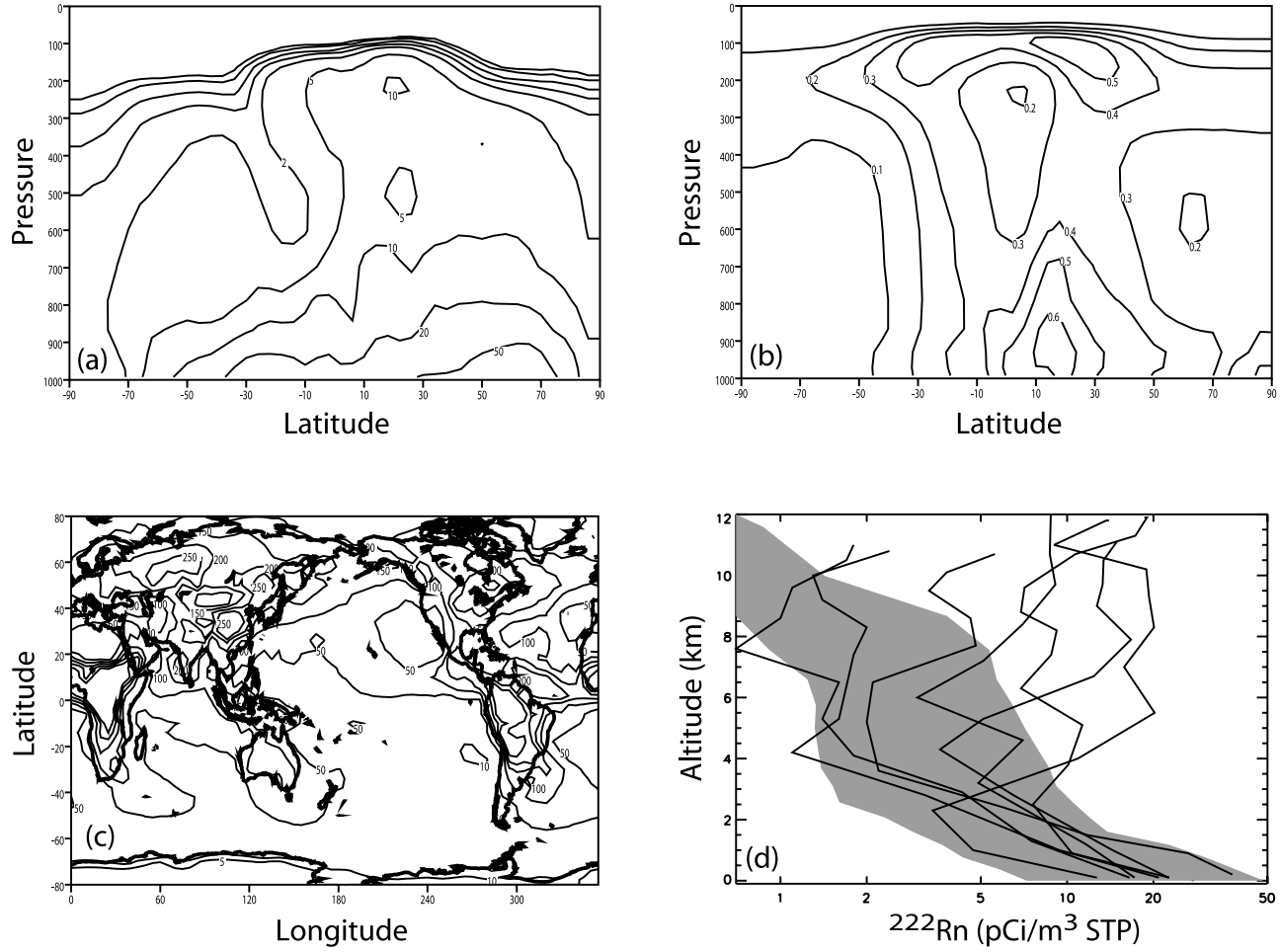

Figure 6. IMPACT-predicted (a) June/July/August zonal average mixing ratio of ^{222}Rn (10^{-21} mole mole^{-1}), (b) annual zonal average mixing ratio of ^{210}Pb (mBq m^{-3} STP), (c) total annual deposition of Pb (kg m^{-2}), and (d) IMPACT-predicted and observed vertical profiles of ^{222}Rn (pCi m^{-3} STP) near Moffett Field, California (37.4°N, 122°W). The lines are observations from individual flights on seven different days during June 1994 [*Kritz et al.*, 1998]. The shaded area represents 10–90% of the 720 model predicted hourly vertical profiles of ^{222}Rn off the coast near San Francisco in June.

ing spring, during which the region should experience maximum outflow from Asia [*Hoell et al.*, 1997]. The Mauna Loa site, at an altitude of roughly 3400 m, should experience free tropospheric flow. Analysis of IMPACT results shows the transport of lead from the Asian continent is too weak in the early months of the year resulting in this under prediction of lead. Other global models that also underpredict radon concentrations in the free troposphere [*Stockwell et al.*, 1998] hypothesize that they underestimate convective transport and/or vertical diffusion.

[67] Figure 6a shows the June-July-August average of the zonal mean concentration of ^{222}Rn predicted by IMPACT, which compares well with Figure 5 of *Jacob et al.* [1997] (a model intercomparison study of the ^{222}Rn cycle). Similar to other models, the IMPACT simulation shows a peak of 20–50 $\times$ 10^{-21} mol mol^{-1} between 800 and 1000 mbar over the northern midlatitudes, decreasing to roughly 5 $\times$ 10^{-21} mol mol^{-1} at 200 mbar. Small values of less than 1 $\times$ 10^{-21} mol mol^{-1} predicted for the middle to upper troposphere in the polar Southern Hemisphere compare well with other models [*Jacob et al.*, 1997]. The asymmetry between the Southern and Northern Hemispheres, due to differences in this land-based source (the Southern Hemisphere has far less land than the Northern Hemisphere) and accentuated by convection in the tropics, is also clearly displayed.

[68] Figure 6b shows the model-predicted, annual average, zonal mean concentration of ^{210}Pb. Similar to ^{222}Rn, there is an asymmetry between the Northern and Southern Hemispheres, due to the asymmetry in the land-based radon source. The model levels of 0.2–0.5 mBq per standard cubic meter (SCM) at 100–200 mbar agree quite well with the observed levels of 0.1–0.5 mBq SCM^{-1} and an annual average of 0.3–0.4 mBq SCM^{-1} [*Environmental Measurements Laboratory*, 2003] for altitudes between 12.2 and 19.2 km. The IMPACT model predicts a local minimum in the upper tropical troposphere, most likely due to scavenging in convective updrafts, as seen in other models [*Guelle et al.*, 1998; *Giannakopoulos et al.*, 1999; *Liu et al.*, 2001].

[69] Figure 6c show the simulated annual total deposition of ^{210}Pb. The maxima are located either directly above or

shortly downwind of continental regions, due to the land-based emission of ^{222}Rn and precipitation patterns. The maximum values of 200–250 kg m^{-2} over eastern Asia and minima of 10–50 kg m^{-2} over large regions of the southern oceans are similar to those found by an earlier model [*Feichter et al.*, 1991].

[70] Figure 6d shows IMPACT-predicted vertical profiles of radon off the western coast of North America near Moffett Field, California (37.4°N, 122°W). IMPACT predicted 720 hourly profiles of radon for June in this region. The shaded area represents 10–90% of these 720 model-predicted hourly vertical profiles. Also shown are seven individual radon profiles measured by *Kritz et al.* [1998]. Much of the envelope of predicted concentrations lie within those observed. However, several measured profiles have high concentrations of radon between 4 and 12 km. As discussed above, these high measurements in the free troposphere may not be reproduced by this and other models [*Stockwell et al.*, 1998, *Barrie et al.*, 2002] due to the model's radon source emissions or convective transport of radon into the free troposphere.

4. Model Calculations: Full Stratospheric and Tropospheric Photochemistry

[71] The primary model result we report here is a multiyear, full stratospheric and tropospheric photochemistry simulation with emissions, boundary, and initial conditions representative of the current atmosphere and meteorological fields from MACCM3. Results are presented from the last 12 months of a 40-month run initiated on day 244 (September 1) of a 365-day year. The initialization and length of this run is a compromise among dynamical and photochemical time constants in the troposphere and stratosphere. We specify emissions for many source gases, which enables the model to simulate tropospheric distributions for comparison to observations. It is computationally prohibitive to achieve steady state atmospheric burdens for source gases such as N_2O, CFCs, and others relative to their emissions. Thus, although the simulation is not sufficiently long to establish completely internally consistent stratospheric distributions of source gases, distributions and fluxes in the "middle world" of the lower stratosphere and the troposphere should be well represented.

[72] To help achieve these goals, the model is initialized with zonal mean distributions of source gases and product radical families from the LLNL two-dimensional, zonal model (for a recent description, see *Park et al.* [1999]). The 2-D model solves the IMPACT photochemical mechanism presented here, but with CH_4, N_2O, and CFCs set to 1998 abundances at the surface, rather than current emission fluxes. Additionally, the ozone distribution in the 2-D calculation was constrained to the *Logan* [1999a] zonal climatology developed from sets of observations. Although differences in the mean circulation and eddy diffusivity between 2- and 3-D dynamics will cause a transient in the IMPACT solution at the commencement of the 3-D run, stratospheric net fluxes and photochemical rates should still be characteristic of the solution, without memory of the initial condition. After more than 2 years of spinup, tropospheric quantities other than integrated burden of the source gases should have little dependence on the details of initialization.

4.1. Hydroxyl Radical, OH

[73] Zonal average tropospheric [OH] predicted for January and July is shown in Figure 7. The OH distribution has a local maximum in the tropical troposphere. In this region, radiation levels and water vapor concentrations, both of which contribute to OH production, are higher. A peak of 1.5×10^6 molecules cm^{-3} is located over the southern tropics in January. Its size diminishes somewhat in July, as the Intertropical Convergence Zone (ITCZ), a region with high water vapor concentration, shifts northward. Peak OH concentrations in July in the tropical to midlatitude Northern Hemisphere (near 30°N–40°N) reach $2.0–2.5 \times 10^6$ molecules cm^{-3}. These higher levels are due partially to emissions of NO_x and other ozone precursors from the highly industrialized Northern Hemisphere continents, which lead to higher O_3 and, ultimately, higher OH concentrations. The OH concentrations are in very good agreement with other recent global model values [*Hauglustaine et al.*, 1998, *Wang et al.*, 1998b; *Lawrence et al.*, 1999; *Bey et al.*, 2001], although the IMPACT January results tend to be slightly lower than those of *Bey et al.* [2001].

[74] The atmospheric lifetime of methyl chloroform, CH_3CCl_3, can be used as a proxy for the globally averaged hydroxyl radical concentration. Methyl chloroform, an industrial product, is removed predominantly by reaction with tropospheric OH. Its distribution and budget has been carefully characterized [*Montzka et al.*, 2000; *Prinn et al.*, 2001, and references therein]. Atmospheric lifetime can be defined in a variety of ways, including the ratio of the atmospheric burden to the loss rate at steady state [*WMO*, 1999; *IPCC*, 2001]. It is determined in IMPACT as the ratio of the total atmospheric mass of CH_3CCl_3 to the sum of the modeled loss rate processes given the modeled distribution. Because the lifetime is around 5 years, the steady state distribution of CH_3CCl_3 in the troposphere is essentially well mixed and is not sensitive to the details of tropospheric motions. The IMPACT lifetime should thus be close to the true steady state value.

[75] *Montzka et al.* [2000] derived a global CH_3CCl_3 lifetime of 5.2 years (+0.2/−0.3), by observing the decay of the abundance after emissions were reduced due to the Montreal Protocol. The lifetime includes losses due to (1) tropospheric reaction with OH, (2) stratospheric reaction with OH, (3) stratospheric photolysis, and (4) oceanic loss. Values derived from other observational techniques fall within these uncertainty limits. The IMPACT simulation described here includes the first three processes above, but does not include an explicit oceanic loss term. If an oceanic loss lifetime of 94 years (based on work by *Yvon-Lewis and Butler* [2002]) is assumed, the IMPACT calculated global CH_3CCl_3 lifetime is 5.3 years. The portion of the loss ascribed to reaction with tropospheric OH (the first process above) produces a lifetime of 6.5 years, while the loss ascribed to stratospheric reaction and photolysis (the second and third processes above) produces a lifetime of 41 years. The IMPACT OH tropospheric loss lifetime of 6.5 years is consistent with the 6.3-year value derived by *Montzka et al.* [2000].

[76] This good comparison is not sufficient to "validate" the related chemical and physical processes in IMPACT.

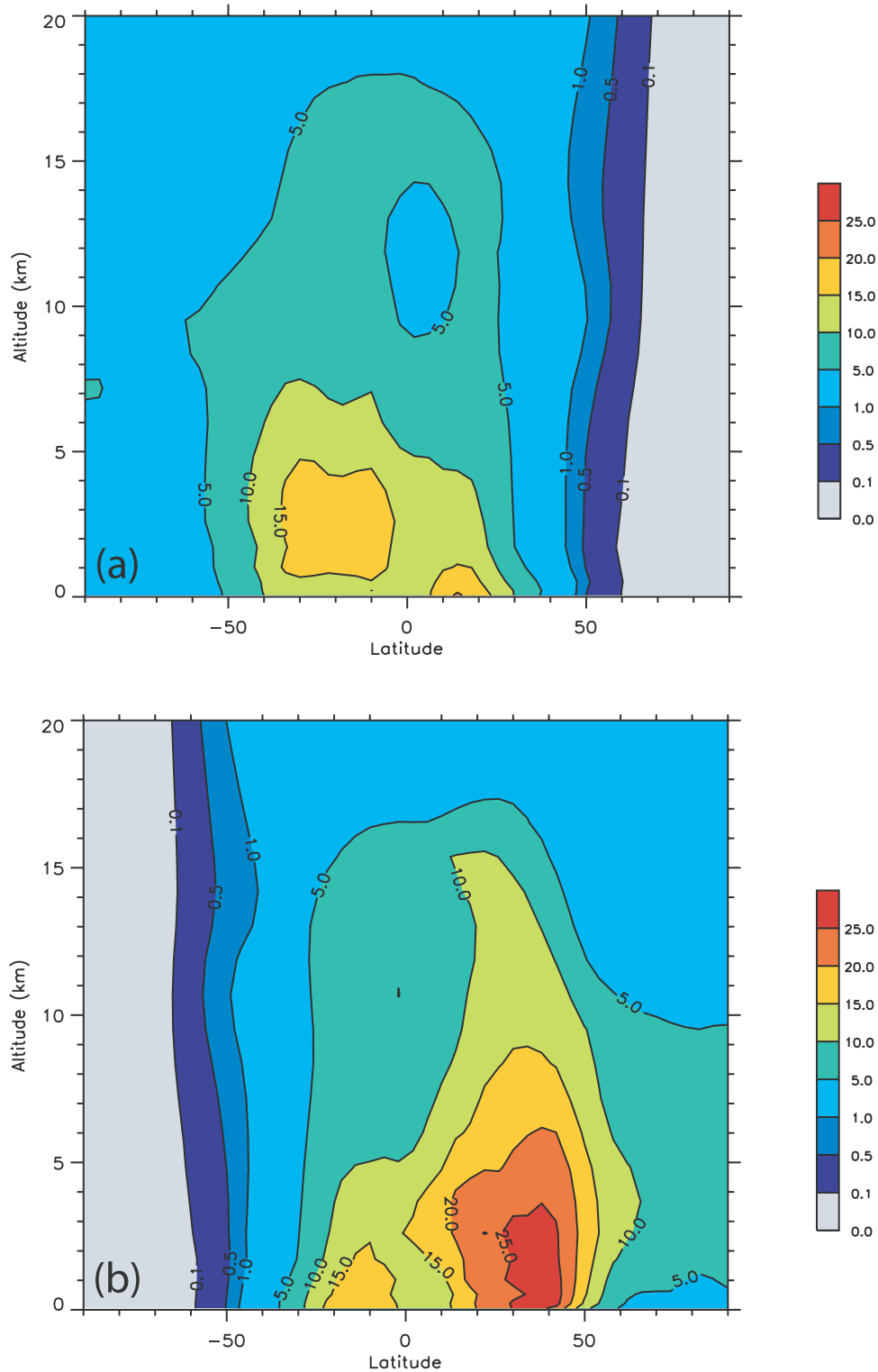

Figure 7. IMPACT predicted zonal average [OH] for (a) January and (b) July, in 10^5 cm^{-3}.

For example, IMPACT shows little interhemispheric asymmetry in OH, where the methyl chloroform decay over the last several years is more rapid south of the intertropical convergence zone [*Montzka et al.*, 2000]. However, we can conclude that the IMPACT troposphere possesses a good representation of global average tropospheric OH and that related species and processes that depend on this quantity should also be quantitatively reasonable.

4.2. Ozone Budget

[77] Global models are useful tools for analyzing the budget of tropospheric ozone. In the troposphere, the

Table 4. IMPACT Calculated Annual O_3 Flux Advected Across a Single Pressure Surface

Pressure, mbar	Advective Flux, Tg O_3/yr
288	945
245	929
208	895
177	854
150	805
128	760
109	725

main sources are ozone transport from the stratosphere (**S**) and local in situ photochemical production (**P**), with the major losses due to photochemical destruction (**L**) and dry deposition (**D**), where the bold quantities are global integrals over space and time. Other losses are minor. Within the troposphere, the term **P-L** represents a very small difference between two large quantities. If tropospheric ozone is in steady state, mass balance gives

$$\mathbf{S} + \mathbf{P} \approx \mathbf{L} + \mathbf{D}. \quad (10)$$

[78] The stratospheric source (**S**) is essentially independent of the troposphere (depending primarily on stratospheric chemical production and cross-tropopause air mass flux). Therefore, in the atmosphere, the globally averaged deposition (**D**) and net chemical production in the troposphere (**P-L**) must respond so as to satisfy equation (10) at steady state (even though the distribution of ozone in the troposphere is strongly affected by in situ production and loss, which are much larger individually than the stratospheric source, deposition, and net chemical production). Thus it is vital for a model to have a good estimate of the stratospheric source (**S**) in order to correctly determine the net chemical effect of anthropogenic activities on ozone. Recent tropospheric models have varied widely in their stratospheric source (391–1440 Tg O_3 yr^{-1} [*IPCC*, 2001]), which leads to the following observation: "the large differences in the stratospheric source are apparently the driving force behind whether a model calculates a chemical source or sink of tropospheric O_3. Individual CTM studies of the relative roles of stratospheric influx versus tropospheric chemistry in determining the tropospheric O_3 abundance. will not represent a consensus until all CTMs develop a more accurate representation of the stratospheric source consistent with observations [*Murphy and Fahey*, 1994]" [*IPCC*, 2001].

[79] Some models have achieved a reasonable stratospheric ozone source by fixing the magnitude of the stratospheric ozone flux in various ways. For IMPACT, in order to model past and future climates when the stratospheric source may be different, we allow the stratospheric source to be calculated prognostically and interactively through chemical production in the stratosphere and advection by the air mass fluxes given in the meteorological fields.

[80] Table 4 lists the IMPACT calculated annual advective ozone flux across seven different pressure levels. The annual flux ranges from 725 Tg O_3 yr^{-1} (across a pressure level of 109 mbar) to 945 Tg O_3 yr^{-1} (across a pressure level of 288 mbar). These fluxes fall well with the range of 391–1440 Tg O_3 yr^{-1} predicted by recent models [*IPCC*, 2001], although they are somewhat higher than the ranges of 550 ± 140 Tg O_3 yr^{-1} inferred by *Olsen et al.* [2001] and 450 (range: 200–870) Tg O_3 yr^{-1} estimated by *Murphy and Fahey* [1994].

[81] The monthly total tropospheric O_3 budget (**S**, **P-L**, **D**) calculated by the IMPACT model via two methods is shown in Table 5. For the first method (fixed tropopause), the tropopause is assumed to be 150 mbar globally. In the second method (latitudinally dependent tropopause), the tropopause is defined as 93 mbar for latitudes between 40°S and 40°N and 246 mbar for more poleward latitudes. Table 6 lists the annual tropospheric O_3 budgets calculated recently by other global CTMs, many of which, however, had fixed stratospheric concentrations or fluxes.

[82] Note that IMPACT calculates a net positive term for annual **P-L** (+17 Tg O_3 yr^{-1} for the fixed tropopause and +161 Tg O_3 yr^{-1} for the latitudinally dependent tropopause cases). This lies well within the range of −855–+600 Tg O_3 yr^{-1} shown in Table 6. However, the term **P-L** represents a very small difference between two large quantities. The **P-L** term calculated by the model may increase when higher hydrocarbons are included in the model. The smallest terms for **P-L** occur during October-April, while the largest occur for May through August. Since ozone is produced by the emission of many land-based precursors in the presence of sunlight, and the Northern Hemisphere has much more land than the Southern Hemisphere, it follows that the Northern Hemisphere summer is a peak time for in situ photochemical production. Dry deposition, which also peaks during Northern Hemisphere summer, is 826 Tg O_3 yr^{-1} for IMPACT, again well within the range of 533 to 1178 Tg O_3 yr^{-1} calculated by other models. Transport from the stratosphere peaks during March-May for

Table 5. Annual Tropospheric Ozone Budget (Tg O_3) Calculated Using IMPACT Model

	Net In Situ Photochemical Change (Production − Loss)		Advection From Stratosphere		
Month	Fixed Tropopause[a]	Latitudinally Dependent Tropopause[b]	Fixed Tropopause[a]	Latitudinally Dependent Tropopause[b]	Dry Deposition
Jan.	−12.3	1.0	80.5	58.2	53.3
Feb.	−8.5	4.1	76.7	59.8	50.1
March	−10.5	3.6	79.3	65.4	59.2
April	−6.4	7.1	66.3	61.7	63.9
May	16.3	28.2	71.3	62.0	80.1
June	30.9	41.7	58.2	57.0	89.1
July	26.6	36.9	60.0	58.7	92.4
Aug.	17.2	28.2	64.3	51.4	88.7
Sept.	0.7	12.3	55.6	45.5	75.3
Oct.	−18.0	−6.5	57.3	48.9	63.6
Nov.	−9.2	2.5	58.4	42.1	55.8
Dec.	−9.4	2.3	77.7	52.5	54.2
Annual	**+17.4**	**161.4**	**805.6**	**663.2**	**825.7**

[a]Tropopause defined to be 150 mbar globally.
[b]Tropopause defined to be 93 mbar for latitudes (−40° to +40°) and 246 mbar for more poleward latitudes.

Table 6. Tropospheric Ozone Budgets, Tg O_3/yr for Present-Day Conditions From 3-D CTMs[a]

Model	Transport From Stratosphere	In Situ P-L	Deposition	Reference
MATCH	1440	−810	620	*Crutzen et al.* [1999], *IPCC* [2001]
MATCH-MPIC	1103	−478	621	*Lawrence et al.* [1999], *IPCC* [2001]
ECHAM/TM3	768	−86	681	*Houweling et al.* [1998], *IPCC* [2001]
ECHAM/TM3[b]	740	−255	533	*Houweling et al.* [1998], *IPCC* [2001]
HARVARD	400	420	820	*Wang et al.* [1998a], *IPCC* [2001]
GCTM	696	128	825	*Levy et al.* [1997], *IPCC* [2001]
UIO	846	295	1178	*Berntsen et al.* [1996], *IPCC* [2001]
ECHAM4	459	75	534	*Roelofs and Lelieveld* [1997], *IPCC* [2001]
MOZART	391	507	898	*Hauglustaine et al.* [1998], *IPCC* [2001]
STOCHEM	432	430	862	*Stevenson et al.* [2000], *IPCC* [2001]
KNMI	1429	−855	574	*Wauben et al.* [1998], *IPCC* [2001]
UCI	473	345	812	*Wild and Prather* [2000], *IPCC* [2001]
ECHAM4/CBM-4	590	73	668	*Roelofs and Lelieveld* [2000]
ECMWF-NMHC	565	140	705	*Lelieveld and Dentener* [2000]
GEOS-CHEM	470	600	1070	*Bey et al.* [2001]
IMPACT-Latitudinally varying tropopause	663	161	826	this work

[a]Although results should sum such that S+P−L−D ∼ 0, they may not exactly, due to roundoff.
[b]Results using CH_4-only chemistry without NMHC.

IMPACT, corresponding to the traditional peak Northern Hemisphere spring maximum. Note that for the latitudinally dependent tropopause method, the combined sources of stratosphere-troposphere exchange and net in situ photochemical production balance dry deposition to within 1 Tg O_3 yr^{-1} showing that the contribution of convection, diffusion, wet deposition, and convergence to steady state terms are very small.

4.3. Ozone, O_3

[83] Zonal average stratospheric O_3 predicted by IMPACT for January and July is plotted in Figure 8, along with UARS-HALOE O_3 observations, version 18 [*Bruhl et al.*, 1996; *Randel et al.*, 1998]. The ozone data sets [*Bruhl et al.*, 1996] are compiled in the method described by *Randel et al.* [1998]. The location of peak ozone mixing ratios, at roughly 10 mbar in the tropics, is reproduced well by the model in both January and July. IMPACT predicts a slightly higher peak concentration, by ∼10%. IMPACT also captures the slight northward migration of peak ozone from January to July. Regions of lower ozone concentrations (toward the summer poles, and at very high and very low altitudes) are also simulated well by the model. At the winter poles, the IMPACT/MACCCM3 model appears to isolate the polar mid-stratosphere meridionally more strongly than the UARS/HALOE data shows occurs in the real atmosphere. We believe downward motion at the poles is too dominant over poleward motions, particularly in the Northern Hemisphere winter. We see this feature in other species (e.g., N_2O, not shown) as well.

[84] Surface ozone concentrations for the months of January and July are shown in Figure 9. Peak ozone concentrations are predicted over regions where emissions of ozone precursors (NO_x, CO, CH_4, NMHCs) and photochemical activity are highest. In January, this occurs primarily in the Northern Hemisphere tropics. In July, ozone peaks over the industrialized Northern Hemisphere continents (due primarily to industrialized emissions) and Southern Hemisphere continents (due primarily to biomass burning). During January, ozone in the Northern Hemisphere has a longer lifetime (decreased solar radiation decreases photochemical destruction) and is transported further across the oceans than during July. This is evident for both the Northern Pacific and Northern Atlantic Oceans.

[85] Monthly surface ozone measurements made at a number of remote locations [*Oltmans and Levy*, 1994] are compared to IMPACT predictions in Figure 10. IMPACT predicts concentrations within 10 ppbv and captures the seasonal cycle for the Southern Hemisphere sites of Samoa and the South Pole and Northern Hemisphere sites of Westman Island, Mace Head, Izaña, and Barbados. The model overpredicts ozone concentrations at Barrow during winter, spring, and fall, probably due to ozone depleting surface bromine reactions that are not adequately represented in the model [*Foster et al.*, 2001; *Oltmans and Levy*, 1994; *Barrie et al.*, 1988]. The model overpredicts ozone at Niwot Ridge during the summer, which is possibly caused by not resolving the typically pristine Niwot Ridge area within IMPACT's 4° × 5° grid. At Bermuda, high observed ozone levels can be associated with transport from the mid-troposphere over North America [*Oltmans and Levy*, 1994; *Moody et al.*, 1996; *Merrill and Moody*, 1996]. IMPACT simulations do not match observations at Mauna Loa with the model showing an over prediction of ozone of 20 ppb over the summer/fall season. These elevated ozone levels near the Hawaiian Islands persist to approximately 300 mbar, as shown in the vertical profiles of ozone at Hilo, Hawaii, for summer and fall (see PEM-TROPICS-Hawaii figure in the auxiliary materials[1]). Analysis of IMPACT's stratospheric ozone

[1] Auxiliary material is available at ftp://ftp.agu.org/apend/jd/2002JD003155.

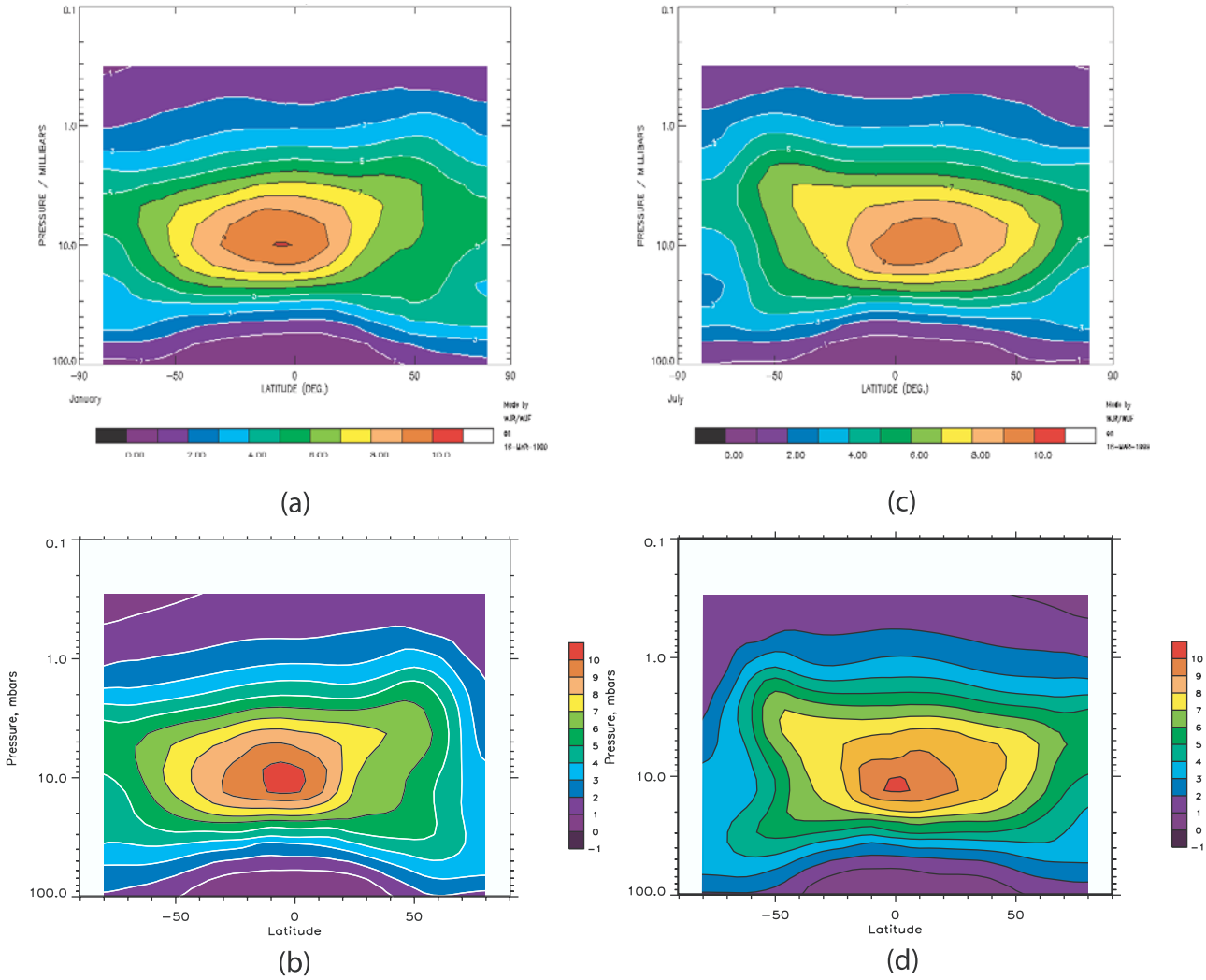

Figure 8. Meridional cross sections of ozone mixing ratio (ppmv) observed by the UARS-HALOE program (version 18) and predicted by IMPACT. The observations are from the extended standard ozone data set, which includes the baseline observations period (April 1992 to March 1993) as well as additional sampling time [*Bruhl et al.*, 1996] and are compiled in the manner described by *Randel et al.* [1998]. (a) January UARS-HALOE observations, (b) January IMPACT predictions, (c) July UARS-HALOE observations, and (d) July IMPACT predictions.

transport shows large downward transport during this region and period of time resulting in this enhanced tropospheric profile.

[86] Ozonesonde data for four sites in the NOAA/CMDL network are plotted with IMPACT results for each of the four seasons in Figure 11. Additional plots for other CMDL sites are shown in the auxiliary materials. Ozone mixing ratios are predicted usually within 5–10 nbar for much of the troposphere at the northern latitude site of Resolute during all four seasons. The model predicted stratospheric maximum location and magnitude does vary from observations, though, especially during March/April/May.

[87] A "midlatitude" site is operated by CMDL at Boulder. The IMPACT model predicts ozone above 100 nbar at the midlatitude site of Boulder to within 15% during all seasons except DJF where it over predicts ozone by 20–30 nbars. While the model predicts ozone levels within 5–10 nbar in the lower troposphere, it tends to overpredict ozone levels between 100 and 400 mbars. The cause of the general problem is likely vertical air mass fluxes from the meteorological fields.

[88] The IMPACT model predicts ozone at the tropical site of Samoa within 5 nbar for all four seasons throughout the troposphere and stratosphere. Much farther south, at Lauder, the IMPACT model predicted ozone mixing ratios in the lower troposphere agree with observations within 5 nbar for December/January/February and September/October/November. As with Boulder, the model over predicts O_3 in the upper troposphere for all four seasons because of excessive transport of stratospheric ozone. The model probably overpredicts ozone at Lauder during

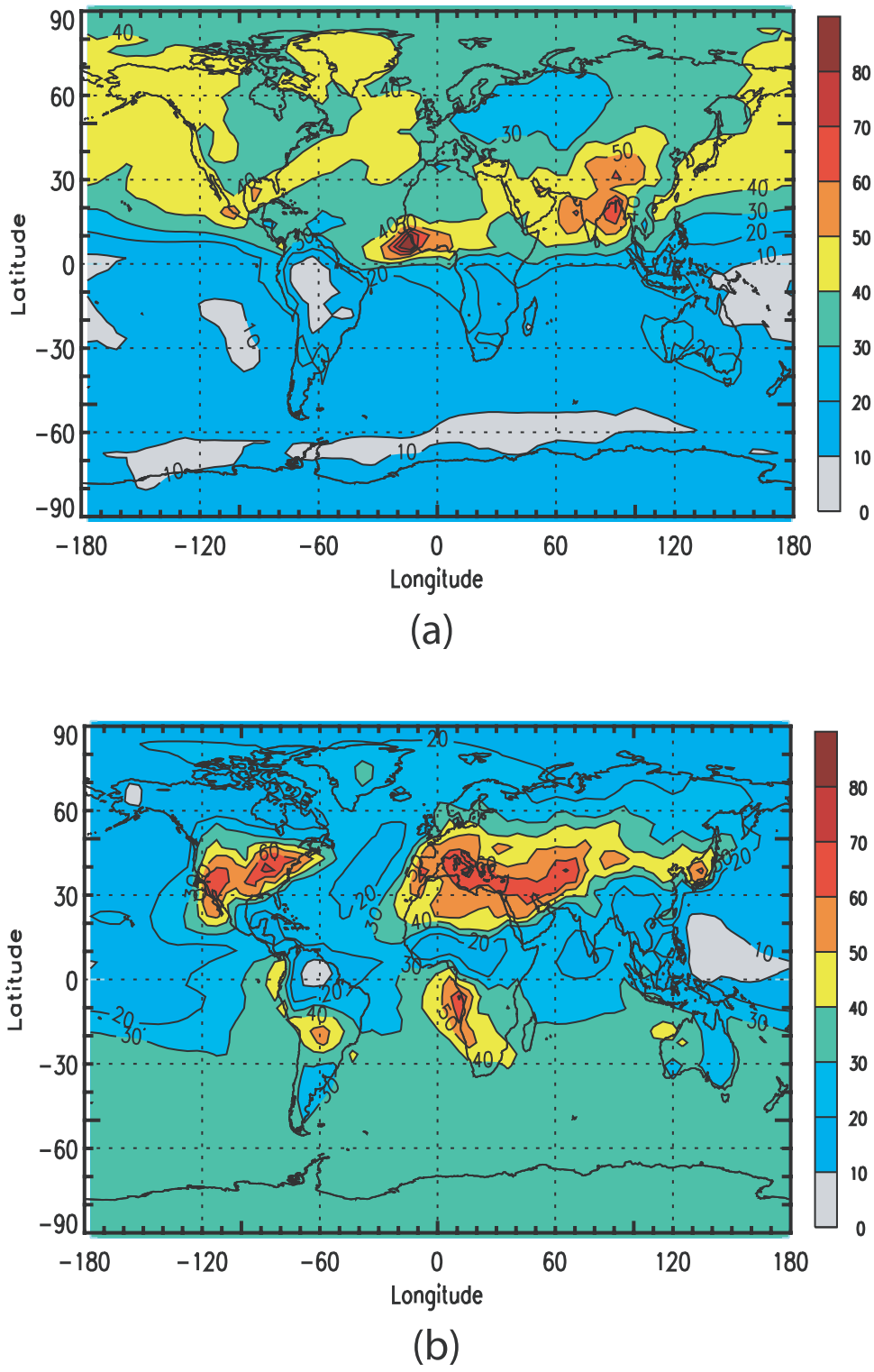

Figure 9. IMPACT-predicted surface [O_3] for (a) January and (b) July, in ppbv.

September/October/November, however, because phenomena associated with the ozone hole are not completely resolved within the model.

[89] Ozonesonde data [*Logan*, 1999a, 1999b] at 600, 200, 100, and 50 mbar from four locations are plotted, together with IMPACT predictions, in Figure 12. Additional plots for other sites are presented in the auxiliary materials. For 600 mbar, at the higher northern latitude site of Resolute, predictions from the IMPACT model agree within 10 ppbv with the mean observations for February to June. The model, however, overpredicts ozone during July–December/January by up to 15 ppbv. At 600 mbar,

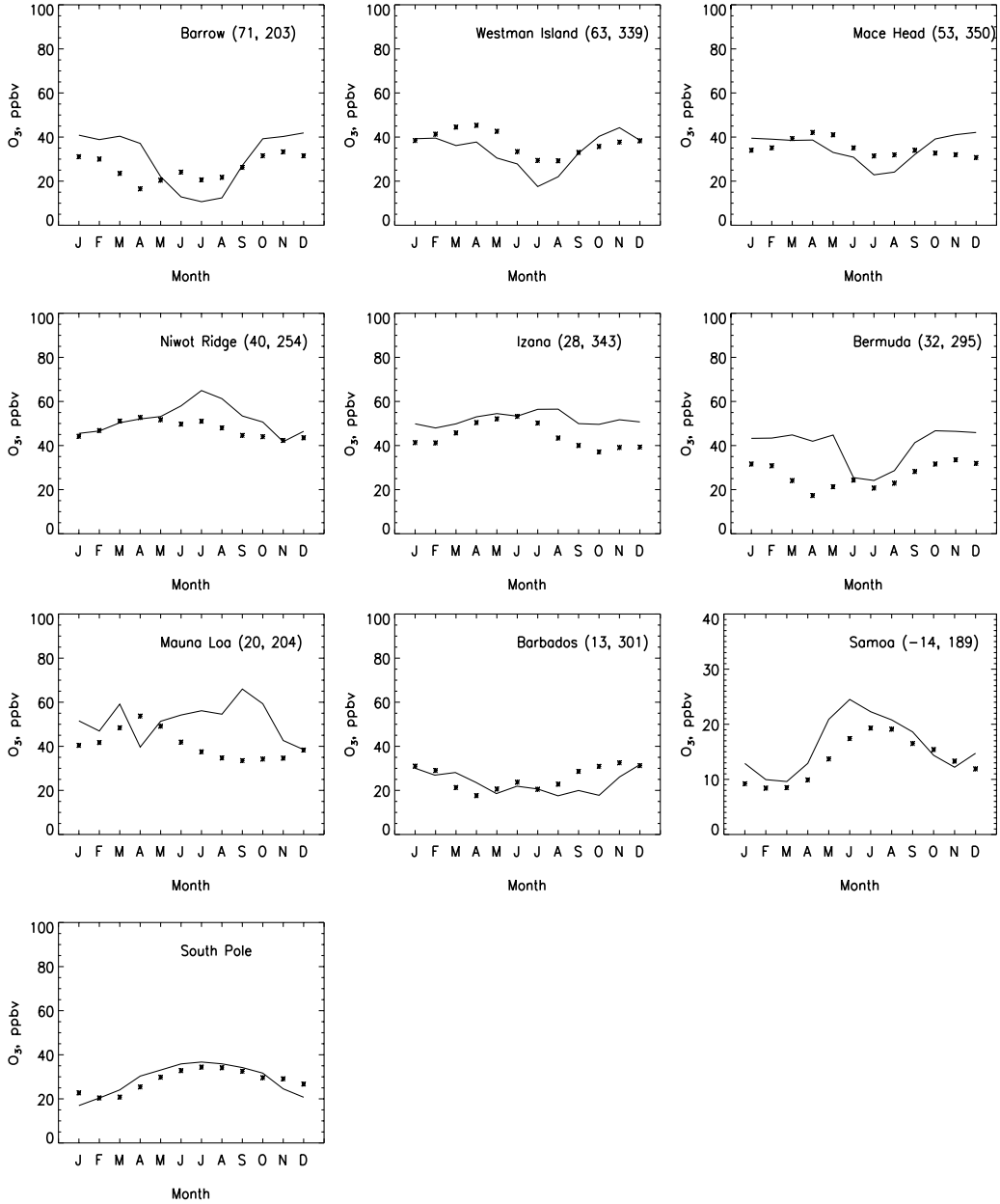

Figure 10. Annual cycle of observed mean O_3 concentrations (asterisks) and IMPACT-predicted [O_3] (solid lines) for 10 surface CMDL sites [*Oltmans and Levy*, 1994] located at Barrow, Westman Island, Mace Head, Niwot Ridge, Izana, Bermuda, Mauna Loa, Barbados, Samoa, and the South Pole.

the model predicts O_3 within 10 ppbv at Boulder, Samoa, and Lauder.

[90] At 200 mbar the IMPACT model represents the seasonal cycle at Resolute well, but predicts ozone concentrations higher than observed by 10–25% during June, July, and August. Observations of ozone over Resolute at 300 mbar show large variability because of the movements in the tropopause which IMPACT is not resolving. Model predictions capture the seasonal cycle very well at Boulder and Samoa. At Samoa, the model and observations agree within 5 ppbv. The largest differences between the model and observations at 200 mbar tend to be at the Southern Hemisphere site of Lauder and across all latitudes at 100 mbar. As discussed above, this is likely due to enhanced transport of stratospheric ozone. At 50 mbar, the model captures the seasonality of ozone at all four sites, while generally predicting slighter higher ozone levels (by 10–15%) than observed.

4.4. Ozone Precursors

[91] In Figure 13 are plotted profiles of ozone and other species from four different sampling campaigns, ABLE-3A (Alaska: 7 July to 17 August 1988), PEM-West A (Pacific Rim: 16 September to 21 October 1991), TRACE-A (Africa/South Atlantic Ocean: 21 September to 26 October 1992), and PEM-West B (Pacific Rim: 7 February to

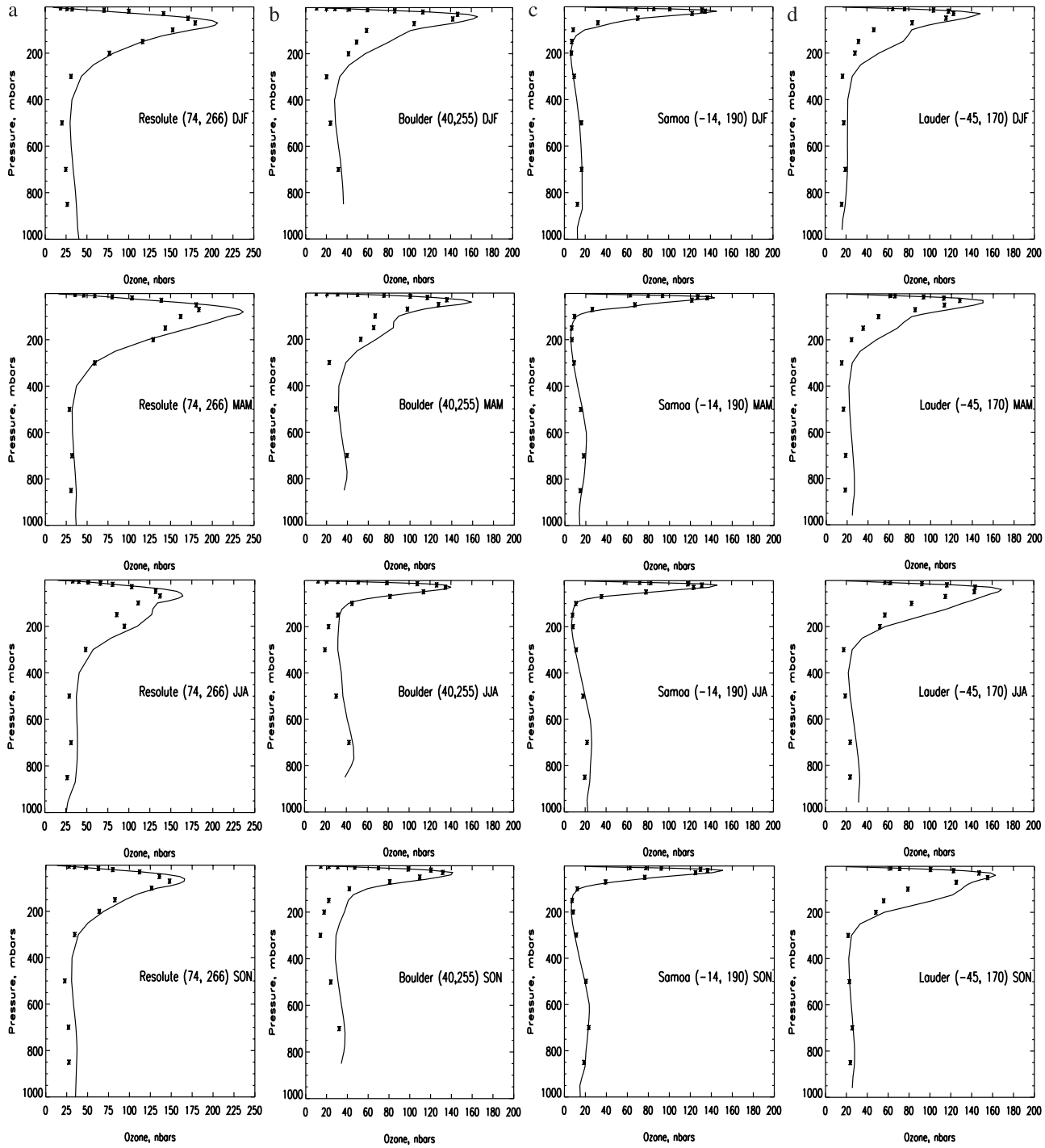

Figure 11. Observed and model-predicted ozone partial pressures in nbars as a function of altitude at four CMDL sites [*Komhyr et al.*, 1994] for (a) Resolute, (b) Boulder, (c) Samoa, and (d) Lauder. Rows show results for seasons December/January/February, March/April/May, June/July/August, and September/October/November.

14 March 1994) [*Emmons et al.*, 2000]. Additional plots from these and other campaigns are available in the auxiliary materials. The observations correspond to several particular sampling-intensive campaigns in specific seasons and years, while the IMPACT model results are monthly average concentrations obtained using MACCM3 meteorology, representing more of a climatological average.

[92] The IMPACT ozone concentrations match observations for ABLE3A, but the model slightly underpredicts ozone for TRACE-A, by 10–20 ppb, and overpredicts ozone for PEM-West B for altitudes above 4 km, by up to a factor of 2 above 10 km. This is likely due to the model's placement of the tropopause too low, although the observations do show large variations in ozone above 8 km. The

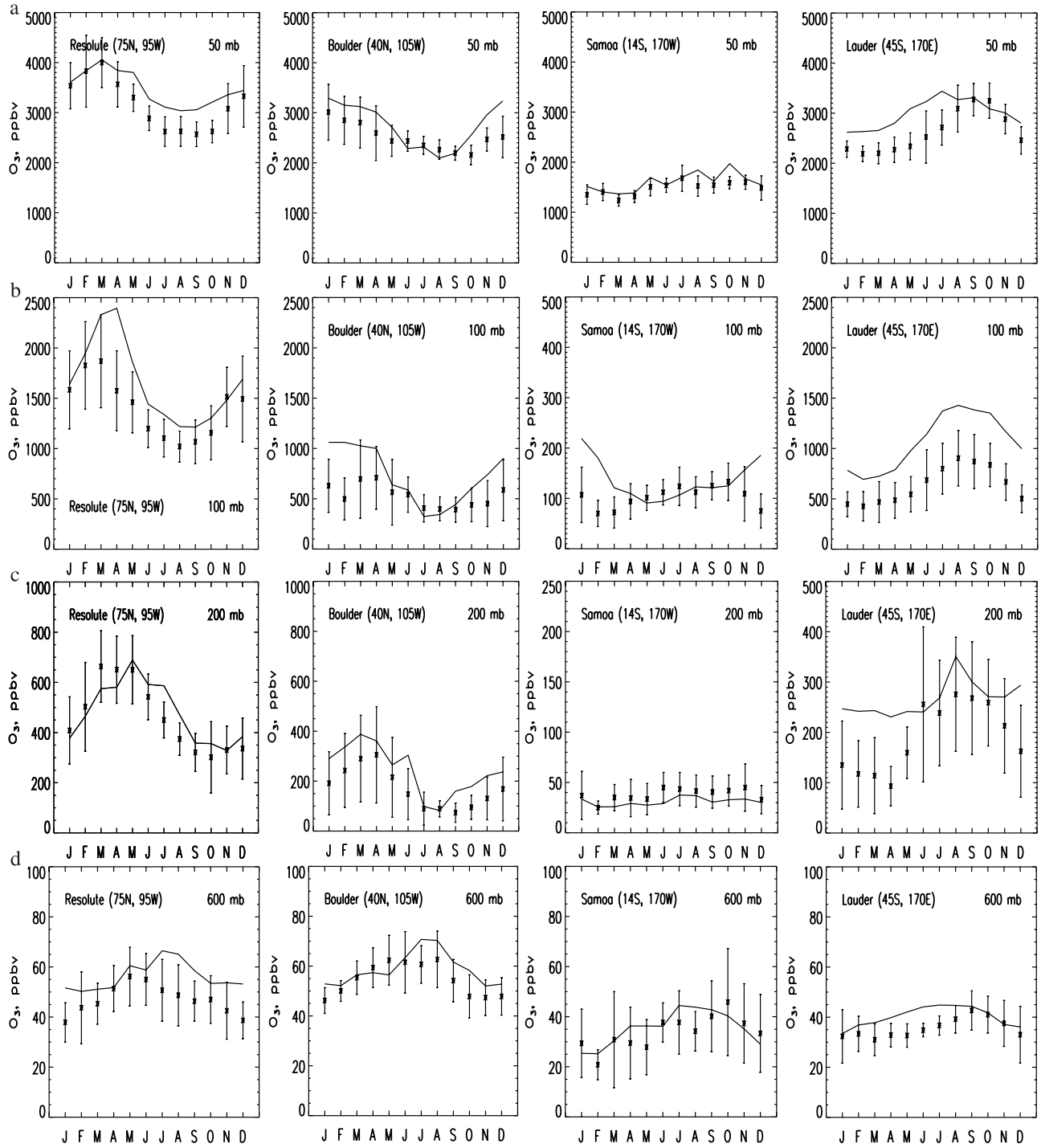

Figure 12. Observed [*Logan et al.*, 1999a, 1999b] and model-predicted ozone concentrations at the four sites shown in Figure 11 for vertical levels located at (a) 50 mbar, (b) 100 mbar, (c) 200 mbar, and (d) 600 mbar.

IMPACT model is not able to reproduce the detailed structure in the ozone profile for PEM-West A. The model predicts mean NO_x concentrations very well at all four locations. Model HNO_3 levels compare well with observations in TRACE-A and PEM-West B, but are too high by a factor of up to 10 at PEM-West A (as are the PAN concentrations). At PEM-West B locations, the model underpredicts PAN levels below 4 km. Although the model captures the H_2O_2 concentrations well for PEM-West A and PEM-West B, it underpredicts by a factor of 2 the large H_2O_2 concentrations observed within the bottom 4–6 km for TRACE-A. Additionally, the model underpredicts CO concentrations for 2–4 km for TRACE-A, indicating the model may not mix some species up as high as they are actually lofted. CO concentrations tend to agree with observations for both PEM-West A campaigns, but are

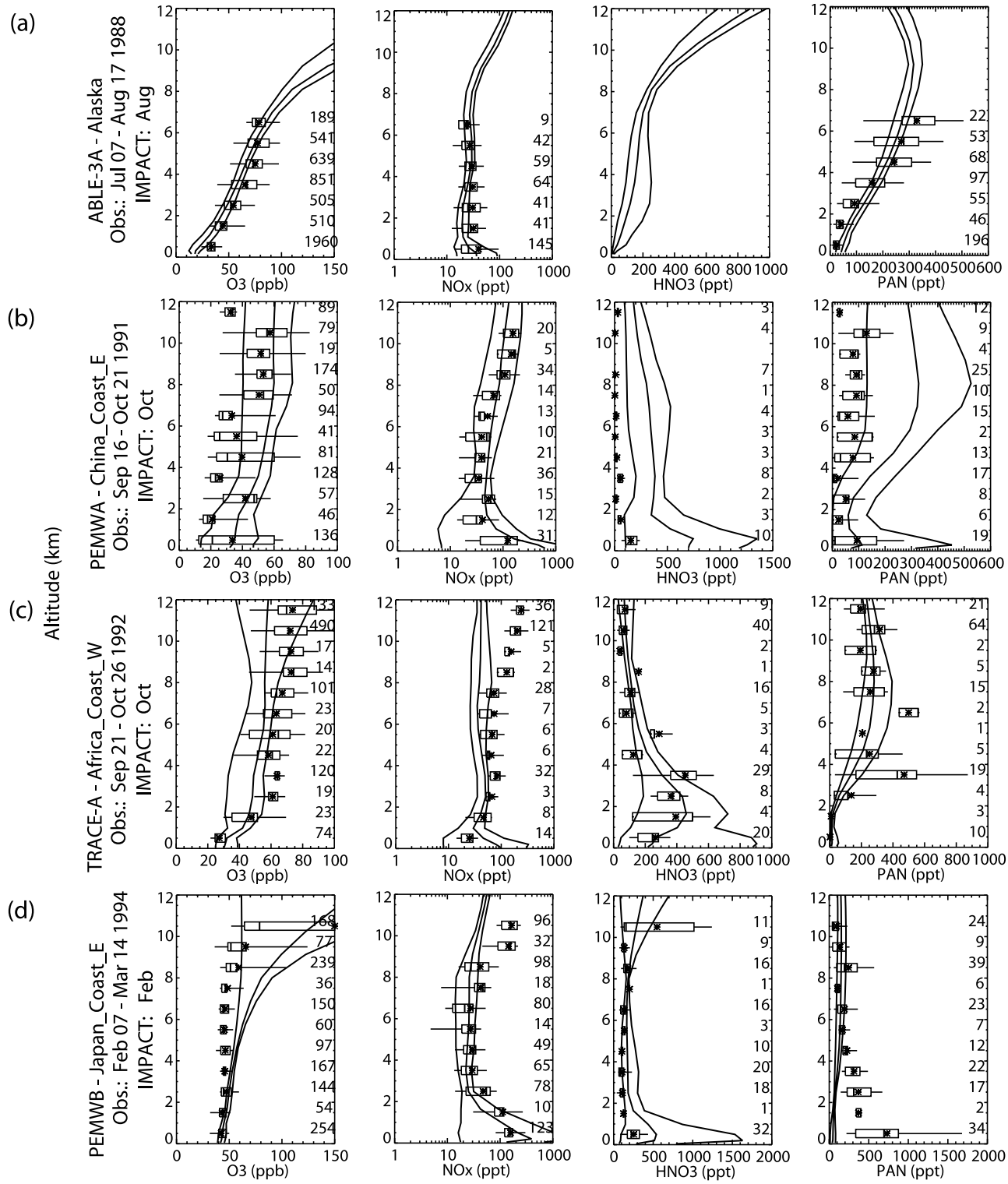

Figure 13. The observed and model-predicted concentrations of O_3 (ppbv), NO_x (pptv), HNO_3 (pptv), PAN (pptv), H_2O_2 (pptv), CO (ppbv), C_2H_6 (pptv), and C_3H_8 (pptv) for (a) ABLE-3A (Alaska, 7 July to 17 August 1988), (b) PEM-West A (China east coast, 16 September to 21 October 1991), (c) TRACE-A (Africa west coast, 21 September to 26 October 1992), and (d) PEM-West B (Japan east coast, 7 February to 14 March 1994). The box and whiskers indicate the central 50% and 90% of the observations, respectively, with a vertical bar at the median, and a star at the mean. The IMPACT values are represented by three lines: the minimum, mean, and maximum monthly average mixing ratios calculated for the grid boxes which encompass the actual sampling campaigns.

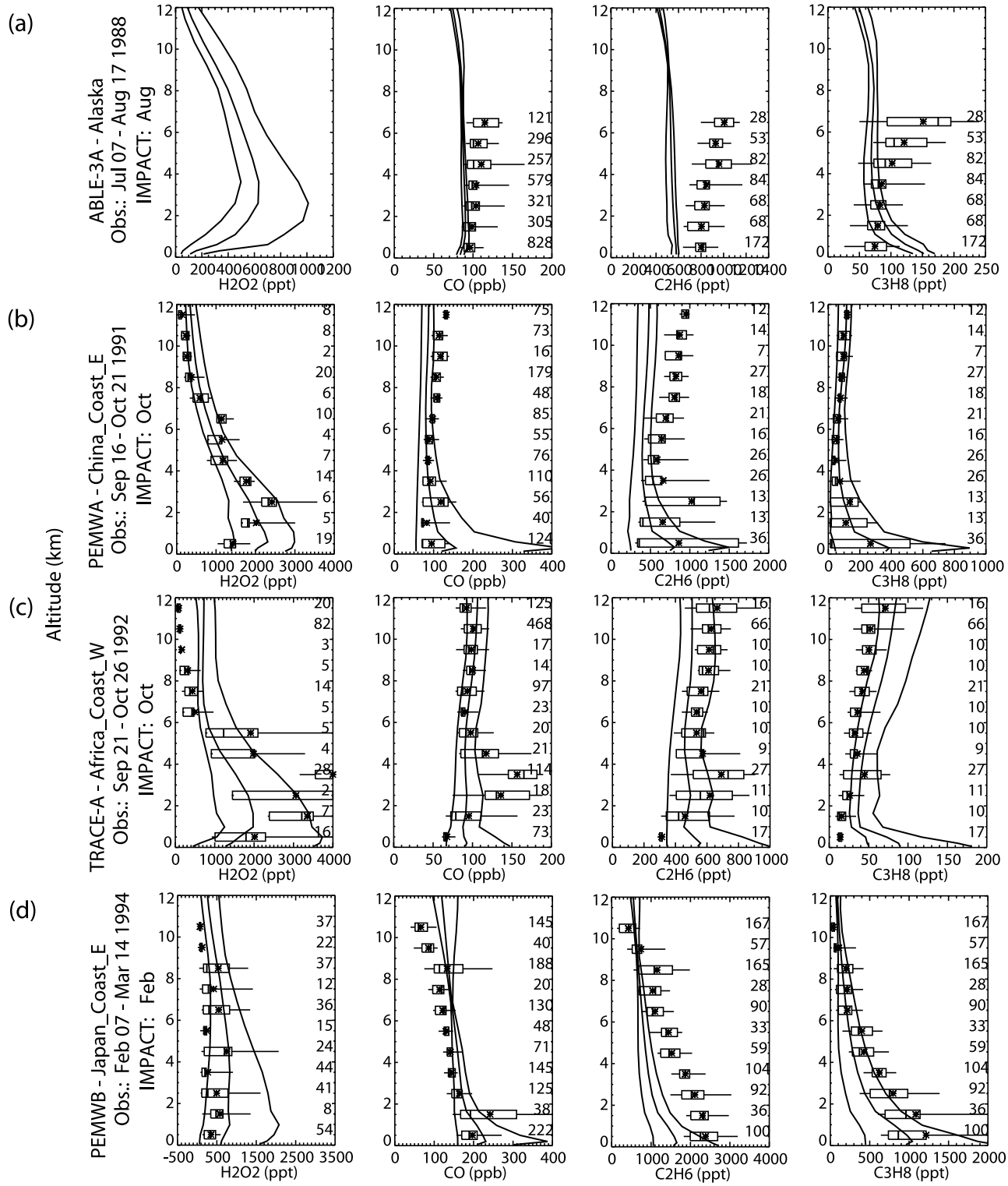

Figure 13. (continued)

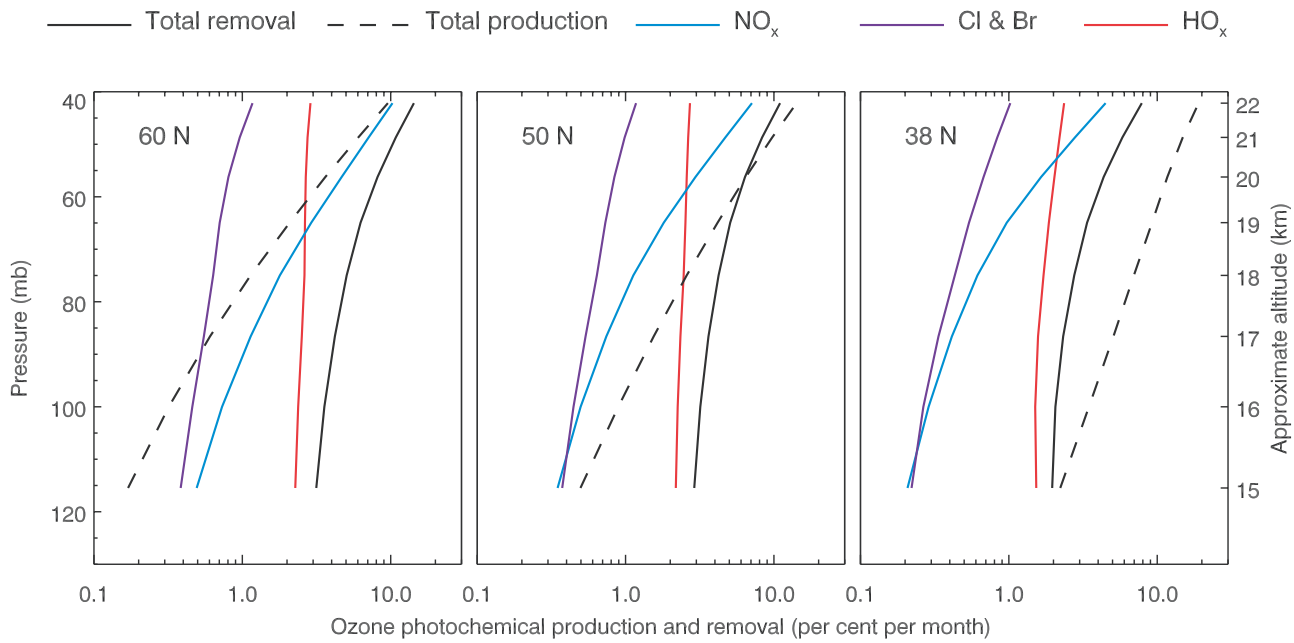

Figure 14. IMPACT May average ozone photochemical loss and production rates for 60°N, 50°N, and 38°N presented in units of the percent change in ozone per month. Radical catalytic cycle definitions follow *Wennberg et al.* [1994].

slightly low for ABLE and slightly high for PEM-West B. At most locations, the model underpredicts C_2H_6 concentrations between 30% and a factor of 2, indicating that the model emission source strength is low. A uniform trend is not apparent for C_3H_8.

4.5. Ozone-Controlling Radical Photochemistry in the Tropopause Region and Lower Stratosphere

[93] Data on radical abundances from instrumented aircraft flying in the lower stratosphere have yielded much important information on the specifics of this photochemistry. *Wennberg et al.* [1994] and *WMO* [1999] investigate ozone removal by radical families for three northern midlatitude locations and between 120 and 60 hPa, based on observations of the abundance of radical family members during the NASA SPADE ER-2 mission in 1993. Absolute removal rates and the relative contributions of radical families are inferred quantities because their derivation depends also on photochemical mechanism assumptions and laboratory-derived kinetic information. IMPACT includes updates to several of the rate constants in the *Wennberg et al.* [1994] analysis, of which several act to

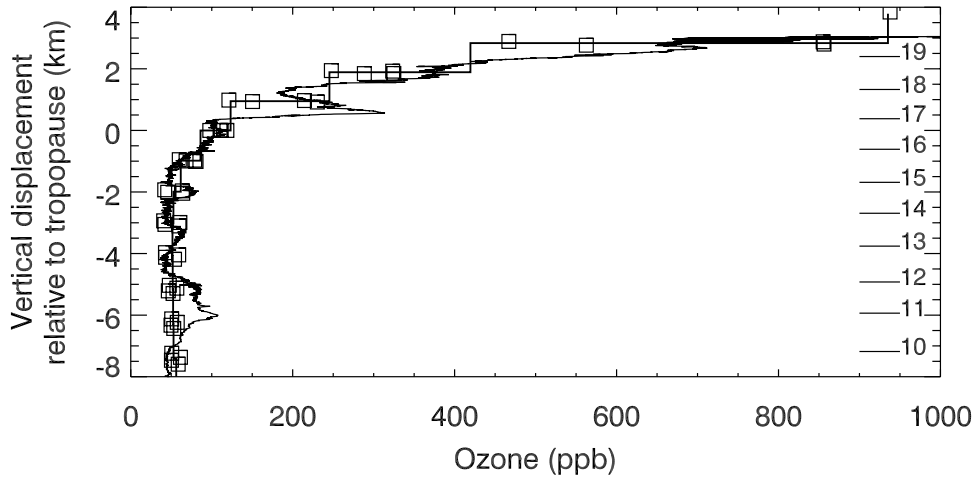

Figure 15. IMPACT ozone profiles at 95°W and 100°W, 30°N and 34°N, for 0000 GMT on 30 September (open squares) and their average (rectilinear solid line) compared to ACCENT WB-57 descent profile (jagged line) at approximately 30°N and 98°W on 22 September 1999. Simulation results and data plotted in distance from individual profile tropopause height. Scale height is taken from flight data.

increase somewhat the importance of the NO_x radical cycle relative to HO_x. Comparing IMPACT zonal monthly averages (Figure 14) for May to Figure 4 of *Wennberg et al.* [1994] and Figures 7–16 of *WMO* [1999], the IMPACT simulation produces total ozone loss removal rates (in per cent per month) that show the same trends and magnitudes as the observationally based inferences. While this may partly be the result of a buffering effect on ozone as its loss-controlling processes compete among themselves, it is a necessary precursor to predict ozone in this region.

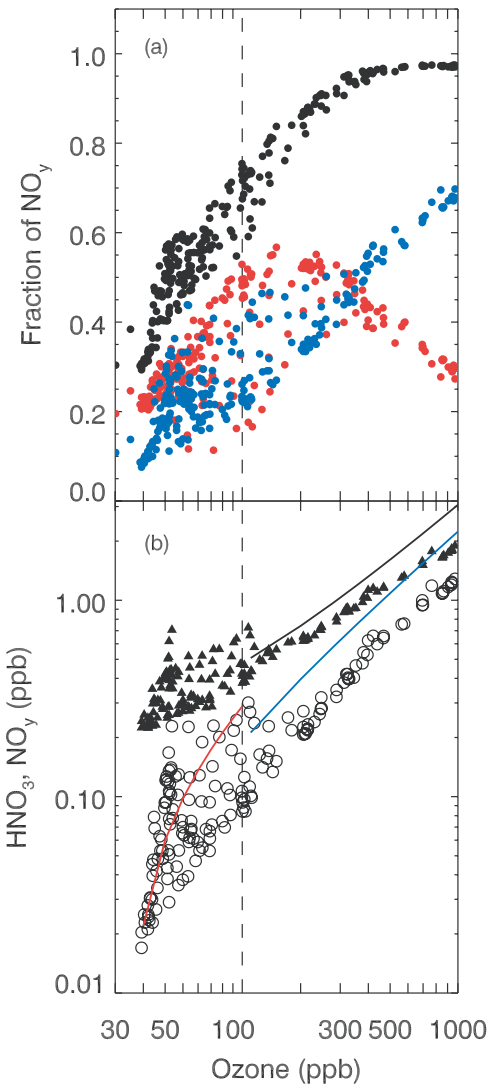

Figure 16. IMPACT nitrogen family abundance as a function of ozone abundance for points within a 25° longitude by 12° latitude box around the 22 September ACCENT flight. Following *Neuman et al.* [2001, Figure 4]. (a) Fractional abundance relative to total NO_y of HNO_3 (blue dots), NO_x (red dots), and HNO_3 + NO_x (black dots). (b) Abundance of HNO_3 (open circles) and NO_y (solid triangles). The black solid line is the *Neuman et al.* [2001] fit to the aircraft observations for NO_y in the lower stratosphere; the blue line is the lower stratospheric HNO_3 fit, and the red line the tropospheric HNO_3 fit.

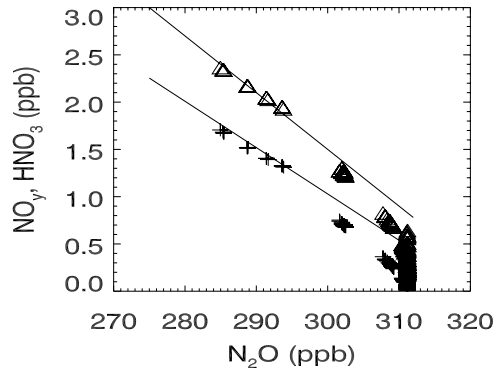

Figure 17. IMPACT HNO_3 (pluses) and NO_y abundance (triangles) as functions of N_2O abundance, in the region used in Figure 16. The solid lines are the fits to the observations depicted by *Neuman et al.* [2001, Figure 3].

[94] In comparing the relative contributions of the radical families in Figure 14 to the 1993 NASA/SPADE results, IMPACT shows a greater importance for NO_x-modulated loss cycles, relative to HO_x and halogen-modulated cycles. The HO_x cycle contribution to the total is roughly the correct magnitude. Changes in preferred kinetic values since the *Wennberg et al.* [1994] analysis may change the quantitative results of their work. The rate-determining step for NO_x mediated ozone destruction is now recommended to be about 15% faster than the recommendation used by *Wennberg et al.* [1994]. While additional recent changes in kinetic parameters of NO_x-NO_y conversion would support a larger proportional abundance of NO_x and therefore a larger role relative to the other cycles, direct observation of NO by Wennberg et al. establishes the NO_x abundance independent of NO_x-NO_y partitioning kinetics in their analysis.

[95] Other parameters, such as aerosol loading, can still play a role, however. *Wennberg et al.* [1994] point out that in May 1993, the presence of aerosol surface area from the recent eruption of Mount Pinatubo suppresses NO_x abundance relative to available NO_y and that NO_x could be 20–50% higher in a cleaner stratosphere. The IMPACT simulation uses a relatively clean aerosol loading climatology based on 1995 SAGE II observations over a period with small volcanic perturbation. The sensitivity of the IMPACT simulation to enhanced aerosol loading is a subject of future studies.

[96] *Neuman et al.* [2001] characterize observations of NO, NO_x, HNO_3, NO_y, and O_3 in the lower stratosphere and upper troposphere around 30°N during the NASA ACCENT WB-57 mission in 1999, when the effects of Mount Pinatubo have receded into the background. Using correlations between O_3 and HNO_3, NO_y, and NO_x, they distinguish between chemical regimes above and below the tropopause between 7 and 18 km. Because ozone can act as a proxy for the vertical coordinate in these correlations, it is first important to investigate IMPACT's ozone profiles near the tropopause. IMPACT comparisons to ozonesonde profiles are discussed above (section 4.3), with the general result that IMPACT ozone abundance often exceeds the sonde value. These comparisons are performed on long-

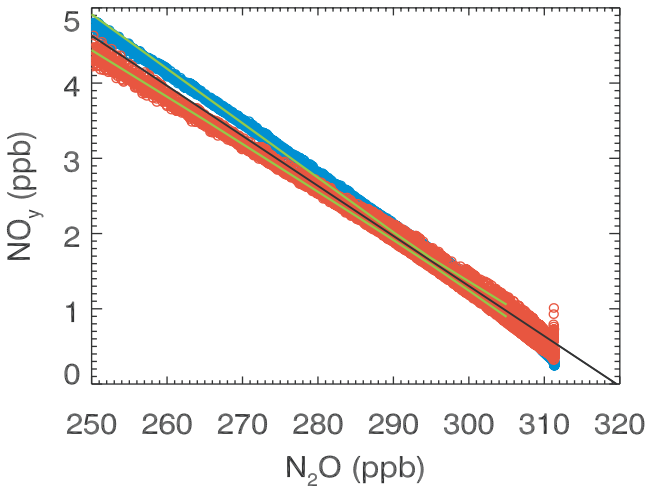

Figure 18. IMPACT NO_y abundance as a function of N_2O abundance for all points between 24°N and 64°N, at pressures less than 180 hPa. Blue points are January averages, red points are July. The black solid line is a linear least squares fit to all points within the plotting area for all months. The green line segments represent the envelope of least squares fits to the 12 sets of monthly correlations.

term temporal averages of both model output and atmospheric observation. Because the IMPACT MACCM3 simulation is not based on data assimilation, specific meteorological conditions, for example, those affecting the ACCENT mission, are not modeled.

[97] Various approaches to comparing model output to the 22 September 1999 mission results selected for discussion by *Neuman et al.* [2001] can be taken. Noting that the IMPACT simulation is climatological in nature, zonal or temporal averaging of the model result at the appropriate season and latitude could be argued. IMPACT ozone results averaged in this manner tend to be somewhat larger near the tropopause than the ACCENT observations, which will affect IMPACT O_3/NO_y correlation plots such as Figure 2 of *Neuman et al.* [2001]. Because temporal and zonal averaging may contribute to making the profile curvature near the tropopause less sharp, synoptic comparisons, even in the absence of an attempt to simulate specific meteorological conditions, may be more appropriate. Figure 15 shows the comparison of IMPACT simulated ozone profiles at the four nearest longitude/latitude grid points (open squares) and their average (thick solid line) to the 22 September ACCENT WB-57 descent profile (jagged line). The vertical coordinate for this comparison is displacement from the local tropopause, reported as 15.3 km for the ACCENT data, and calculated as the minimum in the expression

$$p_{tropopause} = \min(0.03*T - \log_{10}(p)),\ 550\,\text{mbar} > p > 40\,\text{mbar} \quad (11)$$

for the IMPACT profiles (J. Stobie, personal communication, 1999). Very good agreement in ozone abundance and curvature at the tropopause is seen in this figure. The vertical resolution of the MACCM3 grid in this pressure region is shown by the stack of lines on the right of the figure, labeled by vertical index number.

[98] Using the synoptic output for 30 September (the closest model time saved as a "snapshot" rather than a monthly average) and the matching longitude/latitude grid points, the IMPACT correlations for O_3 and HNO_3, NO_y, and NO_y partitioning are shown in Figure 16 (compare to Figure 2 of *Neuman et al.* [2001]). Figure 15 shows that the O_3 values in this figure are in good agreement with the ACCENT observations, so the noticeably larger fraction of NO_y that is contributed by NO_x at a given O_3 value is a strong indication that NO_x is simulated to be larger in the lower stratosphere than is observed. This result is reflected in the smaller fraction of HNO_3 and the lower HNO_3 abundance relative to the observationally derived least squares fit shown in Figure 16b. Total NO_y abundance is also lower than observed, so that the model's NO_x problem appears to be the result of partitioning problems, rather than NO_y source/sink terms. In this case, aerosol loading in 1999 has recovered from the high values following Mount Pinatubo, so, while the climatological values in IMPACT may or may not be too low, the effect should be much smaller than in the 1993 comparison to observations.

[99] Additional evidence that IMPACT stratospheric NO_y is not overpredicted is shown in Figure 17, which shows the IMPACT N_2O/NO_y and N_2O/HNO_3 correlation, where the lines represent the linear fits from Figure 3 of *Neuman et al.* [2001]. The slopes represent conversion efficiency of N_2O to NO_y and IMPACT matches the observations in the lower stratosphere somewhat away from the tropopause. A more global representation is shown in Figure 18, including points from all longitudes between 26°N and 62°N, with pressure below 180 hPa, and N_2O between 250 ppb and 310 ppb. The center black line is a fit to results from all months and has a slope of −0.067. The green lines represent the envelope to least squares fits for all months individually. The blue points are for January only and the red points for July only. *Olsen et al.* [2001] suggest a slope from combined observations of −0.073, or somewhat greater net NO_y production from N_2O in the stratosphere than IMPACT simulates. We also note slightly smaller peak NO_y values in the IMPACT middle stratosphere than satellite and in situ observations.

[100] This apparent overprediction of NO_x leads to an overemphasis on NO_x cycles in ozone removal rates. Higher NO_2 levels will also suppress active chlorine by converting ClO to $ClONO_2$, and diminish the simulated importance of ClO_x in destroying ozone. These behaviors may be symptoms of aerosol surface area densities that are below actual characteristic levels in the lower stratosphere, or NO_x conversion and Cl activation rates that are too slow because of errors in kinetic parameters or, possibly, temperatures higher than lower stratosphere ambient.

5. Conclusions

[101] In this paper, we present a description of the LLNL IMPACT atmospheric chemistry model, which treats chemical and physical processes in the troposphere, stratosphere, and the climatically critical tropopause region, allowing for physically based simulations of past, present, and future ozone and its precursors. Being able to model the effects of

Table A1. Photochemical Reactions (Gas Phase) Included in IMPACT

Thermal Reactions	Arrhenius A	Arrhenius E/R[a]	Troe[b] k_0^{300}	Troe n	Troe k_∞^{300}	Troe m	Unimolecular K_{eq}[c]	Source/Note[d]
Oxygen Species								
$O + O_2 \rightarrow O_3$			6.0e-34	2.4	0.	0.		JPL 00-003[e]
$O + O_3 \rightarrow 2\ O_2$	8.0e-12	2060.						
$O(^1D) + N_2 \rightarrow O + N_2$	1.8e-11	−110.						
$O(^1D) + O_2 \rightarrow O + O_2$	3.2e-11	−70.						
$O(^1D) + O_3 \rightarrow 2\ O_2$	1.2e-10	0.						
Hydrogen/Oxygen Species								
$H_2 + O(^1D) \rightarrow OH + H$	1.1e-10	0.						
$H_2O + O(^1D) \rightarrow 2\ OH$	2.2e-10	0.						JPL 00-003
$H + O_2 \rightarrow HO_2$			5.7e-32	1.6	7.50e-11	0.		
$H + O_3 \rightarrow OH + O_2$	1.4e-10	470.						
$H + HO_2 \rightarrow 2\ OH$	7.0e-11	0.						products: JPL 97-4 Note B5[f]
$OH + O \rightarrow H + O_2$	2.2e-11	−120.						
$OH + O_3 \rightarrow HO_2 + O_2$	1.5e-12	880.						JPL 00-003
$OH + H_2 \rightarrow H + H_2O$	5.5e-12	2000.						
$OH + OH \rightarrow O + H_2O$	4.2e-12	240.						
$HO_2 + O \rightarrow OH + O_2$	3.0e-11	−200.						JPL 00-003
$HO_2 + O_3 \rightarrow OH + 2\ O_2$	2.0e-14	680.						JPL 00-003
$HO_2 + OH \rightarrow H_2O + O_2$	4.8e-11	−250.						JPL 00-003
$HO_2 + HO_2 \rightarrow H_2O_2 + O_2$								k(298 K): 1.7e-12 + 4.9e-32*[M][g]
$HO_2 + HO_2 + H_2O \rightarrow H_2O_2 + O_2 + H_2O$								k(298 K): k($HO_2 + HO_2$) * 6.75e-09 JPL 97-4 Note B13[h]
$H_2O_2 + OH \rightarrow HO_2 + H_2O$	2.9e-12	160.						
Nitrogen/Hydrogen/Oxygen Species								
$N_2O + O(^1D) \rightarrow N_2 + O_2$	4.9e-11	0.						JPL 00-003
$N_2O + O(^1D) \rightarrow 2\ NO$	6.7e-11	0.						JPL 00-003
$N + O_2 \rightarrow NO + O$	1.5e-11	3600.						
$NO + O_3 \rightarrow NO_2 + O_2$	3.0e-12	1500.						JPL 00-003
$NO_2 + O \rightarrow NO + O_2$	5.6e-12	−180.						JPL 00-003
$NO_2 + O_3 \rightarrow NO_3 + O_2$	1.2e-13	2450.						
$NO + OH \rightarrow HONO$			7.0e-31	2.6	3.6e-11	0.1		
$NO + HO_2 \rightarrow NO_2 + OH$	3.5e-12	−250.						
$NO_2 + OH \rightarrow HNO_3$			2.4e-30	3.1	1.7e-11	2.1		JPL 00-003
$NO_2 + HO_2 \rightarrow HO_2NO_2$			1.8e-31	3.2	4.7e-12	1.4		
$N_2O_5 + H_2O \rightarrow 2\ HNO_3$	5.0e-22	0.						JPL 97-4 Note C32[i]
$HO_2NO_2 \rightarrow HO_2 + NO_2$							2.1e-27 * exp(10900/T)	
$HONO + OH \rightarrow H_2O + NO_2$	1.8e-11	390.						
$HNO_3 + OH \rightarrow H_2O + NO_3$								JPL 00-003 Note C9[j]
$HO_2NO_2 + OH \rightarrow H_2O + NO_2 + O_2$	1.3e-12	−380.						limited guidance on products
$N + NO \rightarrow N_2 + O$	2.1e-11	−100.						
$NO_3 + NO \rightarrow 2\ NO_2$	1.5e-11	−170.						
$NO_3 + NO_2 \rightarrow N_2O_5$			2.0e-30	4.4	1.4e-12	0.7		JPL 00-003
$N_2O_5 \rightarrow NO_2 + NO_3$							3.0e-27 * exp(10991/T)	JPL 00-003

Table A1. (continued)

Thermal Reactions	Arrhenius A	Arrhenius E/R[a]	Troe[b] k_0^{300}	Troe n	Troe k_∞^{300}	Troe m	Unimolecular K_{eq}[c]	Source/Note[d]
Chlorine Radical Species								
$Cl + O_3 \rightarrow ClO + O_2$	2.3e-11	200.						JPL 00-003
$ClO + O \rightarrow Cl + O_2$	3.0e-11	−70.						JPL 00-003
$ClONO_2 + O \rightarrow ClO + NO_3$	4.5e-12	900.						*Goldfarb et al.* [1998]
$Cl + H_2 \rightarrow HCl + H$	3.7e-11	2300.						
$Cl + HO_2 \rightarrow HCl + O_2$	1.8e-11	−170.						
$Cl + HO_2 \rightarrow OH + ClO$	4.1e-11	450.						
$Cl + H_2O_2 \rightarrow HCl + HO_2$	1.1e-11	980.						
$ClO + OH \rightarrow HO_2 + Cl$	7.4e-12	−270.						JPL 00-003
$ClO + OH \rightarrow HCl + O_2$	3.2e-13	−320.						JPL 00-003
$ClO + HO_2 \rightarrow O_2 + HOCl$	4.8e-13	−700.						branching ratio: JPL 97-4 Note F43
$ClO + HO_2 \rightarrow O_3 + HCl$	0.0e-00	0.						branching ratio: JPL 97-4 Note F43
$HCl + OH \rightarrow H_2O + Cl$	2.6e-12	350.						JPL 00-003
$HOCl + OH \rightarrow H_2O + ClO$	3.0e-12	500.						
$ClONO_2 + OH \rightarrow HOCl + NO_3$	1.2e-12	330.						limited guidance on products
$ClO + NO \rightarrow NO_2 + Cl$	6.4e-12	−290.						
$ClO + NO_2 \rightarrow ClONO_2$			1.8e-31	3.4	1.5e-11	1.9		JPL 00-0003
$ClO + ClO \rightarrow Cl_2 + O_2$	1.0e-12	1590.						
$ClO + ClO \rightarrow Cl + ClOO$	3.0e-11	2450.						
$ClO + ClO \rightarrow Cl + OClO$	3.5e-13	1370.						
$ClO + ClO \rightarrow Cl_2O_2$			2.2e-32	3.1	3.4e-12	1.0		JPL 00-003
$Cl_2O_2 \rightarrow 2\ ClO$							1.27e-27 * exp(8744/T)	JPL 00-003
$HOCl + Cl \rightarrow HCl + ClO$	2.5e-12	130.						limited guidance on products JPL 97-4 Note F69
$ClONO_2 + Cl \rightarrow Cl_2 + NO_3$	6.5e-12	−135.						products: JPL 97-4 Note F71
Bromine Radical Species								
$Br + O_3 \rightarrow BrO + O_2$	1.7e-11	800.						
$BrO + O \rightarrow Br + O_2$	1.9e-11	−230.						
$Br + HO_2 \rightarrow HBr + O_2$	1.5e-11	600.						
$BrO + OH \rightarrow Br + HO_2$	7.5e-11	0.						products: JPL 97-4 Note G5
$BrO + HO_2 \rightarrow HOBr + O_2$	3.4e-12	−540.						products: JPL 97-4 Note G21
$HBr + OH \rightarrow Br + H_2O$	1.1e-11	0.						
$BrO + NO \rightarrow Br + NO_2$	8.8e-12	−260.						
$BrO + NO_2 \rightarrow BrONO_2$			5.2e-31	3.2	6.9e-12	2.9		JPL 00-003
$BrO + ClO \rightarrow Br + OClO$	9.5e-13	−550.						JPL 00-003
$BrO + ClO \rightarrow BrClOO$	2.3e-12	−260.						JPL 00-003
$BrO + ClO \rightarrow BrCl + O_2$	4.1e-13	−290.						JPL 00-003
$BrO + BrO \rightarrow 2\ Br + O_2$	2.4e-12	−40.						branching ratio: JPL 97-4 Note G37
Halogen Source Species								
$CF_2Cl_2 + O(^1D) \rightarrow 2\ Cl$	1.20e-10	0.						branching ratio: JPL 97-4 Notes A2,A15
$CH_3Cl + OH \rightarrow Cl$	4.0e-12	1400.						carbon containing fragment ignored as insignificant atmospheric source relative to methane

Table A1. (continued)

Thermal Reactions	Arrhenius A	Arrhenius E/R[a]	Troe k_0^{300}	Troe n	Troe k_∞^{300}	Troe m	Unimolecular K_{eq}[c]	Source/Note[d]
$CH_3Br + OH \rightarrow Br$	4.0e-12	1470.						carbon containing fragments ignored as insignificant atmospheric source relative to methane
$CH_3CCl_3 + OH \rightarrow 3\ Cl$	1.8e-12	1550.						carbon containing fragments ignored as insignificant atmospheric source relative to methane
$CH_3Cl + Cl \rightarrow Cl + HCl$	3.2e-11	1250.						carbon containing fragments ignored as insignificant atmospheric source relative to methane
C_1 Hydrocarbons								
$CH_4 + O(^1D) \rightarrow CH_3O_2 + OH$	1.125e-10	0.						combined reaction[k]
$CH_4 + O(^1D) \rightarrow CH_2O + H + HO_2$	3.0e-11	0.						combined reaction[k]
$CH_4 + O(^1D) \rightarrow CH_2O + H_2$	7.5e-12	0.						branching ratio: JPL 97-4 Note A9
$CH_2O + O \rightarrow HO_2 + OH + CO$	3.4e-11	1600.						combined reaction[k]
$CH_4 + OH \rightarrow CH_3O_2 + H_2O$	2.45e-12	1775.						combined reaction[k]
$CO + OH \rightarrow H$								k(298 K): 1.5e-13 * (1 + 0.6 P(in atm))
$CH_2O + OH \rightarrow H_2O + HO_2 + CO$	1.0e-11	0.						combined reaction[k]
$CH_3OH + OH \rightarrow CH_2O + H_2O + HO_2$	6.7e-12	600.						combined reaction[k]
$CH_3OOH + OH \rightarrow CH_3O_2 + H_2O$	2.7e-12	−200.						branching ratio: JPL 97-4 Note D15
$CH_3OOH + OH \rightarrow CH_2O + H_2O + OH$	1.1e-12	−200.						branching ratio: JPL 97-4 Note D15
$CH_3O_2 + HO_2 \rightarrow CH_3OOH + O_2$	3.8e-13	−800.						
$CH_3O_2 + NO \rightarrow HO_2 + CH_2O + NO_2$	3.0e-12	−280.						combined reaction[k]
$CH_3O_2 + NO_2 \rightarrow HO_2 + CH_3O_2NO_2$			1.5e-30	4.0	6.5e-12	2.0		
$CH_3O_2NO_2 \rightarrow CH_3O_2 + NO_2$							1.3e-28 * exp(11200/T)	
$CH_3O_2 + CH_3O_2 \rightarrow 1.33\ CH_2O + 0.66\ CH_3OH + 0.80\ HO_2$	2.5e-13	−190.						Products represent the condensation of products from multiple reaction pathways
$CH_2O + HO_2 \rightarrow CH_3O_3$	6.7e-15	−600.						
$CH_3O_3 \rightarrow CH_2O + HO_2$	2.4e+12	7000.						*Atkinson et al.* [1997]
$CH_3O_3 + NO \rightarrow HCOOH + NO_2 + HO_2$	3.0e-12	−280.						= k(CH_3O_2 + NO)
$CH_3O_3 + HO_2 \rightarrow HCOOH$	5.6e-15	−2300.						*Atkinson et al.* [1997]
$Cl + CH_4 \rightarrow CH_3O_2 + HCl$	9.6e-12	1360.						combined reaction[k]
$Cl + CH_2O \rightarrow HCl + HO_2 + CO$	8.1e-11	30.						combined reaction[k]
$Br + CH_2O \rightarrow HBr + HO_2 + CO$	1.7e-11	800.						
$CH_3O_3 + CH_3O_3 \rightarrow 2HCOOH + 2\ HO_2$	5.7e-14	−750.						*Atkinson et al.* [1997]
$HCOOH + OH \rightarrow HO_2 + CO$	4.0e-13	0.						products: JPL 97-4 Note D16
C_2 Hydrocarbons								
$C_2H_6 + OH \rightarrow ETO2$	8.7e-12	1070.						combined reaction[k]
$C_2H_6 + Cl \rightarrow HCl + ETO2$	7.7e-11	90.						combined reaction[k]
$ETO2 + HO_2 \rightarrow ETP$	7.5e-13	−700.						limited guidance on products
$ETO2 + NO \rightarrow ALD2 + NO_2 + HO_2$	2.6e-12	−365.						
$ETO2 + ETO2 \rightarrow 1.60\ ALD2 + 1.20\ HO_2$	6.8e-14	0.						products: JPL 97-4 D48, ignore 0.40 ethanol

Table A1. (continued)

Thermal Reactions	Arrhenius A	Arrhenius E/R[a]	Troe[b] k_0^{300}	Troe n	Troe k_∞^{300}	Troe m	Unimolecular K_{eq}[c]	Source/Note[d]
ETP + OH → 0.50 ETO2 + 0.50 ALD2 + 0.50 OH	3.0e-12	−190.						*Baulch et al.* [1992]
ALD2 + OH → MCO3	5.6e-12	−270.						combined reaction[k]
ALD2 + NO_3 → MCO3 + HNO_3	1.4e-12	1900.						products: JPL 97-4 Note D34[k]
MCO3 + HO_2 → 0.75 MAP + 0.25 O_3	4.5e-13	−1000.						products: JPL 97-4 Note D31, ignore 0.25 ethanol
MCO3 + NO → CH_3O_2 + NO_2	5.3e-12	−360.						
MCO3 + CH_3O_2 → CH_2O + 0.90 CH_3O_2 + 0.90 HO_2	1.3e-12	−640.						products: JPL 97-4 Note D45
MCO3 + MCO3 → 2.00 CH_3O_2	2.9e-12	−500.						products: JPL 97-4 Note D50
MCO3 + NO_2 → PAN			9.7e-29	5.6	9.3e-12	1.5		
PAN → MCO3 + NO_2							9.0e-29 * exp(14000/T)	
GLYX + OH → HO_2 + 2.00 CO	1.1e-11	0.						*Atkinson et al.* [1997]
C_3 Hydrocarbons								
C_3H_8 + OH → A302	1.0e-11	660.						
C_3H_8 + Cl → HCl + A302	1.2e-10	−40.						
A3O2 + HO2 → RA3P	1.66e-13	−1300.						*Kircher and Stockwell* [1996]
A3O2 + NO → 0.16 RCHO + 0.968 NO_2 + 0.968 HO_2 + 0.82 ACET	2.9e-12	−350.						*Eberhard and Howard* [1996]; ignore 0.032 A3N2 product
A3O2 + A3O2 → 1.20 RCHO + 0.40 ALD2 + 1.20 HO_2	3.0e-13	0.						*Atkinson et al.* [1997], ignore product 0.40 ethanol
RA3P + OH → 0.50 A3O2 + 0.50 RCHO + 0.50 OH	3.0e-12	−190.						= k(ETP + OH)
ACET + OH → ATO2	2.2e-12	685.						
ATO2 + HO_2 → MCO3 + CH_3O_2	1.15e-13	−1300.						*Kirchner and Stockwell* [1996] R28
ATO2 + NO → 0.96 MGLY + 0.96 NO_2 + 0.96 HO_2	8.0e-12	0.						*Sehested et al.* [1998], ignore product 0.04 R4N2
MGLY + OH → MCO3 + CO	1.5e-11	0.						*Atkinson et al.* [1997]
RCHO + OH → ECO3	2.0e-11	0.						*Atkinson et al.* [1997]
RCHO + NO_3 → HNO_3 + ECO3	5.7e-15	0.						*D'Anna and Nielsen* [1997]
ECO3 + HO_2 → 0.75 + 0.25 O_3	4.5e-13	−1000.						= k(MCO3 + HO_2); ignore product 0.25 ethanol
ECO3 + NO → ETO2 + NO_2	2.0e-11	0.						*Atkinson et al.* [1997]
CH_3O_2 + ECO3 → 0.85 ETO2 + CH_2O + 0.5 HO_2	1.3e-12	−640.						= k(CH_3O_2 + MCO3); ignore product 0.15 EOH
MCO3 + ECO3 → ETO2 + CH_3O_2	2.9e-12	−500.						= k(MCO3 + MCO3)
ECO3 + ECO3 → 2.00 ETO2	2.9e-12	−500.						= k(MCO3 + MCO3)
ECO3 + NO_2 → PPN			9.7e-29	5.6	9.3e-12	1.5		= k(PAN formation)
PPN → ECO3 + NO_2							9.0e-29 * exp(14000/T)	= k(PAN thermal decomposition)
RP + OH → 0.50 ECO3 + 0.50 ALD2 + 0.50 OH	3.0e-12	−190.						= k(ETP + OH)
Isoprene Oxidation Species								
ISOP + OH → RIO2	2.55e-11	−409.						*Paulson and Seinfeld* [1992][l]
MVK + OH → VRO2	2.67e-12	−452.						*Gierczak et al.* [1997]
MACR + OH → MAO3	3.90e-12	−379.						* 0.5 (stoichiometric factor), *Gierczak et al.* [1997]

Table A1. (continued)

Thermal Reactions	Arrhenius A	Arrhenius E/R[a]	Troe k_0^{300}	Troe n	Troe k_∞^{300}	Troe m	Unimolecular K_{eq}[c]	Source/Note[d]
MACR + OH → MRO2	3.90e-12	−379.						* 0.5 (stoichiometric factor), *Gierczak et al.* [1997]
HAC + OH → GLYX + HO_2	6.70e-13	−270.						= k(CH_3CHO + OH), branching ratio *Niki et al.* [1987]
HAC + OH → HACO	2.38e-12	−270.						= k(CH_3CHO + OH), branching ratio *Niki et al.* [1987]
ISOP + O_3 → 0.80 CH_2O + 0.26 MVK + 0.67 MACR + 0.07 CH_3OH + 0.55 OH + 0.06 HO_2 + 0.05 CO	5.59e-15	1814.						*Grosjean and Grosjean* [1996]; ignore product: 0.07 PRPE
MVK + O_3 → 0.80 CH_2O + 0.82 MGLY + 0.07 MRO2 + 0.04 ALD2 + 0.08 OH + 0.06 HO_2 + 0.05 CO	6.91e-16	1519.						*Treacy et al.* [1992]; ignore product: 0.11 CHO_2
MACR + O_3 → 0.70 CH_2O + 0.80 MGLY + 0.15 MRO2 + 0.215 OH + 0.21 HO_2	1.30e-15	2112.						*Treacy et al.* [1992]; ignore product: 0.09 CHO_2
RIP + O_3 → 0.7 CH_2O	8.00e-18	0.						*Paulson and Seinfeld* [1992][l]
VRP + O_3 → 0.7 CH_2O	8.00e-18	0.						*Paulson and Seinfeld* [1992][l]
MRP + O_3 → 0.7 CH_2O	8.00e-18	0.						*Paulson and Seinfeld* [1992][l]
ISOP + NO_3 INO_2	3.03e-12	450.						*Dlugokencky and Howard* [1989]
MACR + NO_3 → MAO3 + HNO_3	1.10e-15	0.						*Chew et al.* [1998], product split *Lurmann* [1986]
MACR + NO_3 → MAN2	2.20e-15	0.						*Chew et al.* [1998], product split *Lurmann* [1986]
RIO2 + NO → 0.42 MVK + 0.32 MACR + 0.74 CH_2O + 0.14 ISN1 + 0.12 RIO2 + 0.86 NO_2 + 0.78 HO_2	2.90e-12	−350.						= k(n-propyl peroxy + NO); *Eberhard and Howard* [1996] (in manner of *Kirchner and Stockwell* [1996])

Table A1. (continued)

Thermal Reactions	Arrhenius A	Arrhenius E/R[a]	Troe k_0^{300}	Troe n	Troe k_∞^{300}	Troe m	Unimolecular K_{eq}[c]	Source/Note[d]
VRO2 + NO → 0.68 HAC + 0.27 MGLY + 0.27 CH_2O + 0.68 MCO3 + 0.05 ISN1 + 0.95 NO_2 + 0.27 H_2O	2.90e-12	−350.						= k(n-propyl peroxy + NO); *Eberhard and Howard* [1996] (in manner of *Kirchner and Stockwell* [1996])
MAO3 + NO → MAO2	8.69e-12	−290.						*deGouw and Howard* [1997]
MAO2 + NO → CH_2O + NO_2 + MCO3	4.20e-12	−180.						no specific indication from references cited herein[m]
MRO2 + NO → HACN + NO_2 + HO_2	2.90e-12	−350.						= k(n-propyl peroxy + NO); *Eberhard and Howard* [1996] (in manner of *Kirchner and Stockwell* [1996])
HACO + NO → CH_3O_3 + NO_2	5.30e-12	−360.						= k(acetyl peroxy + NO), in manner of *Kirchner and Stockwell* [1996]
INO2 + NO → 0.05 MVK + 0.1 MACR + 0.15 CH_2O + 1.25 NO_2 + 0.75 ISN1 + 0.8 H_2O	2.90e-12	−350.						= k(n-propyl peroxy + NO); *Eberhard and Howard* [1996] (in manner of *Kirchner and Stockwell* [1996])
ISNR + NO → 0.05 ISN1 + 0.05 HO_2 + 1.9 HAC + 0.95 ACET + 1.9 NO_2	2.90e-12	−350.						= k(n-propyl peroxy + NO); *Eberhard and Howard* [1996] (in manner of *Kirchner and Stockwell* [1996])
MAN2 + NO → MGLY + $2NO_2$ + HO_2	2.90e-12	−350.						= k(n-propyl peroxy + NO); *Eberhard and Howard* [1996] (in manner of *Kirchner and Stockwell* [1996])
RIO2 + HO_2 → RIP	1.66e-13	−1300.						*Kirchner and Stockwell* [1996] R28
VRO2 + HO_2 → VRP	1.66e-13	−1300.						*Kirchner and Stockwell* [1996] R28
MAO3 + HO_2 → RP	1.15e-12	−550.						*Kirchner and Stockwell* [1996] R28; R29 in Table 7
MRO2 + HO_2 → MRP	1.66e-13	−1300.						*Kirchner and Stockwell* [1996] R28
HACO + HO_2 → CH_3OOH	1.15e-12	−550.						*Kirchner and Stockwell* [1996] R28; R29 in Table 7 (substituted peroxy alcohol for peroxy carboxylic acid)
ISNR + HO_2 → PRN2	1.40e-13	−1380.						*Horowitz et al.* [1998]; (ISN1 + HO_2)
INO2 + HO_2 → PRN2	1.40e-13	−1380.						*Horowitz et al.* [1998]; (INO2 + HO_2)
MAN2 + HO_2 → PRN2	1.40e-13	−1380.						*Horowitz et al.* [1998]; (MAN2 + HO_2)
INO2 + NO_2 → 2.0 PRN2	4.20e-13	−180.						S. Sillman, private communication, 1997
HACN + OH → MGLY + HO_2	3.00e-12	0.						*Atkinson et al.* [1997]

Table A1. (continued)

Thermal Reactions	Arrhenius A	Arrhenius E/R[a]	Troe[b] k_0^{300}	Troe n	Troe k_∞^{300}	Troe m	Unimolecular K_{eq}[c]	Source/Note[d]
ISN1 + OH → ISNR	3.35e-11	0.						R67, *Paulson and Seinfeld* [1992][l]
RIP + OH → 0.5 RIO2 + HO_2 + 0.16 MACR + 0.21 MVK + 0.37 CH_2O	3.80e-12	−200.						*Horowitz et al.* [1998]; products uncertain
VRP + OH → VRO2 + 0.5 HAC + HO_2	3.80e-12	−200.						*Horowitz et al.* [1998]; products uncertain
MAP + OH → 0.50 MCO3 + 0.50 CH_2O + 0.50 OH	3.00e-12	−190.						= k(ETP + OH)
MRP + OH → 0.5 MRO2 + 0.5 HAC + HO_2	3.80e-12	−200.						*Horowitz et al.* [1998]; products uncertain
PRN2 + OH → 0.5 OH + 0.5 RCHO + 0.5 NO_2 + 0.5 ISNR	3.80e-12	−200.						*Horowitz et al.* [1998]
MAO3 + HO_2 → CH_2O + O_3 + ETO2	3.86e-16	−2640.						*Kirchner and Stockwell* [1996]; R30 in Table 7, ignore products ethanol, carboxylic acid
MAO2 + HO_2 → O_3 + ACET	3.86e-16	−2640.						*Kirchner and Stockwell* [1996]; limited guidance for products
HACO + HO_2 → ETO2 + O_3	3.86e-16	−2640.						*Kirchner and Stockwell* [1996]; R30 in Table 7, ignore products ethanol, carboxylic acid
MAO3 + NO_2 → MPAN			9.7e-29	5.6	9.3e-12	1.5		= k(CH_3O_2 + NO_2 → PAN
MPAN → MAO3 + NO_2							9.0e-29 * exp(14000/T)	= k(PAN thermal decomposition)
HACO + NO_2 → IPAN			9.7e-29	5.6	9.3e-12	1.5		= k(CH_3O_2 + NO_2 → PAN)
IPAN → HACO + NO_2							9.0e-29 * exp(14000/T)	= k(PAN thermal decomposition)
CH_3O_2 + MAO3 → 0.85 MAO2 + CH_2O + 0.5 HO_2	1.3e-12	−640.						= k(CH_3O_2 + MCO3); ignore products: 0.15 ethanol
MCO3 + MAO3 → MAO2 + CH_3O_2	2.9e-12	−500.						= k(MCO3 + MCO3)
MAO3 + MAO3 → 2 MAO2	2.9e-12	−500.						= k(MCO3 + MCO3)
CH_3O_2 + HACO → 0.85 CH_3O_2 + CH_2O + 0.5 HO_2	1.3e-12	−640.						= k(CH_3O_2 + MCO3); ignore products: 0.15 ethanol
MCO3 + HACO → 2 CH_3O_2	2.9e-12	−500.						= k(MCO3 + MCO3)
HACO + HACO → 2 CH_3O_2	2.9e-12	−500.						= k(MCO3 + MCO3)

Photolysis Processes	Arrhenius A	Arrhenius E/R[a]	Troe[b] k_0^{300}	Troe n	Troe k_∞^{300}	Troe m	Unimolecular K_{eq}[c]	Source/Note[d]
O_2 + *hv* → 2 O								R. Kawa, personal communication, 1999, based on work of *Minschwaner et al.* [1992]
O_3 + *hv* → O + O_2								
O_3 + *hv* → O(^{1}D) + O_2								
N_2O + *hv* → N_2 + O(^{1}D)								
NO + *hv* → N + O								D. Weisenstein and M. Ko, personal communication, 1999
NO_2 + *hv* → NO + O								
NO_3 + *hv* → NO + O_2								
NO_3 + *hv* → NO_2 + O								
N_2O_5 + *hv* → NO_2 + NO_3								
HONO + *hv* → OH + NO								

Table A1. (continued)

Thermal Reactions	Arrhenius A	Arrhenius E/R[a]	Troe k_0^{300}	Troe n	Troe k_∞^{300}	Troe m	Unimolecular K_{eq}[c]	Source/Note[d]
$HNO_3 + h\nu \rightarrow OH + NO_2$								
$HO_2NO_2 + h\nu \rightarrow HO_2 + NO_2$								
$HO_2NO_2 + h\nu \rightarrow OH + NO_3$								
$H_2O + h\nu \rightarrow H + OH$								
$HO_2 + h\nu \rightarrow OH + O$								
$H_2O_2 + h\nu \rightarrow 2\ OH$								
$ClO + h\nu \rightarrow Cl + O$								
$ClO + h\nu \rightarrow Cl + O(^1D)$								
$HCl + h\nu \rightarrow H + Cl$								
$HOCl + h\nu \rightarrow OH + Cl$								*Sander et al.* [2000]
$Cl_2 + h\nu \rightarrow 2\ Cl$								
$OClO + h\nu \rightarrow O + ClO$								
$Cl_2O_2 + h\nu \rightarrow 2\ Cl + O_2$								*Sander et al.* [2000]
$ClONO_2 + h\nu \rightarrow Cl + NO_3$								
$ClONO_2 + h\nu \rightarrow Cl + NO_2 + O$								
$BrO + h\nu \rightarrow Br + O$								= σ(HCl) red shifted by 30 nm
$HBr + h\nu \rightarrow H + Br$								*Sander et al.* [2000]
$HOBr + h\nu \rightarrow Br + OH$								
$BrONO_2 + h\nu \rightarrow Br + NO_3$								
$BrONO_2 + h\nu \rightarrow BrO + NO_2$								
$BrCl + h\nu \rightarrow Br + Cl$								
$CH_3Cl + h\nu \rightarrow CH_3O_2 + Cl$								
$CH_3Br + h\nu \rightarrow Br + CH_3O_2$								
$CFCl_3 + h\nu \rightarrow 3\ Cl$								*Gillotay and Simon* [1989]
$CF_2Cl_2 + h\nu \rightarrow 2\ Cl$								
$CCl_4 + h\nu \rightarrow 4\ Cl$								
$CH_3CCl_3 + h\nu \rightarrow 3\ Cl$								
$CF_3Br + h\nu \rightarrow Br$								*Gillotay and Simon* [1989]
$CF_2ClBr + h\nu \rightarrow Br + Cl$								*Burkholder et al.* [1991]
$CH_3OOH + h\nu \rightarrow CH_2O + HO_2 + OH$								
$CH_2O + h\nu \rightarrow HO_2 + CO + H$								
$CH_2O + h\nu \rightarrow CO + H_2$								
$CH_3O_2NO_2 + h\nu \rightarrow CH_2O + HO_2 + NO_3$								*Atkinson et al.* [1992]
ALD2 + $h\nu \rightarrow CH_3O_2 + HO_2 + CO$								cross sections, *Martinez et al.* [1992]; quantum yield, *Baulch et al.* [1984]
ALD2 + $h\nu \rightarrow CH_4 + CO$								cross sections, *Martinez et al.* [1992]; quantum yield, *Baulch et al.* [1984]
GLYX + $h\nu \rightarrow CH_2O + CO$								*Atkinson et al.* [1992]
RCHO + $h\nu \rightarrow$ ETO2 + HO_2 + CO								cross sections, *Martinez et al.* [1992]; quantum yield, *Atkinson et al.* [1992]
ACET + $h\nu \rightarrow$ MCO3 + CH_3O_2								*Gierczak et al.* [1998]
MGLY + $h\nu \rightarrow$ MCO3 + HO_2 + CO								Cross sections, *Meller et al.* [1991]; quantum yield, *Koch and Moortgat* [1998]
HAC + $h\nu \rightarrow CH_2O$ + 2.0 HO_2 + CO								= *j*(ALD2)
HACN + $h\nu \rightarrow$ MCO3 + CH_2O + HO_2								= j(ACET)
PAN + $h\nu \rightarrow$ MCO3 + NO_2								
PAN + $h\nu \rightarrow CH_3O_2 + NO_3$								
ETP + $h\nu \rightarrow$ ALD2 + OH + HO_2								= *j*(CH_3OOH)

Table A1. (continued)

Photolysis Processes	Arrhenius A	Arrhenius E/R[a]	Troe[b] k_0^{300}	Troe n	Troe k_∞^{300}	Troe m	Unimolecular K_{eq}[c]	Source/Note[d]
RA3P + $h\nu$ → RCHO + OH + HO_2								= $j(CH_3OOH)$
RP + $h\nu$ → ALD2 + OH + HO_2								= $j(CH_3OOH)$
RIP + $h\nu$ → HAC + OH + HO_2								= $j(CH_3OOH)$
VRP + $h\nu$ → RCHO + OH + HO_2								= $j(CH_3OOH)$
MAP + $h\nu$ → CH_2O + OH + HO_2								= $j(CH_3OOH)$
MRP + $h\nu$ → RCHO + OH + HO_2								= $j(CH_3OOH)$
PRN2 + $h\nu$ → OH + HO_2 + RCHO + NO_2								= $j(CH_3OOH)$

[a]Activation energies here follow JPL report practice in listing E/R as negative if the rate constant increases with decreasing temperature.
[b]Formula, $k = \{(k_0(T)[M])/(1 + k_0(T)[M]/k_\infty(T))\} F_c^{\{1+[\log_{10}(k_0(T)[M]/k_\infty(T))]^2\}^{-1}}$, $k_0(T) = k_0^{300}(T/300)^{-n}$, $k_\infty(T) = k_\infty^{300}(T/300)^{-m}$, $F_c = 0.6$.
[c]Rate constant from ratio of reverse reaction rate constant and equilibrium constant, K_{eq}.
[d]Reactions with source unidentified were taken from JPL 97-4 [*DeMore et al.*, 1997] and not updated in JPL 00-003 [*Sander et al.*, 2000].
[e]*Sander et al.* [2000].
[f]*DeMore et al.* [1997].
[g]Formula: $k = 2.3 \times 10^{-13} e^{600/T} + 1.7 \times 10^{-33}[M] e^{1000/T}$.
[h]Formula: $k = (2.3 \times 10^{-13} e^{600/T} + 1.7 \times 10^{-33}[M] e^{1000/T}) \times 1.4 \times 10^{-21} e^{2200/T}$.
[i]Represents a possible homogeneous component for N_2O_5 hydrolysis. The JPL 97-4 recommended upper limit is 2.0e-21, but *Sverdrup et al.* [1987] have reported the upper limit chosen here. More recent work also points to a third-order component.
[j]Formula: $k([M], T) = k_0 + (k_3[M]/(1 + k_3[M]/k_2))$, $k_0 = 2.4 \times 10^{-14} e^{460/T}$, $k_2 = 2.7 \times 10^{-17} e^{2199/T}$, $k_3 = 6.5 \times 10^{-34} e^{1335/T}$.
[k]This reaction combines the major actual product from the reaction above, CH_3, CH_2OH, or HCO, with the fast subsequent reaction with O_2 to form CH_3O_2, $CH_2O + HO_2$, or $HO_2 + CO$. This is done to reduce the number of species and size of a mechanism without compromising its accuracy (an implicit photostationary state assumption).
[l]Note typos or sign errors in E/R in Table 1 of *Paulson and Seinfeld* [1992] for at least Rxns 6–13, 33. *Jacobson* [1995] repeats these errors in his book (and propagates them to the A factors). *Kirchner and Stockwell* [1996] and *Horowitz et al.* [1998] have the correct values.
[m]See *deGouw and Howard* [1997] for negative results.

Table A2. Species Within LLNL-IMPACT Troposphere-Stratosphere Photochemical Mechanism

Symbolic Name	Atomic Composition	Chemical Name
A3O2	$C_3H_7O_2$	n-propyl peroxy radical $CH_3CH_2CH_2OO(.)$
ACET	C_3H_6O	2-propanone acetone $CH_3C(=O)CH_3$
ACO2	CH_2O_2	formic acid HC(=O)OH
AHO2	CH_3O_3	hydroxymethylperoxide radical $HOCH_2OO(.)$
ALD2	C_2H_4O	acetaldehyde ($CH_3C(=O)H$)
ATO2	$C_3H_5O_3$	RO_2 radical from acetone $CH_3C(=O)CH_2OO(.)$
Br	Br	bromine atomic ground state (2P3/2)
BrCl	BrCl	bromine chloride
BrO	BrO	bromine monoxide radical
$BrONO_2$	$BrNO_3$	bromine nitrate
C_2H_6	C_2H_6	ethane CH_3CH_3
C_3H_8	C_3H_8	propane $CH_3CH_2CH_3$
CCl_4	CCl_4	carbon tetrachloride
CF_2Cl_2	CCl_2F_2	CFC12
CF_2ClBr	$CBrClF_2$	Halon 1211
CF_3Br	$CBrF_3$	Halon 1301
$CFCl_3$	CCl_3F	CFC11
CH_3Br	$CBrH_3$	methyl bromide
CH_3CCl_3	$C_2Cl_3H_3$	1,1,1-trichloroethane, methylchloroform
CH_3Cl	$CClH_3$	methyl chloride
$CH_3O_2NO_2$	CH_3O_4N	methylperoxy nitrate
CH_4	CH_4	methane
Cl	Cl	chlorine atomic ground state (2P3/2)
Cl_2	Cl_2	molecular chlorine
Cl_2O_2	Cl_2O_2	chlorine monoxide dimer ClOOCl
ClO	ClO	chlorine monoxide radical
$ClONO_2$	$ClNO_3$	chlorine nitrate
CO	CO	carbon monoxide
ECO3	$C_3H_5O_3$	peroxypropionyl radical $CH_3CH_2C(=O)OO(.)$
ETO2	$C_2H_5O_2$	ethyl peroxy radical $H_3CCH_2OO(.)$
ETP	$C_2H_6O_2$	peroxy ethanol CH_3CH_2OOH
GLYX	$C_2H_2O_2$	glyoxal (HC = O)2
H	H	hydrogen atomic ground state (2S)
H_2	H_2	molecular hydrogen
H_2O	H_2O	water
H_2O_2	H_2O_2	hydrogen peroxide HOOH
HAC	$C_2H_4O_2$	glycolaldehyde, hydroxy-acetaldehyde $HOCH_2C(=O)H$
HACN	$C_3H_6O_2$	hydroxy acetone $HOCH_2C(=O)CH_3$
HACO	$C_2H_3O_4$	1-hydroxy peroxy acetyl radical $HOCH_2C(=O)OO(.)$
HBr	HBr	hydrogen bromide
HCHO	CH_2O	formalydehyde $H_2C = O$
HCl	HCl	hydrogen chloride
HNO_3	HNO_3	nitric acid HONO(O)
HNO_4	HNO_4	pernitric acid HOONO(O)
HO_2	HO_2	perhydroxyl radical HOO
HOBr	HOBr	hydrobromous acid
HOCl	HOCl	hydrochlorous acid
HONO	HNO_2	nitrous acid
INO2	$C_5H_8NO_5$	Isoprene-NO_3 adduct derivative
IPAN	$C_2H_3NO_6$	$HOCH2C(=O)OONO_2$
ISN1	$C_5H_7O_4N$	organic nitrate (ISNIx in Paulson)
ISOP	C_5H_8	2-methyl 1,3-butadiene isoprene $CH_2CHC(CH_3)CH_2$
ISNR	$C_5H_8O_7N$	peroxy radical from OH addition/abstraction from
MACR	C_4H_6O	2-methyl propenal (methacrolein) $CH_2 = C(CH_3)C(=O)H$
MAN2	$C_4H_6O_6N$	MACR/NO_3 adduct $CH_2(OO.)C(CH_3)(ONO_2)C(=O)H$
MAO2	$C_3H_5O_2$	RO_2 radical from MACR $H_2C = C(CH_3)OO(.)$
MAO3	$C_4H_5O_3$	RO_2 radical from MACR $H_2C = C(CH_3)C(=O)OO(.)$
MAP	$C_2H_4O_3$	peroxyacetic acid $CH_3C(=O)OOH$
MCO3	$C_2H_3O_3$	peroxyacetyl radical $CH_3C(=O)OO(.)$
MGLY	$C_3H_4O_2$	methyl glyoxal $CH_3C(=O)C(=O)H$
MO2	CH_3O_2	methylperoxy radical $CH_3OO(.)$
MOH	CH_4O	methyl alcohol CH_3OH
MP	CH_4O_2	methylperoxy alcohol CH_3OOH
MPAN	$C_4H_5NO_5$	$CH_2 = C(CH_3)C(=O)OONO_2$
MRO2	$C_4H_7O_4$	MACR/OH/O_2 adduct $HOCH_2C(CH_3)(OO.)C(=O)H$
MRP	$C_4H_8O_4$	peroxy alcohol from MACR $HOCH_2C(CH_3)(OOH)C(=O)H$
MVK	C_4H_6O	methyl vinyl ketone $CH_3C(=O)CH = CH_2$
N	N	nitrogen atomic ground state (4S)
N_2	N_2	molecular nitrogen
N_2O	N_2O	nitrous oxide NNO
N_2O_5	N_2O_5	dinitrogen pentoxide O_2NONO_2
NO	NO	nitric oxide
NO_2	NO_2	nitrogen dioxide ONO

Table A2. (continued)

Symbolic Name	Atomic Composition	Chemical Name
NO_3	NO_3	nitrogen trioxide ONO(O)
O	O	oxygen atomic ground state (3P)
$O(^1D)$	O	oxygen atomic first singlet state (1D)
O_2	O_2	molecular oxygen
O_3	O_3	ozone
OClO	ClO_2	symmetrical chlorine dioxide
OH	HO	hydroxyl radical
PAN	$C_2H_3NO_5$	peroxyacetyl nitrate $CH_3C(=O)OONO_2$
PPN	$C_3H_5NO_5$	peroxypropionyl nitrate $CH_3CH_2C(=O)OONO_2$
PRN2	$C_4H_7O_6N$	lumped peroxy alcohols from isoprene oxidation
RA3P	$C_3H_8O_2$	peroxy propyl alcohol (primary) $CH_3CH_2CH_2OOH$
RCHO	C_4H_8O	C3-C5 aldehydes
RIO2	$C_5H_9O_3$	isoprene/OH/O_2 adduct
RIP	$C_5H_{10}O_3$	RO_2 isoprene peroxide, CH_2 = CHC(OH)CH_3-CH_2OOH
RP	$C_4H_6O_3$	methacrolein peroxy acid $CH_2 = C(CH_3)C(=O)OOH$
VRO2	$C_4H_7O_4$	MVK/OH/O_2 adduct $CH_3C(=O)CH(OO.)CH_2OH$
VRP	$C_4H_8O_4$	peroxy alcohol from MVK $CH_3C(=O)CH(OOH)$

natural and anthropogenic perturbations on ozone in the tropopause region is important because ozone in this region exerts a disproportionately greater influence on radiative forcing than ozone in other atmospheric regions [*Lacis et al.*, 1990; *IPCC*, 2001].

[102] IMPACT predicts global, three-dimensional species distributions in the troposphere and the stratosphere using a comprehensive chemical mechanism that includes thermal and photolytic reactions. Detailed modules address surface and elevated emissions, dry deposition, wet scavenging from both convective and large-scale clouds, vertical diffusion, convection, and advection. Stiff ordinary differential equation systems representing chemical equations and rates are solved using SMVGEAR II. The model was designed for, and is exercised on, multiple computer platforms such as UNIX workstations, vector supercomputers, and massively parallel computers (including the COMPAQ SC1, IBM SP, and Cray T3E).

[103] In model calculations of ^{222}Rn and ^{210}Pb, IMPACT captures the seasonal distribution and magnitude of surface observations of ^{210}Pb at a number of sites. Differences between model predictions and observations at Mauna Loa result from insufficient transport of Asian outflows during the first half of the year.

[104] A model simulation of a full annual photochemical cycle in the troposphere and stratosphere shows predicted OH and O_3 concentrations agree well with observations. Concentrations of OH vary, as expected, with proximity to large water vapor concentrations and sources of O_3 precursors (such as NO_x, NMHCs, etc.). The IMPACT calculated global methyl chloroform lifetime is 5.3 years, while that calculated using tropospheric OH loss is 6.5 years.

[105] The stratospheric O_3 mixing ratios predicted by IMPACT compare favorably with UARS-HALOE O_3 measurements, although polar winter ozone is too low in IMPACT caused by isolation of the polar region. Ozone levels predicted by the model at 200 mbar and 100 mbar, however, tend to be higher than observed by ozonesondes by 10–25%, and up to a factor of 2 in particular locations, but are usually within observational error bars. Within the troposphere, model-predicted ozone concentrations are higher than observed for some high northern and southern latitude sites primarily due to excessive transport of stratospheric ozone. The model predicted ozone concentration in the tropics agrees quite well with observations there.

[106] The total flux of stratospheric ozone advected through a vertical surface ranges from 663 Tg O_3 yr^{-1} to 806 Tg O_3 yr^{-1}, depending on the definition of tropopause. The net annual in situ photochemical production term (production minus loss) is calculated to be 17–161 Tg O_3 yr^{-1}, with an annual dry deposition amount of 826 Tg O_3 yr^{-1}.

[107] Comparison to in situ aircraft observations of ozone-controlling radicals reveals that ozone and NO_y abundance are simulated reasonably well, as are HO_x catalytic cycles and total production and removal rates for ozone. NO_x is, however, overpredicted in the lower mid latitude stratosphere, possibly as a result of underpredicting processes converting NO_x to NO_y. This could be a result of climatological aerosol surface area densities that are specified at levels below actual values, underpredicted conversion rates, or both.

Appendix A

[108] Here we present the IMPACT photochemical mechanism. Table A1 includes homogeneous gas phase thermal and photolytic reactions, their reactants, products, kinetic parameters, and the literature sources. Table A2 describes all chemical species included in the mechanism. Table A3 includes the heterogeneous thermal reactions, with gas phase reactants and products, which are moderated by the presence of aerosol surfaces.

Table A3. Aerosol Heterogeneous Processes Within the IMPACT Model

Reaction	Location
1. $N_2O_5 \rightarrow 2HNO_3$	stratosphere
2. $ClONO_2 \rightarrow HOCl + HNO_3$	stratosphere
3. $BrONO_2 \rightarrow HOBr + HNO_3$	stratosphere
4. $HCl + ClONO_2 \rightarrow Cl_2 + HNO_3$	stratosphere
5. $HCl + HOCl \rightarrow Cl_2 + H_2O$	stratosphere
6. $HOBr + HCl \rightarrow BrCl + H_2O$	stratosphere
7. $N_2O_5 \rightarrow 2HNO_3$	troposphere
8. $NO_3 \rightarrow HNO_3$	troposphere
9. $NO_2 + H_2O \rightarrow 0.5\ HONO + 0.5\ HNO_3$	troposphere

[109] **Acknowledgments.** We would like to thank the reviewers of this paper for their many helpful suggestions and comments. This work has been supported in part by the Department of Energy Office of Science through the Climate Change Prediction Program (CCPP), Scientific Discovery through Advanced Computing (SciDAC), and Atmospheric Chemistry Program (ACP) programs, as well as by the Lawrence Livermore National Laboratory internal LDRD program. This work was performed under the auspices of the U.S. Department of Energy by the University of California, Lawrence Livermore National Laboratory, under contract W-7405-ENG-48.

References

Andreae, M. O. (1990), Biomass Burning: Its history, use and distribution and its impact on environmental quality and global climate, in *Global Biomass Burning*, pp. 3–21, edited by J. S. Levine, MIT Press, Cambridge, Mass.

Appenzeller, C., and H. C. Davies (1992), Structure of stratospheric intrusions into the troposphere, *Nature*, *358*, 570–572.

Appenzeller, C., H. C. Davies, and W. A. Norton (1996), Fragmentation of stratospheric intrusions, *J. Geophys. Res.*, *101*, 1435–1456.

Atherton, C. S. (1994), Predicting tropospheric ozone and hydroxyl radical in a global, three-dimensional, chemistry, transport, and deposition model, Ph.D. thesis, Univ. of Calif., Davis, Davis, California.

Atherton, C. S. (1995), Biomass burning sources of nitrogen oxides, carbon monoxide, and non-methane hydrocarbons, *LLNL Rep. UCRL-ID-122583*, Lawrence Livermore Natl. Lab., Livermore, Calif.

Atkinson, R., D. L. Baulch, R. A. Cox, R. F. Hampson Jr., J. A. Kerr, and J. Troe (1992), Evaluated kinetic and photochemical data for atmospheric chemistry: Supplement IV, IUPAC Subcommittee on Gas Kinetic Data Evaluation for Atmospheric Chemistry, *J. Phys. Chem. Ref. Data*, *21*, 1125–1568.

Atkinson, R., D. L. Baulch, R. A. Cox, R. F. Hampson Jr., J. A. Kerr, M. J. Rossi, and J. Troe (1997), Evaluated kinetic, photochemical and heterogeneous data for atmospheric chemistry: Supplement V, IUPAC Subcommittee on Gas Kinetic Data Evaluation for Atmospheric Chemistry, *J. Phys. Chem. Ref. Data*, *26*, 521–1011.

Balkanski, Y. J., D. J. Jacob, G. M. Gardner, W. C. Graustein, and K. K. Turekian (1993), Transport and residence times of tropospheric aerosols inferred from a global three-dimensional simulation of ^{210}Pb, *J. Geophys. Res.*, *98*, 20,573–20,586.

Bamber, D. J., P. G. W. Healey, B. M. R. Jones, S. A. Penkett, A. F. Tuck, and G. Vaughan (1984), Vertical profiles of tropospheric gases: Chemical consequences of stratospheric intrusions, *Atmos. Environ.*, *18*, 1759–1766.

Barrie, L. A., J. W. Bottenheim, R. C. Schnell, P. J. Crutzen, and R. A. Rasmussen (1988), Ozone destruction and photochemical reactions at polar sunrise in the lower Arctic atmosphere, *Nature*, *334*, 138–141.

Barrie, L. A., et al. (2002), A comparison of large-scale atmospheric sulphate aerosol models (COSAM): Overview and highlights, *Tellus, Ser. B*, *53*, 615–645.

Bates, T. S., K. C. Kelly, J. E. Johnson, and R. H. Gammon (1995), Regional and seasonal variations in the flux of oceanic carbon monoxide to the atmosphere, *J. Geophys. Res.*, *100*, 23,093–23,101.

Baughcum, S. L., T. G. Tritz, S. C. Hernerdon, and D. C. Pickett (1996), Scheduled civil aircraft emission inventories for 1992: Database development and analysis, *NASA CR-4700*, Natl. Aeronautics and Space Admin., Washington, D. C.

Baulch, D. L., R. A. Cox, R. F. Hampson Jr., J. A. Kerr, J. Troe, and R. T. Watson (1984), Evaluated kinetic and photochemical data for atmospheric chemistry: Supplement II, CODATA Task Group on Gas Phase Chemical Kinetics, *J. Phys. Chem. Ref. Data*, *13*, 1259–1380.

Baulch, D. L., C. J. Cobos, R. A. Cox, C. Esser, P. Frank, T. H. Just, J. A. Kerr, M. J. Pilling, J. Troe, R. W. Walker, and J. Warnatz (1992), Evaluated kinetic data for combustion modeling, *J. Phys. Chem. Ref. Data*, *21*, 411–429.

Benkovitz, C. M., M. T. Scholtz, J. Pacyna, L. Tarrason, J. Dignon, E. C. Voldner, P. A. Spiro, J. A. Logan, and T. E. Graedel (1996), Global gridded inventories of anthropogenic emissions of sulfur and nitrogen, *J Geophys. Res.*, *101*, 29,239–29,253.

Berntsen, T., I. S. A. Isaksen, W.-C. Wang, and X. Z. Liang (1996), Impacts of increased anthropogenic emissions in Asia on tropospheric ozone and climate -A global, 3-D model study, *Tellus, Ser. B*, *48*, 13–32.

Bey, I., D. J. Jacob, R. M. Yantosca, J. A. Logan, B. D. Field, A. M. Fiore, Q. Li, H. Y. Liu, L. J. Mickley, and M. G. Schultz (2001), Global modeling of tropospheric chemistry with assimilated meteorology: Model description and evaluation, *J. Geophys. Res.*, *106*, 23,073–23,095.

Bouwman, A. F., K. W. van der Hoek, and J. G. J. Olivier (1995), Uncertainty in the global source distribution of nitrous oxide, *J. Geophys. Res.*, *100*, 2785–2800.

Brasseur, G. P., X. X. Tie, P. J. Rasch, and F. Lefevre (1997), A three-dimensional simulation of the Antarctic ozone hole: Impact of anthropogenic chlorine on the lower stratosphere and upper troposphere, *J. Geophys. Res.*, *102*, 8909–8930.

Brasseur, G. B., D. A. Hauglustaine, S. Walters, P. J. Rasch, J.-F. Muller, C. Granier, and X. X. Tie (1998), MOZART, a global chemical transport model for ozone and related chemical tracers: 1. Model description, *J. Geophys. Res.*, *103*, 28,265–28,289.

Bruhl, C., S. R. Drayson, J. M. Russell III, P. J. Crutzen, J. M. McInerney, P. N. Purcell, H. Claude, H. Gernandt, T. J. McGee, I. S. McDermid, and M. R. Gunson (1996), Halogen Occulation Experiment (HALOE) ozone channel validation, *J. Geophys. Res.*, *101*, 10,217–10,240.

Burkholder, J. B., R. R. Wilson, T. Gierczak, R. Talukdar, S. A. McKeen, J. J. Orlando, G. L. Vaghjiani, and A. R. Ravishankara (1991), Atmospheric Fate of CF_3Br, CF_2Br_2, CF_2ClBr, and CF_2BrCF_2Br, *J. Geophys. Res.*, *96*, 5025–5043.

Chew, A. A., R. Atkinson, and S. M. Aschmann (1998), Kinetics of the gas-phase reactions of NO_3 radicals with a series of alcohols, glycol ethers, ethers and chloroalkenes, *J. Chem. Soc. Faraday Trans.*, *94*, 1083–1089.

Chipperfield, M. P., D. Cariolle, P. Simon, R. Ramaroson, and D. J. Lary (1993), A three-dimensional modeling study of trace species in the Arctic lower stratosphere during winter 1989–1990, *J. Geophys. Res.*, *98*, 7199–7218.

Chipperfield, M. P., D. Cariolle, and P. Simon (1994), A three-dimensional transport model study of chlorine activation during EASOE, *Geophys. Res. Lett.*, *21*, 1467–1470.

Chipperfield, M. P., J. A. Pyle, C. E. Blom, N. Glatthor, M. Hopfner, T. Gulde, C. Piesch, and P. Simon (1995), The variability of $ClONO_2$ and HNO_3 in the Arctic polar vortex: Comparison of Transall Michelson interferometer for passive atmospheric sounding measurements and three dimensional model results, *J. Geophys. Res.*, *100*, 9115–9129.

Chuang, C. C., J. E. Penner, K. E. Taylor, A. S. Grossman, and J. J. Walton (1997), An assessment of the radiative effects of anthropogenic sulfate, *J. Geophys. Res.*, *102*, 3761–3778.

Chung, Y. S., and T. Dann (1985), Observations of stratospheric ozone at the ground level in Regina, Canada, *Atmos. Environ.*, *19*, 157–162.

Conrad, R., and W. Seiler (1986), Exchange of CO and H_2 between Ocean and Atmosphere, in *The Role of Air-Sea Exchange in Geochemical Cycling*, edited by P. Buat-Menard, pp. 269–282, D. Reidel, Norwell, Mass.

Coy, L., and R. Swinbank (1997), Characteristics of stratospheric winds and temperatures produced by data assimilation, *J. Geophys. Res.*, *102*, 25,763–25,781.

Coy, L., E. R. Nash, and P. A. Newman (1997), Meteorology of the polar vortex: Spring 1997, *Geophys. Res. Lett.*, *24*, 2693–2696.

Crutzen, P. J., and P. H. Zimmerman (1991), The changing photochemistry of the troposphere, *Tellus*, *43*, 136–151.

Crutzen, P. J., M. G. Lawrence, and U. Poschol (1999), On the background photochemistry of tropospheric ozone, *Tellus, Ser. A*, *51*, 123–146.

Danielsen, E. F. (1968), Stratospheric-tropospheric exchange based on radioactivity, ozone and potential vorticity, *J. Atmos. Sci.*, *25*, 502–518.

D'Anna, B., and C. J. Nielsen (1997), Kinetic study of the vapour-phase reaction between aliphatic aldehydes and the nitrate radical, *J. Chem. Soc. Faraday Trans.*, *93*, 3479–3483.

de Gouw, J. A., and C. J. Howard (1997), Direct measurement of the rate coefficient for the $CH_2 = C(CH_3)C(O)O_2 + NO$ reaction using chemical ionization mass spectrometry, *J. Phys. Chem. A.*, *101*, 8662–8667.

DeMore, W. B., S. P. Sander, D. M. Golden, R. F. Hampson, M. J. Kurylo, C. J. Howard, A. R. Ravishankara, C. E. Kolb, and M. J. Molina (1997), Chemical kinetics and photochemical data for use in stratospheric modeling, *JPL Publ.*, *97-4*.

Dignon, J., J. E. Penner, C. S. Atherton, and J. J. Walton (1992), Atmospheric reactive nitrogen: A model study of natural and anthropogenic sources and the role of microbial soil emissions, *LLNL Rep. UCRL-JC-107393*, Lawrence Livermore Natl. Lab., Livermore, Calif.

Dignon, J., C. S. Atherton, H. E. Eddleman, J. E. Penner, J. J. Walton, and A. S. Grossmann (1998), Quantifying magnitudes and distributions of CO sources, *LLNL Rep. UCRL-JC-128835*, Lawrence Livermore Natl. Lab., Livermore, Calif.

Dlugokencky, E. J., and C. J. Howard (1989), Studies of NO_3 radical reactions with some atmospheric organic compounds at low pressures, *J. Phys. Chem.*, *93*, 1091–1096.

Douglass, A., R. B. Rood, S. R. Kawa, and D. J. Allen (1997), A three-dimensional simulation of the evolution of the middle latitude winter ozone in the middle stratosphere, *J. Geophys. Res.*, *102*, 19,217–19,232.

Eberhard, J., and C. J. Howard (1996), Temperature-dependent kinetics studies of the reactions of $C_2H_5O_2$ and n-$C_3H_7O_2$ radicals with NO, *Int. J. Chem. Kinet.*, *28*, 731–740.

Emmons, L. K., D. A. Hauglustaine, J.-F. Muller, M. A. Carroll, G. P. Brasseur, D. Brunner, J. Staehelin, V. Thouret, and A. Marenco (2000),

Data composites of airborne observations of tropospheric ozone and its precursors, *J. Geophys. Res.*, *105*, 20,497–20,538.
Environmental Measurements Laboratory (2003), High Altitude Sampling Program Database, http://www.eml.doe.gov/, Dept. of Energy, New York.
Erickson, D. J., and J. A. Taylor (1992), Three-dimensional tropospheric CO modeling: The possible influence of the ocean, *Geophys. Res. Lett.*, *19*, 1955–1958.
Feichter, J., R. A. Brost, and M. Heimann (1991), Three-dimensional modeling of the concentration and deposition of 210 Pb aerosols, *J. Geophys. Res.*, *96*, 22,447–22,460.
Foster, K. L., R. A. Plastridge, J. W. Bottenheim, P. B. Shepson, B. J. Finlayson-Pitts, and C. W. Spicer (2001), The role of Br_2 and BrCl in surface ozone destruction at polar sunrise, *Science*, *291*, 471–474.
Fung, I., J. John, J. Lerner, E. Matthews, M. Prather, L. P. Steele, and P. J. Fraser (1991), Three-dimensional model synthesis of the global methane cycle, *J. Geophys. Res.*, *96*, 13,033–13,065.
Giannakopoulos, C., M. P. Chipperfield, K. S. Law, and J. A. Pyle (1999), Validation and intercomparison of wet and dry deposition schemes using ^{210}Pb in a global three-dimensional off-line chemical transport model, *J. Geophys. Res.*, *104*, 23,761–23,784.
Gierczak, T., J. B. Burkholder, R. K. Talukdar, A. Mellouki, S. B. Barone, and A. R. Ravishankara (1997), Atmospheric fate of methyl vinyl ketone and methacrolein, *J. Photochem. Photobiol. A*, *110*, 1–10.
Gierczak, T., J. B. Burkholder, S. Bauerle, and A. R. Ravishankara (1998), Photochemistry of acetone under tropospheric conditions, *Chem. Phys.*, *231*, 229–244.
Gillotay, D., and P. C. Simon (1989), Ultraviolet-absorption spectrum of trifluoro-bromo-methane, difluoro-dibromo-methane and difluoro-bromo-chloro-methane in the vapor-phase, *J. Atmos. Chem.*, *8*, 41–62.
Giorgi, F., and W. L. Chameides (1986), Rainout lifetimes of highly soluble aerosols and gases as inferred from simulations with a general circulation model, *J. Geophys. Res.*, *91*, 14,367–14,376.
Goldfarb, L., M. H. Harwood, J. B. Burkholder, and A. R. Ravishankara (1998), Reaction of $O(^3P)$ with $ClONO_2$: Rate coefficients and yield of NO_3 product, *J. Phys. Chem. A*, *102*, 8556–8563.
Grosjean, E., and D. Grosjean (1996), Rate constants for the gas-phase reaction of ozone with 1, 1-disubstituted alkenes, *Int. J. Chem. Kinet.*, *28*, 911–918.
Guelle, W., Y. J. Balkanski, J. E. Dibb, M. Schulz, and F. Dulac (1998), Wet deposition in a global size-dependent aerosol transport model: 2. Influence of the scavenging scheme on ^{210}Pb vertical profiles, surface concentrations, and deposition, *J. Geophys. Res.*, *103*, 28,876–28,891.
Guenther, A., C. N. Hewitt, D. Erickson, R. Fall, C. Gergon, T. Graedel, P. Harley, L. Klinger, M. Lerdau, W. A. McKay, T. Piercet, B. Scholes, R. Steinbrecher, R. Tallamraju, J. Taylor, and P. Zimmerman (1995), A global model of natural volatile organic compound emissions, *J. Geophys. Res.*, *100*, 8873–8892.
Harries, J. E., J. M. Russell III, A. F. Tuck, L. L. Gordley, P. Purcell, K. Stone, R. M. Bevilacqua, M. R. Gunson, G. Nedoluha, and W. A. Weintraub (1996), Validation of measurements of water vapor from the Halogen Occultation Experiment (HALOE), *J. Geophys. Res.*, *101*, 10,205–10,216.
Hauglustaine, D. A., G. P. Brasseur, S. Walters, P. J. Rasch, J.-F. Muller, L. K. Emmons, and M. A. Carroll (1998), MOZART, a global chemical transport model for ozone and related chemical tracers: 1. Model results and evaluation, *J. Geophys. Res.*, *103*, 28,291–28,335.
Heimann, M., and C. Keeling (1989), A three-dimensional model of atmospheric CO_2 transport based on observed winds: 2. Model description and simulated tracer experiments, *Geophys. Monogr.*, *55*, 237–275.
Hoell, J. M., D. D. Davis, S. C. Liu, R. E. Newell, H. Akimoto, R. J. McNeal, and R. J. Bendura (1997), The Pacific Exploratory Mission-West Phase B: February–March, 1994, *J. Geophys. Res.*, *102*, 28,223–28,240.
Holton, J. R., P. H. Haynes, M. E. McIntyre, A. R. Douglass, R. B. Rood, and L. Pfister (1995), Stratosphere-troposphere exchange, *Rev. Geophys*, *33*, 403–439.
Horowitz, L. W., J. Liang, G. M. Gardner, and D. J. Jacob (1998), Export of reactive nitrogen from North America during summertime: Sensitivity to hydrocarbon chemistry, *J. Geophys. Res.*, *103*, 13,451–13,476.
Houweling, S., F. Dentener, and J. Lelieveld (1998), The impact of nonmethane hydrocarbon compounds on tropospheric photochemistry, *J. Geophys. Res.*, *103*, 10,673–10,696.
Intergovernmental Panel on Climate Change (IPCC) (2001), *Climate Change 2001: The Scientific Basis,Contribution of Working Group I to the Third Assessment Report of the Intergovernmental Panel on Climate Change*, edited by J. T. Houghton et al., 881 pp., Cambridge Univ. Press, New York.
Jacob, D. J. (2000), Heterogeneous chemistry and tropospheric ozone, *Atmos. Environ.*, *34*, 2131–2159.
Jacob, D. J., and S. C. Wofsy (1988), Photochemistry of biogenic emissions over the Amazon Forest, *J. Geophys. Res.*, *93*, 1477–1486.
Jacob, D. J., and S. C. Wofsy (1990), Budgets of reactive nitrogen, hydrocarbons, and ozone over the Amazon forest during the wet season, *J. Geophys. Res.*, *95*, 16,737–16,754.
Jacob, D. J., S.-M. Fan, S. C. Wofsy, P. A. Spiro, P. S. Bakwin, J. A. Ritter, E. V. Browell, G. L. Gregory, D. R. Fitzjarrald, and K. E. Moore (1992), Deposition of ozone to tundra, *J. Geophys. Res.*, *97*, 16,473–16,479.
Jacob, D. J., et al. (1997), Evaluation and intercomparison of global atmospheric transport models using ^{222}Rn and other short-lived tracers, *J. Geophys. Res.*, *102*, 5953–5970.
Jacobson, M. A. (1995), Computation of global photochemistry with SMVGEAR II, *Atmos. Environ., Part A*, *29*, 2541–2546.
Jöckel, P., R. V. Kuhlmann, M. G. Lawrence, B. Steil, C. A. M. Brenninkmeijer, P. J. Crutzen, P. J. Rasch, and B. Eaton (2001), On a fundamental problem in implementing flux-form advection schemes for tracer transport in three-dimensional general circulation and chemical tracer models, *Q. J. R. Meteorol. Soc.*, *127*, 1035–1052.
Kanakidou, M., and P. J. Crutzen (1993), Scale problems in global tropospheric chemistry modeling: Comparison of results obtained with a three-dimensional model, adopting longitudinally uniform and varying emissions of Nox and NMHC, *Chemosphere*, *26*, 787–801.
Khalil, M. A. K. (1999), Atmospheric carbon monoxide, *Chemosphere*, *1*, ix–xi.
Kiehl, J. T., J. J. Hack, G. B. Bonan, B. A. Boville, D. L. Williamson, and P. J. Rasch (1998), The National Center for Atmospheric Research Community Climate Model: CCM3, *J. Clim.*, *11*, 1131–1149.
Kirchner, F., and W. R. Stockwell (1996), The effect of peroxy radical reactions on the predicted concentrations of ozone, nitrogenous compounds and radicals, *J. Geophys. Res.*, *101*, 21,007–21,022.
Koch, G., and G. K. Moortgat (1998), Photochemistry of methylglyoxal in the vapor phase, *J. Phys. Chem.*, *102*, 9142–9153.
Komhyr, W. D., S. J. Oltmans, J. A. Lathrop, J. B. Kerr, and W. A. Matthews (1994), The latitudinal distribution of ozone to 35 km altitude from ECC ozonesonde observations, 1982–1990, *Proceedings of Quadrennial Ozone Symposium 1992: Ozone in the Troposphere and Stratosphere*, edited by R. D. Hudson, *NASA Conf. Publ.*, *3266*, 858–862.
Kritz, M. A., S. W. Rosner, and D. Z. Stockwell (1998), Validation of an off-line three-dimensional chemical transport model using observed radon profiles: 1. Observations, *J. Geophys. Res.*, *103*, 8425–8432.
Lacis, A. A., D. J. Wuebbles, and J. Logan (1990), Radiative forcing of climate by changes in the vertical distribution of ozone, *J. Geophys. Res.*, *95*, 9971–9981.
Langford, A. O. (1999), Stratosphere-troposphere exchange at the subtropical jet: Contribution to the tropospheric ozone budget at midlatitudes, *Geophys. Res. Lett.*, *26*, 2449–2452.
Langford, A. O., and S. J. Reid (1998), Dissipation and mixing of a small-scale stratospheric intrusion in the upper troposphere, *J. Geophys. Res.*, *103*, 31,265–31,276.
Larsen, R. J., C. G. Sanderson, and J. Kada (1995), EML Surface air sampling program, 1990–1993 data, *Rep. EML-572*, Environ. Meas. Lab., New York.
Larson, R. E. (1974), Radon profiles over Kilauea, the Hawaiian Islands and Yukon Valley snow cover, *Pure Appl. Geophys.*, *112*, 204–208.
Lawrence, M. G., P. J. Crutzen, P. J. Rasch, B. E. Eaton, and N. M. Mahowald (1999), A model for studies of tropospheric photochemistry: Description, global distributions, and evaluation, *J. Geophys. Res.*, *104*, 26,245–26,277.
Lelieveld, J., and F. J. Dentener (2000), What controls tropospheric ozone?, *J. Geophys. Res.*, *105*, 3531–3551.
Lerner, J., E. Matthews, and I. Fung (1988), Methane emission from animals: A global high-resolution database, *Global Biogeochem. Cycles*, *2*, 139–156.
Levy, H., J. D. Mahlman, and W. J. Moxim (1985), Tropospheric ozone: The role of transport, *J. Geophys. Res.*, *90*, 3753–3772.
Levy, H., P. S. Kasibhatla, W. J. Moxim, A. A. Klonecki, A. I. Hirsch, S. J. Oltmans, and W. L. Chameides (1997), The global impact of human activity on tropospheric ozone, *Geophys. Res. Lett.*, *24*, 791–794.
Lin, S. J., and R. B. Rood (1996), A fast flux form semi-Lagrangian transport scheme on the sphere, *Mon. Weather Rev.*, *124*, 2046–2070.
Liousse, C., J. E. Penner, C. Chuang, J. J. Walton, H. Eddleman, and H. Cachier (1996), A global three-dimensional model study of carbonaceous aerosols, *J. Geophys. Res.*, *101*, 19,411–19,432.
Liu, H., D. J. Jacob, I. Bey, and R. M. Yantosca (2001), Constraints from ^{210}Pb and ^{7}Be on wet deposition and transport in a global three-dimensional chemical tracer model driven by assimilated meteorological fields, *J. Geophys. Res.*, *106*, 12,109–12,128.
Logan, J. A. (1999a), An analysis of ozonesonde data for the lower stratosphere: Recommendations for testing models, *J. Geophys. Res.*, *104*, 16,151–16,170.

Logan, J. A. (1999b), An analysis of ozonesonde data for the troposphere: Recommendations for testing 3-D models, and development of a gridded climatology for tropospheric ozone, *J. Geophys. Res.*, *104*, 16,115–16,149.

Loring, R. O., H. E. Fuelberg, J. Fishman, M. V. Watson, and E. V. Browell (1996), Influence of a middle-latitude cyclone on tropospheric ozone distributions during a period of TRACE A, *J. Geophys. Res.*, *101*, 23,941–23,956.

Lurmann, F. W., A. C. Lloyd, and R. Atkinson (1986), A chemical mechanism for use in long-range transport/acid deposition computer modeling, *J. Geophys. Res.*, *91*, 10,905–10,936.

Mari, C., D. J. Jacob, and P. Bechtold (2000), Transport and scavenging of soluble gases in a deep convective cloud, *J. Geophys. Res.*, *105*, 22,255–22,267.

Martinez, R. D., A. A. Buitrago, N. W. Howell, C. H. Hearn, and J. A. Joens (1992), The near UV absorption of several aliphatic aldehydes and ketones at 300 K, *Atmos. Environ., Part A*, *26*, 785–792.

Matthews, E. (1983), Global vegetation and land use: New high-resolution data bases for climate studies, *J. Clim. Appl. Meteorol.*, *22*, 474–487.

McCulloch, A. P. Midgley, and D. Fisher (1994), Distribution of emissions of chlorofluorocarbons (CFCs) 11, 12, 113, 114, and 115 among reporting and non-reporting countries in 1986, *Atmos. Environ.*, *28*, 2567–2582.

Meller, R., W. Raber, J. N. Crowley, M. E. Jenkin, and G. K. Moortgat (1991), The UV-visible absorption spectrum of methylglyoxal, *J. Photochem. Photobiol. A*, *62*, 163–171.

Merrill, J. T., and J. L. Moody (1996), Synoptic meteorology and transport during the North Atlantic Regional Experiment (NARE) intensive: Overview, *J. Geophys. Res.*, *101*, 28,903–28,922.

Metwally, M. (1995), Jet Aircraft engine emissions database development: 1992 military, charter and nonscheduled traffic, *NASA CR-4684*, Natl. Aeronaut. and Space Admin., Washington, D. C.

Minschwaner, K., G. P. Anderson, L. A. Hall, and K. Yoshino (1992), Polynomial coefficients for calculating O_2 Schumann-Runge cross-sections at 0.5 cm-1 resolution, *J. Geophys. Res.*, *97*, 10,103–10,108.

Mirin, A. A., et al. (1994), Climate system modeling using a domain and task decomposition message-passing approach, *Comput. Phys. Commun.*, *84*, 278.

Montzka, S. A., C. M. Spivakovsky, J. H. Butler, J. W. Elkins, L. T. Lock, and D. J. Mondeel (2000), New observational constraints for atmospheric hydroxyl on global and hemispheric scales, *Science*, *288*, 500–503.

Moody, J. L., J. C. Davenport, J. T. Merrill, S. J. Oltmans, D. D. Parrish, J. S. Holloway, H. Levy II, G. L. Forbes, M. Trainer, and M. Buhr (1996), Meteorological mechanisms for transporting O_3 over the western North Atlantic Ocean: A case study for August 24–29, 1993, *J. Geophys. Res.*, *101*, 29,213–29,228.

Müller, J.-F., and G. P. Brasseur (1995), IMAGES: A three-dimensional chemical transport model of the global troposphere, *J. Geophys. Res.*, *100*, 16,445–16,490.

Murphy, D. M., and D. W. Fahey (1994), An estimate of the flux of stratospheric reactive nitrogen and ozone into the troposphere, *J. Geophys. Res.*, *99*, 5325–5332.

Neuman, J. A., et al. (2001), In situ measurements of HNO_3, NO_y, NO, and O_3 in the lower stratosphere and upper troposphere, *Atmos. Environ.*, *35*, 5789–5797.

Niki, H., P. D. Maker, C. M. Savage, and M. D. Hurley (1987), Fourier transform infrared study of the kinetics and mechanisms for the Cl-atom- and HO-radical-initiated oxidation of glycolaldehyde, *J. Phys. Chem.*, *91*, 2174–2178.

Olivier, J. G. J., A. F. Bouwman, C. W. M. Van der Maas, J. J. M. Berdowski, C. Veldt, J. P. J. Bloos, A. J. H. Visschedijk, P. Y. F. Zandveld, and J. L. Haverlag (1996), Description of EDGAR Version 2.0: A set of global emission inventories of greenhouse gases and ozone-depleting substances for all anthropogenic and most natural sources on a per country basis and on $1^\circ \times 1^\circ$ grid, *RIVM/TNO Rep. 771060-002*, Natl. Inst. of Public Health and the Environ., Bilthoven, Netherlands, December .

Olsen, S. C., C. A. McLinden, and M. J. Prather (2001), Stratospheric N_2O-NO_y system: Testing uncertainties in a three-dimensional framework, *J. Geophys. Res.*, *106*, 28,771–28,784.

Oltmans, S. J., and H. Levy (1994), Surface ozone measurements from a global network, *Atmos. Environ.*, *28*, 9–24.

Pacyna, J. M., and T. E. Graedel (1995), Atmospheric emissions inventories: Status and prospects, *Annu. Rev. Energy Environ.*, *20*, 265–300.

Park, J. H., M. K. W. Ko, C. H. Jackman, R. A. Plumb, J. A. Kaye, and K. H. Sage (Eds.) (1999), Models and measurements intercomparison II, *NASA/TM-1999-209554*, Natl. Aeronaut. and Space Admin., Washington, D. C.

Paulson, S. E., and J. H. Seinfeld (1992), Development and evaluation of a photooxidation mechanism for isoprene, *J. Geophys. Res.*, *97*, 20,703–20,715.

Penner, J. E., C. S. Atherton, J. Dignon, S. J. Ghan, J. J. Walton, and S. Hameed (1991), Tropospheric nitrogen: A three-dimensional study of sources, distributions, and deposition, *J. Geophys. Res.*, *96*, 959–990.

Pickering, K. E., Y. S. Wang, W. K. Tao, C. Price, and J. F. Müller (1998), Vertical distributions of lightning NO_x for use in regional and global chemical transport models, *J. Geophys. Res.*, *103*, 31,203–31,216.

Prather, M., M. McElroy, S. Wofsy, G. Russell, and D. Rind (1987), Chemistry of the global troposphere: Fluorocarbons as tracers of air motion, *J. Geophys. Res.*, *92*, 6579–6613.

Price, C., and D. Rind (1992), A simple lightning parameterization for calculating global lightning distribution, *J. Geophys. Res.*, *97*, 9919–9933.

Prinn, R. G., et al. (2001), Evidence for substantial variations of atmospheric hydroxyl radical in the past two decades, *Science*, *292*, 1882–1888.

Randel, W. J., F. Wu, J. M. Russell III, A. Roche, and J. W. Water (1998), Seasonal cycles and QBO variations in stratospheric CH_4 and H_2O observed in UARS HALOE data, *J. Atmos. Sci.*, *55*, 163–185.

Rasch, P. J., N. M. Mahowald, and B. E. Eaton (1997), Representation of transport, convection, and the hydrological cycle in chemical transport models: Implication for the modeling of short-lived and soluble species, *J. Geophys. Res.*, *102*, 28,127–28,138.

Rind, D., and J. Lerner (1996), Use of on-line tracers as a diagnostic tool in general circulation model development: 1. Horizontal and vertical transport in the troposphere, *J. Geophys. Res.*, *101*, 12,667–12,683.

Roelofs, G.-J., and J. Lelieveld (1995), Distribution and budget of O_3 in the troposphere calculated with a chemistry general circulation model, *J. Geophys. Res.*, *100*, 20,983–20,998.

Roelofs, G.-J., and J. Lelieveld (1997), Model study of the influence of cross-tropopause O_3 transport on tropospheric O_3 levels, *Tellus, Ser. B*, *49*, 38–55.

Roelofs, G.-J., and J. Lelieveld (2000), Tropospheric ozone simulation with a chemistry-general circulation model: Influence of higher hydrocarbon chemistry, *J. Geophys. Res.*, *105*, 22,697–22,712.

Rose, K., and G. P. Brasseur (1989), A three-dimensional model of chemically active trace species in the middle atmosphere during disturbed winter conditions, *J. Geophys. Res.*, *94*, 16,387–16,403.

Rotman, D. A., et al. (2001), Global Modeling Initiative assessment model: Model description, integration, and testing of the transport shell, *J. Geophys. Res.*, *106*, 1669–1691.

Sander, S. P., et al. (2000), Chemical kinetics and photochemical data for use in stratospheric modeling: Supplement to Evaluation 12: Update of key reactions, Evaluation 13, *JPL Publ.*, *00-003*.

Sehested, J., L. K. Christensen, O. J. Nielsen, M. Bilde, T. J. Wallington, W. F. Schneider, J. J. Orlando, and G. S. Tyndall (1998), Atmospheric chemistry of acetone: Kinetic study of the $CH_3C(O)CH_2O_2$ + NO/NO_2 reactions and decomposition of $CH_3C(O)CH_2O_2NO_2$, *Int. J. Chem. Kinet.*, *30*, 475–489.

Seinfeld, J. H., and S. N. Pandis (1998), *Atmospheric Chemistry and Physics*, John Wiley, New York.

Singh, H. B., D. O'Hara, D. Herlth, G. W. Sachse, D. R. Blake, J. D. Bradshaw, M. Kanakidou, and P. J. Crutzen (1994), Acetone in the atmosphere: Distribution, sources, and sinks, *J. Geophys. Res.*, *99*, 1805–1819.

Stevenson, D. S., C. E. Johnson, W. J. Collins, R. G. Derwent, and J. M. Edwards (2000), Future estimates of tropospheric ozone radiative forcing and methane turnover: The impact of climate change, *Geophys. Res. Lett.*, *27*, 2073–2076.

Stockwell, D. Z., M. A. Kritz, M. P. Chipperfield, and J. A. Pyle (1998), Validation of an off-line three-dimensional chemical transport model using observed radon profiles: 2. Model results, *J. Geophys. Res.*, *103*, 8433–8445.

Sverdrup, G. M., C. W. Spicer, and G. F. Ward (1987), Investigation of the gas-phase reaction of dinitrogen pentoxide with water-vapor, *Int. J. Chem. Kinet.*, *19*, 191–205.

Thomason, L. W., L. R. Polle, and T. Deshler (1997), A global climatology of stratospheric aerosol surface area density deduced from Stratospheric Aerosol and Gas Experiment II measurements: 1984–1994, *J. Geophys. Res.*, *102*, 8967–8976.

Treacy, J., M. El Hag, D. O'Farrell, and H. Sidebottom (1992), Reactions of ozone with unsaturated organic compounds, *Ber. Bunsenges. Phys. Chem.*, *96*, 422–427.

Walton, J. J., M. C. MacCracken, and S. J. Ghan (1988), A global-scale Lagrangian trace species model of transport, transformation, and removal processes, *J. Geophys. Res.*, *93*, 8339–8354.

Wang, Y., D. J. Jacob, and J. A. Logan (1998a), Global simulation of tropospheric O_3-NO_x-hydrocarbon chemistry: 1. Model formulation, *J. Geophys. Res.*, *103*, 10,713–10,725.

Wang, Y., D. J. Jacob, and J. A. Logan (1998b), Global simulation of tropospheric O_3-NO_x-hydrocarbon chemistry: 3. Origin of tropospheric ozone and effects of nonmethane hydrocarbons, *J. Geophys. Res.*, *103*, 10,757–10,767.

Watson, J. J., J. A. Probert, and S. D. Piccot (1991), Global inventory of volatile organic compound emissions from anthropogenic sources, *EPA-600/8-91-002*, U. S. Environ. Prot. Agency, Research Triangle Park, N. C.

Wauben, W. M. F., J. P. F. Fortuin, P. F. J. vanVelthoven, and H. M. Kelder (1998), Comparison of modeled ozone distributions with sonde and satellite observations, *J. Geophys. Res.*, *103*, 3511–3530.

Wennberg, P. O., et al. (1994), Removal of stratospheric O_3 by radicals: In situ measurements of OH, HO_2, NO, NO_2, ClO, and BrO, *Science*, *266*, 398–404.

Wesely, M. L. (1989), Improved parameterizations for surface resistance to gaseous dry deposition in regional-scale numerical models, *Atmos. Environ.*, *23*, 1293–1304.

Wesely, M. L., D. R. Book, R. L. Hart, and R. E. Speer (1985), Measurements and parameterization of particulate sulfur dry deposition over grass, *J. Geophys. Res.*, *90*, 2131–2143.

Wild, O., and M. J. Prather (2000), Excitation of the primary tropospheric chemical mode in a global three-dimensional model, *J. Geophys. Res.*, *105*, 24,647–24,660.

Willmott, C. J., C. M. Rowe, and Y. Mintz (1985), Climatology of the terrestrial seasonal water cycle, *J. Clim.*, *5*, 589–606.

World Meteorological Organization (WMO) (1999), Scientific Assessment of Ozone Depletion: 1998, *Rep. 44*, Global Ozone Res. and Monit. Project, Geneva.

World Meteorological Organization (WMO) (2002), Scientific Assessment of Ozone Depletion: 2002, Global Ozone Research and Monitoring Project, *Rep. 47*, Geneva.

Yienger, J. J., and H. Levy II (1995), Empirical model of global soil-biogenic NO_x emissions, *J. Geophys. Res.*, *100*, 11,447–11,464.

Yvon-Lewis, S. A., and J. H. Butler (2002), Effect of oceanic uptake on atmospheric lifetimes of selected trace gases, *J. Geophys. Res.*, *107*(D20), 4414, doi:10.1029/2002JD001267.

C. S. Atherton, D. J. Bergmann, P. J. Cameron-Smith, C. C. Chuang, P. S. Connell, J. E. Dignon, A. Franz, K. E. Grant, C. R. Molenkamp, D. D. Proctor, D. A. Rotman, and J. R. Tannahill, Atmospheric Science Division, Lawrence Livermore National Laboratory, 7000 East Avenue, L-103, Livermore, CA 94550, USA. (atherton2@llnl.gov; bergmann1@llnl.gov; cameronsmith1@llnl.gov; chuang1@llnl.gov; connell2@llnl.gov; dignon1@llnl.gov; franz2@llnl.gov; grant3@llnl.gov; molenkamp1@llnl.gov; proctor1@llnl.gov; rotman1@llnl.gov; tannahill1@llnl.gov)

D. E. Kinnison, Atmospheric Chemistry Division, National Center for Atmospheric Research, P.O. Box 3000, Boulder, CO 80307-3000, USA. (dkin@ucar.edu)